sustainability

MDPI

Article

Hydrogen Enrichment of Hythane Under Typical Natural Gas Pipeline Conditions: Changes in Properties and Their Operational Implications up to 30% Hydrogen Mole Fraction

Osama A. Marzouk

College of Engineering, University of Buraimi, Al Buraimi 512, Oman; osama.m@uob.edu.om

Abstract

Hythane is hydrogen-enriched natural gas, or a methane-dominated hydrogen-methane (CH_4–H_2) gas mixture. Hythane has attracted increasing attention as a more environmentally friendly alternative to natural gas, associated with a reduction in the carbonaceous content (thus, a reduction in carbon dioxide emissions) while taking advantage of existing global natural gas pipelines and gas-fired vehicle engines or industrial gas turbines with potentially limited retrofits. A clear understanding of how the chemical, thermofluidic, and transport properties of methane are altered due to blending natural gas with hydrogen is needed. To this end, the variations of 20 properties of methane–hydrogen mixtures were evaluated as the hydrogen mole fraction increased from 0% (pure methane) to 30% (upper limit for hythane) with a uniform step of 1%. The results are presented here. The pressure and temperature were set to 30 bar (absolute) and 20 °C, which represent a typical environment for transported natural gas in pipelines. These properties were computed using the CoolProp package in Python, and the results are analyzed to propose either a linear or a quadratic regression model for each of the 20 properties to reveal their dependence on hydrogen blending. A pressure-sensitivity analysis (between 1 bar and 50 bar) and a temperature-sensitivity analysis (between 20 °C and 70 °C) for the midrange composition of 85% CH_4 and 15% H_2 were performed. The current work is intended to serve as a compact reference for understanding how progressive hydrogen enrichment affects the behavior of hythane and the implications of this hydrogen enrichment for fuel handling, flow behavior, and energy performance. Compared to pure methane (CH_4), the properties with the largest relative increase were the thermal diffusivity (159.2% increase), thermal conductivity (127.3% increase), and specific entropy (45.7% increase). On the other hand, the properties with the largest relative decrease were the Prandtl number (50.1% decrease), Joule–Thomson coefficient (44.2% decrease), and density (28.8% decrease). At 30% H_2, the volumetric energy density at pipeline conditions decreased by 23.7%, while the direct carbon dioxide emissions per unit of released energy decreased by 11.4%.

Keywords: hythane; hydrogen; methane; natural gas; CoolProp

Check for updates

Received: 29 October 2026
Revised: 18 November 2026
Accepted: 26 November 2026
Published: 28 November 2026

Copyright: © 2026 by the author. Licensee MDPI, Basel, Switzerland. This article is an open access article distributed under the terms and conditions of the Creative Commons Attribution (CC BY) license.

1. Introduction and Literature Review

1.1. Overview of Hythane

As of 2025, there are more than 4000 natural gas pipelines globally. Together, these gas pipelines extend over 1.5 million km [1]. Most of these pipelines carry compressed natural gas, while a small portion of approximately 9% (132,000 km) carry liquefied natural gas (LNG) [2]. These giant networks of natural gas pipelines are in addition to 206,000 km

of worldwide gas pipelines in development. Given that the Earth's perimeter is nearly 40,000 km, existing gas pipelines are sufficient to encircle the Earth 38 times. Planned pipelines alone encircle the Earth more than five times. The United States has the longest gas pipeline network, with the combined length of its gas pipelines being around 340,000 km as of December 2024 [3]. Well-established gas markets in Europe and North America are characterized by concentrated gas pipeline trade and capacity [4].

Hydrogen is a non-traditional valuable energy carrier (either as a fuel or as a chemical feedstock) that is associated with zero carbon dioxide (CO_2) emissions [5]. Hydrogen can be used in non-traditional clean power systems, such as fuel cells and magnetohydrodynamic generators [6–8]. Due to the large difference in the chemical and physical properties of hydrogen compared to natural gas, transporting pure hydrogen in a natural gas pipeline is not technically realistic. Hydrogen has some peculiar characteristics that inhibit such straightforward repurposing of natural gas pipelines, such as hydrogen embrittlement (HE), wide flammability limits [9], elevated levels of hazards due to a low ignition energy [10], and easy leakage [11].

Therefore, the concept of hydrogen blending into natural gas, which can be approximated as methane [12,13], has been investigated recently as a practical pathway for reducing the carbon footprint of gaseous-fuel systems while realistically making use of the existing natural-gas infrastructure. Such a blend is referred to as hythane (hydrogen–methane), as well as hydrogen-rich natural gas (HRNG) or hydrogen-enriched compressed natural gas (HECNG or HCNG) [14]. The term hythane is a portmanteau that is formed from the words "hydrogen" and "methane", thereby reflecting the two principal components of the blend. The term "hythane" is associated with work by Lynch and Marmaro [15]. Their U.S. patent US5139002A "Special purpose blends of hydrogen and natural gas" (filed by Hydrogen Consultants Inc on 30 October 1990 and granted on 18 August 1992) in the early 1990s is the first clearly documented technical use of hythane as a fuel blend. The hydrogen content in hythane is typically limited to 30% by mole (by volume) [16] because below this threshold, the combustion characteristics are not negatively impacted [17,18] and hydrogen embrittlement is insignificant such that no material replacement is needed [19]. Thus, a retrofit to the compressed natural gas (CNG) pipelines, burners, and combustion engines might not be necessary [20]. It should be noted that the term "hythane" is a broad term for any methane-dominated gaseous mixture of hydrogen and methane (or natural gas). Meanwhile, the term "Hythane®" is a registered trademark corresponding to a specific composition of 20% hydrogen and 80% natural gas (by volume) [21].

Molecular hydrogen (H_2) has a very different molecular weight, density, gravimetric energy content, transport behavior, heating value, and radiative characteristics compared to methane (CH_4) [22,23], which is the dominant constituent of natural gas and can constitute 95% of natural gas by volume. Therefore, the concentration of hydrogen in hythane is a governing factor in determining the performance, safety, and infrastructure implications. Even moderate enrichment can change how the blended hythane fuel behaves in storage, distribution, metering, and combustion.

1.2. Summary of Selected Studies on Hythane

Recent reviews of the literature explored replacing natural gas with hythane while examining several factors in determining the performance, safety, and infrastructure implications of transporting such hydrogen–methane mixtures. For example, Hora et al. [24] concluded that the transition from methane to hydrogen as an energy carrier presents both opportunities and challenges in terms of the existing transport infrastructure. To achieve this shift efficiently and safely, they proposed incremental integration of hydrogen, with an initial phase of integrating hydrogen into existing natural gas systems through blending

hydrogen with methane at concentrations from 5% to 30%. They emphasized that such blending is contingent upon local regulations. They also considered that a thorough understanding of the piping materials' properties is a requirement for the effective management of this gaseous transition.

Wang et al. [25] conducted a feasibility analysis for the transportation of hythane in natural gas pipelines. They recommended that the hydrogen mole fraction (volume fraction) does not exceed 27%. Also, they pointed out that the added hydrogen may result in a drop in pressure and flow rate corresponding to the equilibrium operating point, leading to a reduction in the gas transmission capacity.

Mahajan et al. [26] reported a review of hydrogen blending in gas pipeline networks. They stressed the environmental advantage of such blending due to phasing out the carbon content in natural gas in favor of the zero-carbon hydrogen that can be produced from solar [27] and wind power [28] units combined with electrolysis systems [29]. They clarified the advantage of blending hydrogen with natural gas through a seamless transition with minimum disruptions in power or heat generation. They mentioned several hydrogen blending projects, such as HyDeploy [30], GRHYD [31], THyGA [32], and HyBlend [33], which aim at developing efficient pathways toward decarbonization, carbon neutrality, and net-zero emissions of greenhouse gases (GHG) [34] to combat climate change. Also, they referred to techno-economic models being developed to estimate the cost and energy transportation efficiency due to the delivery of hythane. Despite these attractive large-scale efforts toward the deployment of the hythane shift, they identified some concerns during transport, such as overpressure and leakage.

Leicher et al. [35] discussed and analyzed blends of hydrogen and natural gas while focusing on combustion science as applied to residential and commercial gas appliances. They concluded that the admixture of hydrogen into natural gas may lead to higher combustion temperatures as well as laminar combustion speeds. In addition, the flame shape and flame position are also expected to change. Their study suggested that in appliances designed for natural gas [36], flashback risk should be carefully examined, as well as higher nitrogen oxide (NO_x) emissions [37].

McReynolds et al. [38] examined the effects of hydrogen blending on methane emissions within the distribution network of natural gas and within end-use piping. They commented that the small size of the hydrogen molecules and their high mobility raise a concern that hythane (hydrogen–natural gas blend) is more susceptible to leaking than pure natural gas. The researchers conducted methane emission measurements (chamber-based) within the natural gas distribution infrastructure as well as at end-use piping using hythane of 0–40% hydrogen by mole. They reported that the total methane emissions were 7–26% lower for hythane than for pure natural gas. Their testing showed that a drop in the total methane leakage can be achieved by hythane blending up to 40% hydrogen mole fraction, and only minimal infrastructure upgrades are needed in the short term.

Di Lullo et al. [39] considered the blending of blue hydrogen, which is hydrogen produced by processing natural gas or coal while using carbon capture and sequestration (CCS) technologies to avoid the release of produced carbon dioxide into the atmosphere [40]. Their application domain was direct consumption, and they examined the effect of hydrogen concentration on transportation and on the well-to-combustion (WTC) greenhouse gas (GHG) emissions. They selected a moderate hythane blend with 15% hydrogen and 85% natural gas (by mole) and assessed the GHG emissions of hythane using a developed model. They found that combustion GHG emissions decreased by 4%, while transportation GHG emissions increased by 8%. They suggested that steam methane reforming (SMR) of hydrogen with 90% carbon capture can achieve a 3% reduction in WTC GHG emissions. Also, they estimated that WTC GHG emissions can increase by 2% in the absence of carbon

capture. While green hydrogen produced by clean electricity supply is favored over blue hydrogen from an environmental perspective, blue hydrogen production is cheaper [41]. Grey hydrogen (produced from fossil natural gas without carbon capture and sequestration) is even cheaper [42], and it still dominates industrial hydrogen production [43].

Makaryan et al. [44] conducted a comprehensive review on the challenges and opportunities of hythane. They concluded that most of the reviewed works showed that the use of hythane in internal combustion engines (ICEs) has a favorable impact by improving the performance as well as emission characteristics of these hythane-fired engines that can be novel power units in ground and aerial mobility [45,46] as well as low energy (green) buildings. For those researchers, the most significant characteristic of hythane is the concentration of hydrogen in that hydrogen–methane fuel mixture. This hydrogen concentration was found to strongly affect the combustion process of hythane and to control the optimal operating point of the internal combustion engine. They found that low-hydrogen hythane does not require additional safety measures and does not involve elevated risks beyond those corresponding to natural gas. They called for further research on the compatibility of pipeline materials with hythane, safety conditions for equipment operating with hythane, and the environmental feasibility of using hythane.

Dally et al. [47] used a hydrogen-methane mixture as a fuel for turbulent nonpremixed flames. They found that this fuel mixture can be successfully adopted in stabilized combustion, where it yields a stable flame that is anchored to burners of the bluff-body type. Later numerical simulations were able to reproduce this favorable feature in hydrogen-methane flames [48].

In a recent study, Pallav et al. [49] demonstrated that blending 18–25% (by mole) hydrogen into natural gas can strongly improve combustion performance in India's city gas distribution (CGD) systems while using the same existing infrastructure. By utilizing a full-scale testbed with real CGD pipeline materials along with domestic burners, the study showed that increasing hydrogen content gradually transforms the flame from deep blue to a clean bluish-violet profile, thereby reducing luminosity and soot, reducing flame length, increasing burning velocity, and offering the best balance of flame stability and thermal efficiency.

1.3. Scope of the Present Study

As implied by the discussed literature studies in the previous subsection, property-based characterization of hythane is important for successful design and performance prediction. This is because the addition of hydrogen to methane changes the behavior of the blend not only chemically (chemical properties change), but also physically (thermofluidic and transport properties change). Such changes, if large enough, can affect the operation of hythane equipment and the distribution network. For example, density affects storage and flow metering; viscosity [50] and thermal conductivity affect transport behavior, convective heat transfer, pressure losses, and hydrodynamic loads. In addition, compressibility and speed of sound influence gas-dynamic response [51]. Furthermore, energy metrics (such as the specific enthalpy and the specific heat capacity at constant pressure) affect the interchangeability of hythane with natural gas (methane) in practical systems. A compact study that tracks all these properties over the relevant hydrogen fraction range for methane and provides analytical models for describing how these properties change due to progressive replacement of natural gas with hydrogen can therefore support the scientific interpretation of hythane behavior and facilitate preliminary engineering design.

The primary objective of the present study is to document how 20 intrinsic (size-independent) properties of hythane vary as the hydrogen mole fraction increases from 0% (pure methane) to 30% (representative upper limit on hydrogen content in hythane). The

variation of these properties as a function of the hydrogen enrichment (specifically, as a function of the hydrogen mole fraction) was computed and is presented graphically and numerically in a systematic way that aids in manifesting the quantitative and qualitative impact of this hydrogen enrichment on hythane. Also, 20 regression models (either linear or quadratic) are proposed for these 20 properties. The current work focuses on a composition sweep from pure methane (0% hydrogen mole fraction, 100% methane) to high-hydrogen hythane (30% hydrogen mole fraction, 70% methane). This work does not attempt to cover all possible operating temperatures and pressures in the gas industry. Instead, it provides a structured report of the computed trends of 20 selected hythane properties at a representative absolute pressure of 30 bar (3 MPa) for natural gas transportation pipelines [52,53], with a reasonable average ambient temperature of 20 °C [54]. The discussed results here facilitate further extension toward application-specific operating envelopes, as well as feasibility analysis of hydrogen–methane blending.

In the current study, natural gas is represented by pure methane, so hythane is treated as a binary methane–hydrogen mixture. As mentioned in Section 1.1, natural gas can be approximated as methane [12,13], which is its dominant component. This simplification also isolates the effect of hydrogen enrichment from the effects of the other natural gas components, whose proportions vary from one gas source to another, and thus keeps the results general rather than specific to a particular gas field. However, actual natural gas also contains small amounts of heavier hydrocarbons (mainly ethane and propane) and inert components (mainly nitrogen and carbon dioxide). These components shift the absolute values of some properties (such as the molecular weight, density, and heating value), while the trends caused by hydrogen enrichment are expected to remain qualitatively similar. Where a specific natural gas composition is required, the same computational procedure can be applied, because the GERG-2008 mixture model adopted in CoolProp covers the main natural gas components.

1.4. Contributions of the Current Study

The contributions of the present study to the fields of hythane transportation, hythane deployment, hydrogen utilization, and computational modeling of hythane include providing a coherent, verified, and well-documented property-based characterization of hythane over a wide range of chemical compositions, with the hydrogen mole fraction ranging from 0% to 30%, and with a fine composition resolution of 1% hydrogen mole fraction.

While hydrogen–natural gas blending has been widely studied, the literature focuses on infrastructure compatibility, combustion behavior, leakage, emissions, or techno-economic performance. Consequently, a clear gap remains in the systematic, composition-resolved characterization of the coupled chemical, thermofluidic, and transport properties of methane–hydrogen mixtures under representative pipeline conditions. In particular, the reviewed studies do not provide (as one coherent standalone real-gas framework as presented here) an incremental compositional sweep from 0% to 30% hydrogen, simultaneous evaluation of 20 properties, compact regression correlations for every property, independent validation against NIST and Cantera, pressure-sensitivity analysis, and temperature-sensitivity analysis. The novelty of the present study lies in integrating these separate elements into a single systematic, and comprehensive property map intended for preliminary pipeline analysis and system-level engineering calculations.

Several studies in the literature have addressed infrastructure challenges, pipeline compatibility, combustion behavior, leakage, emissions, or techno-economic models of hydrogen–natural gas blending. However, the present work addresses a different topic and focuses on the systematic response of a comprehensive group of chemical, thermofluidic, and transport properties of methane–hydrogen mixtures (hythanes) under representative

pipeline conditions. In contrast to examining a limited number of properties, a narrow range of blend compositions, or adopting simplified ideal-gas approximations, the current study evaluates 20 properties consistently using the real-gas modeling tool CoolProp and validates selected results from it against the NIST Chemistry WebBook online simulator, the Cantera desktop simulator, and published data in the literature. The current study identifies and proposes compact regression models for each property as a function of hydrogen content, thereby facilitating the convenient incorporation of these proposed regression models into other independent modeling frameworks or preliminary designs. The current study also presents a pressure sensitivity analysis and a temperature sensitivity analysis to broaden its scope and avoid being limited to one pressure and temperature setting. These sensitivity analyses provide insights into the impact of possible variations in either pressure or temperature on hythane properties and can be helpful in qualitatively and quantitatively estimating the impact of changes in the ambient conditions or the impact of hythane treatments during its transportation (such as compression) on its behavior.

Therefore, the contribution of this work is not only the application of simulation tools and reporting of computed property changes, but also the development of a compact resource that analytically, numerically, and visually links progressive hydrogen enrichment to practical implications for hythane handling, flowing behavior, thermal storage capacity, heat transfer, throttling processes, metering, and preliminary pipeline design.

The proposed regression correlations also offer practical advantages over direct CoolProp calculations. They are closed-form algebraic expressions that can be evaluated in a spreadsheet, by hand, or within other software without installing a thermophysical library or configuring a mixture backend. They can be differentiated analytically, such that the slope of each correlation directly gives the sensitivity of a property to hydrogen enrichment (for example, at the baseline conditions, the density of hythane decreases by about 0.20 kg/m^3 for every 1% increase in the hydrogen mole fraction). They are also computationally inexpensive, which is advantageous when properties must be evaluated repeatedly, as in pipeline-network simulations, optimization studies, and real-time monitoring or control, where repeated calls to a full Helmholtz-energy mixture model can become costly. Within the investigated range of 0% to 30% hydrogen, these correlations reproduce the CoolProp results with a maximum relative residual below 3% for every property, as shown in Section 3.2. Therefore, these correlations are not intended to replace CoolProp, but to provide a compact, transparent, and portable representation of its results for the conditions considered here.

Table 1 establishes a comparison between the current work and the closest studies discussed in Section 1.2, based on dimensions that construct methodological proximity: application focus and main method, hydrogen-content range, operational conditions, examined outputs, validation, empirical correlation modeling, and sensitivity analysis.

Table 1. Comparison between recent literature sources and the present study.

Study	Primary Focus and Method	H_2 Range and Conditions	Outputs	Validation, Correlations, Sensitivity	Difference from the Current Study
Wang et al. [25]	Feasibility analysis of transporting hydrogen–natural-gas mixtures in existing natural-gas pipelines.	Recommended an H_2 mole fraction not exceeding 27%.	Equilibrium pressure and flow rate, gas transmission capacity, and pipeline-transport feasibility.	No property-by-property regression set or independent property validation reported in the manuscript summary; operating-point effects were considered.	Application-level pipeline performance rather than a unified map of chemical, thermofluidic, and transport properties.

Table 1. *Cont.*

Study	Primary Focus and Method	H_2 Range and Conditions	Outputs	Validation, Correlations, Sensitivity	Difference from the Current Study
McReynolds et al. [38]	Chamber-based measurements at natural-gas distribution infrastructure and end-use piping.	0–40% H_2 by volume; facility-specific experimental conditions.	Methane emissions and leakage behavior; total methane emissions were reported as 7–26% lower for hythane than for pure natural gas.	Experimental measurements; no complete thermophysical-property regressions or pressure/temperature sensitivity matrix.	Leakage-focused field evidence rather than composition-resolved prediction of multiple intrinsic mixture properties.
Di Lullo et al. [39]	Modeling of blue-hydrogen blending for direct consumption, including pipeline transportation and well-to-combustion greenhouse-gas assessment.	Representative 15% H_2/85% natural-gas blend (by volume); scenario-dependent pipeline and carbon-capture assumptions.	Transportation and combustion greenhouse gas (GHG) emissions, well-to-combustion (WTC) emissions, and pipeline energy capacity.	Included sensitivity and uncertainty analyses for the emissions/transport model; no regression equation for each intrinsic fluid property.	Environmental and energy-capacity assessment at a selected blend rather than a fine composition sweep across 20 properties.
Pallav et al. [49]	Full-scale city-gas-distribution testbed using existing pipeline materials and domestic burners.	18–25% H_2 by mole; experimental city gas distribution (CGD) and burner conditions.	Flame appearance and length, soot tendency, burning velocity, flame stability, and thermal efficiency.	Experimental demonstration; no real-gas property database, complete regression set, or broad pressure/temperature sensitivity analysis.	Combustion and infrastructure compatibility within a narrow blend range rather than a general property-level engineering reference.
Current study	Real-gas computational characterization using CoolProp, with independent benchmarking against NIST, Cantera, and literature data.	0–30% H_2 at 1% increments; baseline 30 bar and 20 °C; pressure sensitivity from 1 to 50 bar and temperature sensitivity from 20 to 70 °C for 15% H_2.	Twenty chemical, thermofluidic, and transport properties, plus quantitative implications for handling, flow, heat transfer, metering, and throttling.	Selected-property validation; one linear or quadratic correlation for every property using an R^2 threshold of 0.99; pressure and temperature sensitivity analyses.	Integrates breadth, 1–resolution composition mapping, real-gas consistency, transferable correlations, independent validation, and operating-condition sensitivity in one framework.

As shown in the above table, the cited studies provide important but application-specific evidence on pipeline feasibility, leakage, greenhouse-gas (GHG) performance, and combustion behavior. The current study expands the literature by combining a fine 31-composition sweep with simultaneous real-gas evaluation of 20 intrinsic properties, compact correlations for every property, independent benchmarking, and pressure-sensitivity and temperature-sensitivity analyses. Thus, the claimed novelty includes an integrated and transferable property framework rather than isolated use of a simulation package or the general study of hydrogen–natural gas blending.

1.5. Manuscript Structure

In the next parts of this manuscript, Section 2 is presented. It includes a description of the utilized computational framework, and a validation check for this framework. This is followed by Section 3, where the pressure-temperature phase diagrams for pure methane

and pure hydrogen are presented first, and then the variation of 20 hythane properties with the hydrogen mole fraction is visualized and discussed. These visualizations also include proposed regression model equations. A pressure sensitivity analysis and a temperature sensitivity analysis are also provided for an intermediate hythane composition (15% hydrogen molar fraction). Finally, concluding remarks are provided.

2. Methodology

2.1. Computational Framework

The research method followed in the current study was an applied and computational investigation. The primary fluid property calculation tool used here was CoolProp [55–57], which provides an open-source framework for estimating pure-fluid properties and mixture properties using equations of state, transport-property correlations, and mixture models derived from published literature. CoolProp is a C++ library with several wrappers (interfaces) that allow it to be used within other software environments, such as Python [58], Modelica [59], MATLAB [60], Octave [61], and MathCAD [62]. CoolProp is considered a reliable and well-documented tool that has been used in multiple studies and simulator projects [63–66]. It was initially released in 2012 and has been improved progressively over many years till today [67].

The CoolProp database has more than 120 fluids (components). Nearly all the fluid models in CoolProp are based on the real-gas Helmholtz energy formulation for the equation of state (EOS) [68–73], described in terms of the reduced density ρ_r and reduced absolute temperature T_r. These two non-dimensional reduced variables are the dimensional density (ρ) and dimensional absolute temperature (T) normalized by their corresponding critical density ρ_c and critical absolute temperature T_c, respectively [74]. Thus, the two independent non-dimensional properties for the Helmholtz equation of state are:

$$\rho_r = \frac{\rho}{\rho_c} \tag{1}$$

$$T_r = \frac{T}{T_c} \tag{2}$$

This density-temperature-based Helmholtz energy formulation is a convenient choice for constructing the equation of state [75]. The reason is that this choice means that all the thermodynamic properties of interest can be obtained directly from partial derivatives of the Helmholtz energy [76,77].

The mixture model adopted in CoolProp is derived from the work of Kunz et al. [78] and Lemmon et al. [79–81]. According to this modeling method, a mixture is composed of two or more components [82]. For each pair of these components, it is necessary to have information (estimated binary interaction parameters) about the excess Helmholtz energy term [83–85] and the reducing function [86,87].

The results were computed under the Python environment (version 3.13.9) with the installed CoolProp package (version 7.2.0). All hythane states were evaluated using the multi-fluid Helmholtz-energy backend of CoolProp (HEOS) through its high-level PropsSI function, with each mixture specified by the fluid string "Methane[xCH4]&Hydrogen[xH2]", where xCH4 and xH2 are the mole fractions of methane and hydrogen expressed as decimal fractions (xCH4 = 1−xH2). Because no backend prefix is included in this string, CoolProp applies its default HEOS backend. Each state was fixed by temperature and pressure inputs, set to 293.15 K (20 °C) and 3 MPa (30 bar) for the baseline case, and varied from 0.1 MPa to 5 MPa (1 bar to 50 bar) at 20 °C and from 293.15 K to 343.15 K (20 °C to 70 °C) at 30 bar in the sensitivity analyses. The thermal diffusivity and the kinematic viscosity were computed from the CoolProp outputs as k/(ρ·cp) and μ/ρ, respectively, and the Joule–Thomson

coefficient was computed as $-(\partial h/\partial P)T/(\partial h/\partial T)P$ using the partial-derivative outputs of CoolProp. The default binary interaction parameters and departure function for the methane–hydrogen pair, as distributed with CoolProp (originating from the GERG-2008 formulation of Kunz et al. [78]), were adopted without any modification, and no user-defined mixture parameters were introduced. The mixture transport properties (thermal conductivity and viscosity) were obtained from the default mixture transport models of CoolProp. CoolProp provides property evaluation for pure fluids and mixtures through Helmholtz-energy-based formulation and documented mixture models. For methane-hydrogen systems (hythane) analyzed here, the mixture is defined by the mole fractions of hydrogen and methane, where the hydrogen content was varied incrementally from 0% to 30% by mole. At each composition point, the 20 selected properties were evaluated under a consistent set of state inputs. The resulting numerical outputs were exported, plotted, and a subset of them were tabulated to visualize and quantify the dependence of each property on hydrogen enrichment.

The Trendline tool in Microsoft Excel was used to propose a regression model for each property. A linear model was usually sufficient to achieve excellent fit, with an R-squared value (the coefficient of determination, R^2) exceeding 0.99. In two cases only (namely, the adiabatic index and the Prandtl number), the linear regression model was unable to attain this goodness-of-fit threshold, and in these two cases, a quadratic regression fit was proposed instead of the linear one, and the 0.99 threshold for R^2 is then satisfied.

2.2. Hythane Mixture Definition and Composition Range

The hythane composition is parameterized using the hydrogen mole fraction (X_{H2}). Methane occupies the balance of the mixture, with its mole fraction (X_{CH4}) being uniquely determined for each hydrogen mole fraction as follows:

$$X_{CH4} = 100\% - X_{H2} \quad (3)$$

The compositional range investigated here is $0\% \leq X_{H2} \leq 30\%$, corresponding to $100\% \geq X_{CH4} \geq 70\%$, respectively. This range is practically relevant because hydrogen fractions up to about 30% are often reported in the literature for assessing the behavior of hythane as a special methane-dominated mixture rather than a generic methane–hydrogen fuel.

A small increment of the composition was selected during the sweeping process, with a fixed interval of the hydrogen mole fraction of $\Delta X_{H2} = 1\%$. Such high resolution helps in accurately capturing the variations of the hythane properties in response to hydrogen enrichment. Thus, a total of 30 hythane compositions plus the reference case of pure methane ($X_{H2} = 0\%$) were investigated. Thus, 31 compositions for each property were investigated. In addition, the properties of pure hydrogen were also computed as a reference case of interest.

2.3. Evaluated Properties

For each of the analyzed chemical compositions, 20 properties were computed, which are listed in Table 2. These properties address various aspects of the behavior of hythane, as well as pure methane and pure hydrogen. These properties were selected based on their potential usefulness in the design or operation of pipelines or equipment used in transporting or processing hythane. For example, density is an important property to monitor when transitioning from methane (natural gas) to hythane because it directly affects the mass flow rate and bulk transport speed [88]. Likewise, specific enthalpy is an important metric that represents the energy content in the transported hythane. Also, the absolute viscosity affects the pressure drop along a hythane pipeline.

Table 2. List of hythane properties examined here.

Index	Category	Property	Symbol	Unit
1	Chemical	Molecular weight	MW	kg/kmol
2	Chemical	Specific gas constant	R_g	J/(kg·K)
3	Chemical	Hydrogen mass fraction	Y_{H2}	%
4	Chemical	Methane mass fraction	Y_{CH4}	%
5	Thermofluidic	Speed of sound	c	m/s
6	Thermofluidic	Density	ρ	kg/m^3
7	Thermofluidic	Specific volume	$\not{v}$	m^3/kg
8	Thermofluidic	Specific internal energy	u	kJ/kg
9	Thermofluidic	Specific enthalpy	h	kJ/kg
10	Thermofluidic	Specific entropy	s	kJ/(kg·K)
11	Thermofluidic	Specific heat capacity at constant pressure	C_p	J/(kg·K)
12	Thermofluidic	Specific heat capacity at constant volume	C_v	J/(kg·K)
13	Thermofluidic	Adiabatic index	γ	[-]
14	Thermofluidic	Compressibility factor	Z	[-]
15	Thermofluidic	Joule-Thomson coefficient	μ_{JT}	K/MPa
16	Transport	Thermal conductivity	λ	W/(m·K)
17	Transport	Absolute viscosity (dynamic viscosity)	μ	mPa·s (cP)
18	Transport	Thermal diffusivity	α	mm^2/s
19	Transport	Momentum diffusivity (kinematic viscosity)	ν	mm^2/s (cSt)
20	Transport	Prandtl number	Pr	[-]

The units appearing in the table reflect the units used in displaying the values of these properties in the current work. Some of these units are not the native units reported directly by CoolProp, which uses SI units. Instead, for convenience and practicality, some properties were scaled to be easier to comprehend. For example, the proper unit (cSt or centistokes, mm^2/s) is used for the momentum diffusivity instead of the theoretical (m^2/s), which is too large compared to typical values of this property for hythane.

While the above properties might be familiar to the reader, it might be useful to briefly explain four of them because these may be less frequently encountered in fluid mechanics or thermodynamics contexts.

In the above table, the adiabatic index (also called specific heat ratio) is the ratio of the specific heat capacity at constant pressure to the specific heat capacity at constant volume. This non-dimensional property has an important role in high-speed flows and gas dynamics [89]. Mathematically, the adiabatic index is defined as follows:

$$\gamma = \frac{C_p}{C_v} \tag{4}$$

It is useful to add that, strictly speaking, the above definition is for the specific heat ratio, not the adiabatic exponent (also called isentropic exponent or isentropic index) [90]. However, for the chemically frozen hythane mixtures considered here, the specific heat ratio is identical in value to the adiabatic index [91]. However, gaseous mixtures undergoing instantaneous changes in their chemical composition through chemical equilibrium and spatial transience [92] can have slightly different values for the specific heat ratio and the adiabatic index [93].

In the above table, the compressibility factor is the ratio of the ideal-gas density (ρ_{ideal}) to the real density (ρ), which is equivalently the ratio of the real specific volume ($\bar{v}_{ideal}$) to the ideal-gas specific volume ($\bar{v}$) [94]. This is mathematically expressed as follows [95]:

$$Z = \frac{\rho_{ideal}}{\rho} = \frac{P}{\rho\, R_g T} = \frac{P\,\bar{v}}{R_g T} = \frac{\bar{v}}{\bar{v}_{ideal}} \tag{5}$$

In the above table, the Prandtl number is the ratio of the momentum diffusivity to the thermal diffusivity [96]. Mathematically, this is expressed as follows:

$$\mathrm{Pr} = \frac{\nu}{\alpha} = \frac{\mu/\rho}{\lambda/\left(\rho\, C_p\right)} = \frac{\mu\, C_p}{\lambda} \tag{6}$$

where the momentum diffusivity, or kinematic viscosity, is defined as follows:

$$\nu = \frac{\mu}{\rho} \tag{7}$$

and the thermal diffusivity is defined as follows:

$$\alpha = \frac{\lambda/C_p}{\rho} \tag{8}$$

For many gases, such as air [97] (nitrogen and oxygen) [98], helium [99], and hydrogen [100], the Prandtl number (Pr) at ambient pressures varies over a narrow range around the value of 0.7, with a weak effect of temperature. Methane tends to have a slightly higher Prandtl number [101] near 0.75, which increases with the pressure and approaches unity at 100 bar and 25 °C [102].

In the above table, the Joule–Thomson coefficient (μ_{JT}) measures how the temperature of a gaseous species changes during a throttling process, which is an isenthalpic expansion (an expansion occurring adiabatically with a constant specific enthalpy) [103]. It is mathematically defined as the partial derivative of temperature with respect to pressure (P) at a constant specific enthalpy (h) [104]:

$$\mu_{JT} = \left(\frac{\partial T}{\partial P}\right)_h = -\left(\frac{\partial h}{\partial P}\right)_T \Big/ \left(\frac{\partial h}{\partial T}\right)_p = -\left(\frac{\partial h}{\partial P}\right)_T / C_p \tag{9}$$

A negative value of (μ_{JT}) means that the gas warms during throttling, which is the case for hydrogen at room temperature [105,106]. On the other hand, a positive value of (μ_{JT}) means that the gas cools during throttling, which is the case for air at room temperatures [107]. For an ideal gas, the specific enthalpy is a function of the temperature only [108]. Thus, the partial derivative $\left(\frac{\partial h}{\partial P}\right)_T$ vanishes, and the Joule–Thomson coefficient becomes zero for ideal gases.

2.4. Validation Check

Despite the evident history of CoolProp, its adoption in various studies and projects, and good documentation, a validation check for this tool is added by comparing its predicted properties with those reported by an independent, reliable, and very popular tool, which is the NIST Chemistry WebBook online calculator [109,110]. This was developed by the United States National Institute of Standards and Technology (NIST) [111], and its official name is Standard Reference Database Number 69 (SRD 69) [112]. It is a major database that provides thermochemical, thermophysical, and ion-energetics data for thousands of chemical species [113]. Properties of methane [114] and hydrogen [115] were selected at the same absolute pressure of 30 bar and temperature of 20 °C, and these are the baseline conditions assigned to hythane here. Also, we compared the properties computed using

the thermochemical and transport library Cantera (version 3.2.0) [116,117] for a mid-range hythane composition of 85% methane and 15% hydrogen by mole. A subset of 10 properties from the total 20 properties was considered in this study to perform the benchmarking validation. Some of the 20 CoolProp properties were omitted in the validation because they are not directly reported by the NIST Chemistry WebBook online calculator (such as the specific gas constant) or Cantera (such as the Joule–Thomson coefficient). The same number of significant digits were maintained when comparing the results of CoolProp with those of NIST or Cantera, thereby rendering the comparison fair and consistent. As commonly practiced, the specific enthalpy and specific entropy reported here are relative to a reference (zero-value) state of saturated liquid [118,119] at an absolute pressure of 1 atm [120,121].

The validation comparison results are summarized in Table 3 for the two pure-gas cases and the gaseous mixture case (85% CH_4 and 15% H_2). It can be noticed that the agreement is considered satisfactory for almost all properties.

Table 3. Comparing fluid properties by CoolProp and by NIST Chemistry WebBook for pure methane, pure hydrogen, and an intermediate hythane composition (absolute pressure 30 bar and temperature 20 °C).

Property	Unit	Methane		Hydrogen		Intermediate Hythane (15% H_2)	
		CoolProp	NIST	CoolProp	NIST	CoolProp	Cantera
Molecular weight	kg/kmol	16.0428	16.0425	2.01588	2.01588	13.9388	13.9390
Speed of sound	m/s	436.44	436.44	1329.48	1329.47	475.84	479.98
Density	kg/m^3	20.875	20.875	2.438	2.438	17.792	17.156
Specific internal energy	kJ/kg	725.295	725.295	2641.932	2641.929	769.149	788.550
Specific enthalpy	kJ/kg	869.006	869.006	3872.664	3872.659	937.762	963.204
Specific entropy	kJ/(kg·K)	4.80658	4.80658	39.13132	39.13125	5.81130	5.87705
Specific heat capacity at constant pressure	J/(kg·K)	2418.58	2418.58	14368.76	14368.74	2648.49	2475.11
Specific heat capacity at constant volume	J/(kg·K)	1728.47	1728.47	10185.56	10185.54	1905.32	1878.62
Joule–Thomson coefficient	K/MPa	4.338991	4.338991	−0.304978	−0.304978	-	-
Thermal conductivity	W/(m·K)	0.035626	0.035451	0.186819	0.186819	0.058291	0.048595
Absolute viscosity	mPa·s (cP)	0.011513	0.011400	0.008820	0.008820	0.011053	0.011311

The largest deviation is for the thermal conductivity for the binary gas mixture case. Relative to the average (0.053443 W/(m·K)) of the two computed values of CoolProp (0.058291 W/(m·K)) and Cantera (0.048595 W/(m·K)), the absolute deviation is 18.14%. While this deviation is not small, it is tolerated given the inevitable approximations involved in the computation of the thermal conductivity in general [122], as well as the challenging binary mixture of hydrogen and methane, which includes very different molecular weights (disparate atomic sizes) [123]. This discrepancy is noticeably larger than those obtained for the pure-fluid cases, for which CoolProp agrees closely with the NIST values. The difference is therefore attributed mainly to the mixture transport models rather than to the pure-component property data. It should be noted that the thermal conductivity in a binary gas is neither obtained from a simple mole-fraction average nor from the equation of state. Rather, it depends on the adopted mixing rule, collision integrals, interaction parameters, and treatment of the large disparity in molecular mass and transport behavior between hydrogen and methane. Given that CoolProp and Cantera implement different mixture-

transport formulations, their predictions can diverge. CoolProp uses advanced transport models, ECSs (extended corresponding states) [124], and specialized real-gas correlations (Ely–Hanley) [125]. Cantera uses Chapman–Enskog kinetic theory with Lennard–Jones parameters [126] and a mixture-averaged transport model [127] to compute mixture thermal conductivity [128].

The second largest relative deviation is for the specific heat capacity at constant pressure, and it is 6.77%. This deviation is not high, and it drops as the absolute pressure drops. For example, it becomes 4.47% at 20 bar and 2.23% at 10 bar. This systematic pressure dependence indicates that the difference arises mainly from the distinct real-gas mixture formulations used by CoolProp. At higher pressures, intermolecular interactions and residual contributions to the heat capacity become more important, making the predicted value more sensitive to the adopted equation of state, mixing rules, and binary-interaction parameters, and CoolProp gives more accurate results than Cantera [129]. As the pressure decreases, the mixture approaches ideal-gas behavior, where these residual contributions diminish, and the predictions of the two models converge.

The third largest relative deviation is for either the density or the specific volume, and it is 3.64%, which is small. These two deviations have the same magnitude because the specific volume is simply the reciprocal of density. Therefore, a difference in the predicted mixture density produces a corresponding inverse difference in specific volume. This small discrepancy is consistent with differences between the underlying treatments of non-ideal interactions.

A closer inspection of the density and heat-capacity deviations clarifies their origin. The Cantera values in Table 3 were obtained using the GRI-Mech 3.0 input file (gri30.yaml) distributed with Cantera, whose thermodynamic model is an ideal-gas equation of state. The compressibility factor computed by CoolProp for the mixture of 85% CH_4 and 15% H_2 is 0.96425. The corresponding ideal-gas density is therefore 17.1562 kg/m^3, compared with the real-gas density of 17.7923 kg/m^3 obtained from CoolProp, which is a relative deviation of 3.64%. This is identical to the density deviation between CoolProp and Cantera. Similarly, the specific heat capacity at constant pressure computed by CoolProp for this mixture decreases from 2648.49 J/(kg·K) at 30 bar to 2588.33 J/(kg·K) at 20 bar, 2530.92 J/(kg·K) at 10 bar, and 2481.67 J/(kg·K) at 1 bar, thus approaching the pressure-independent ideal-gas value, which explains why the deviation in this property diminishes as the pressure decreases. Therefore, the density and heat-capacity deviations quantify the real-gas (residual) contributions that are captured by CoolProp but are absent from an ideal-gas treatment, rather than errors in either tool. Regarding independent experimental support, the multi-fluid Helmholtz-energy mixture model adopted in CoolProp (the GERG-2008 formulation [78]) was developed by fitting experimental data for natural gas components and their binary mixtures, including methane–hydrogen mixtures, and its estimated uncertainty in the gas-phase density is about 0.1% over a range that includes the conditions of the current study. Thus, the thermodynamic properties of hythane computed here (such as the density, compressibility factor, and speed of sound) rest on an experimentally validated basis, whereas the main remaining uncertainty lies in the mixture thermal conductivity, as discussed above.

For all remaining properties, the relative deviation between CoolProp and Cantera is within 2.7%. These limited deviations support the robustness of the CoolProp package.

Regarding the implications of the thermal-conductivity deviation for the reliability of the predicted thermal properties, it should be noted that the mixture validation was performed at a single mid-range composition (85% CH_4 and 15% H_2), whereas the two limiting pure-fluid cases (0% H_2 and 100% H_2) agree closely with NIST. Accordingly, the CoolProp thermal conductivity of hythane is expected to be most reliable near the methane-rich end of

the investigated range, and its uncertainty can be expected to grow as the hydrogen content increases and mixture-transport effects become more influential. Because the thermal diffusivity (Equation (8)) is proportional to the thermal conductivity and the Prandtl number (Equation (6)) is inversely proportional to it, this uncertainty propagates directly into these two derived transport properties, whereas the thermodynamic properties obtained from the equation of state are not affected by it. However, since all 31 compositions were computed consistently with the same CoolProp mixture-transport model, the predicted composition trends (the monotonic increase in the thermal conductivity and thermal diffusivity and the monotonic decrease in the Prandtl number with hydrogen enrichment), are expected to be more robust than the absolute values. An inspection of the computed results indicates that the CoolProp mixture thermal conductivity varies almost exactly linearly with the hydrogen mole fraction between the two pure-fluid limits. For example, at 15% H_2, CoolProp gives 0.058291 W/(m·K), compared with 0.058305 W/(m·K) obtained by linear mole-fraction interpolation between pure methane (0.035626 W/(m·K)) and pure hydrogen (0.186819 W/(m·K)), a difference of only about 0.02%. In contrast, the kinetic-theory mixture-averaged model in Cantera gives a value well below this linear interpolation (0.048595 W/(m·K)). This difference in the treatment of mixing is the most probable source of the 18.14% deviation. Consequently, the near-perfect linearity of the regression model for the thermal conductivity partly reflects the mixing treatment in CoolProp, and the actual thermal conductivity of hythane may fall below this linear trend at intermediate compositions. Therefore, the absolute values reported here for the thermal conductivity, thermal diffusivity, and Prandtl number of hythane should be treated as model-based estimates whose uncertainty may be comparable to the 18.14% deviation identified above. These values are recommended for comparative and preliminary analyses rather than final heat-transfer design, for which experimental mixture data should be consulted when available.

3. Results and Discussion

3.1. Pressure-Temperature (PT) Phase Diagram for Methane and Hydrogen

In addition to visualizing the variation of hythane properties as a function of hydrogen enrichment, the CoolProp simulator was used to generate a phase diagram for methane (CH_4) and another phase diagram for molecular hydrogen (H_2) using the pressure (P) and temperature (T) as the two independent state variables needed to fully describe the state [130]. These pressure-temperature (PT) diagrams are shown in Figure 1 (methane) and Figure 2 (hydrogen). The visualized contrast between the properties of methane and hydrogen presented here is useful for establishing a qualitative expectation of the impact of adding hydrogen to methane for forming hythane.

The difference between methane and hydrogen can be further demonstrated by comparing certain intrinsic properties for both species, particularly at their triple point and their critical point. This comparison is shown in Table 4. The values in the table were computed using CoolProp. Thus, they correspond to the PT phase diagrams presented above. Hydrogen has a much lower density, triple point temperature, critical temperature, and critical pressure than methane. However, their triple point pressures are not very different (although hydrogen still has a lower value). Some values quoted in the table were reported in the literature as benchmarks. Thus, the same table serves both to contrast methane with hydrogen and also to add a secondary validation check for the accuracy of CoolProp that is added to the primary validation check presented earlier. The good agreement between the CoolProp values and the corresponding third-party values in the literature is clear, and this agreement further supports the use of CoolProp as a fluid property simulator.

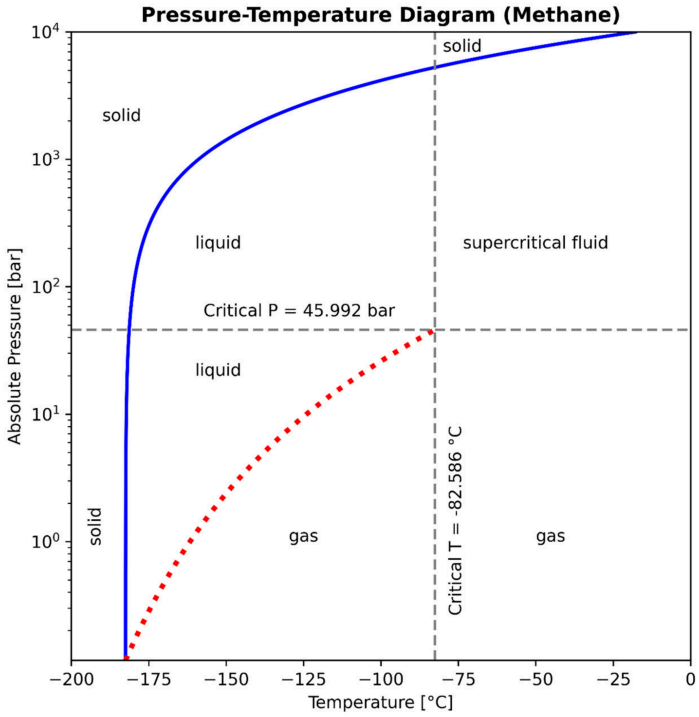

Figure 1. Pressure-temperature (PT) phase diagram for methane, showing different phase regions. This plot was made by the author, with the data produced using CoolProp [57]. The red dotted line represents the evaporation/condensation phase change boundary that separates the liquid-phase region from the gas-phase region. The blue solid line represents the melting/freezing (fusion/solidification) phase change boundary that separates the solid-phase region from the liquid-phase region.

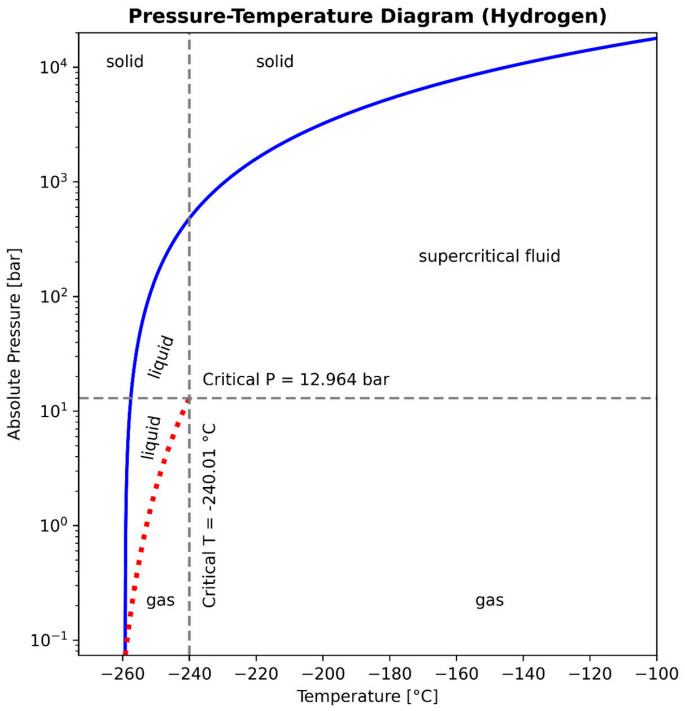

Figure 2. Pressure-temperature (PT) phase diagram for hydrogen, showing different phase regions. This plot was made by the author, with the data produced using CoolProp [57]. The red dotted line represents the evaporation/condensation phase change boundary that separates the liquid-phase region from the gas-phase region. The blue solid line represents the melting/freezing (fusion/solidification) phase change boundary that separates the solid-phase region from the liquid-phase region.

Table 4. Contrasted properties of methane and hydrogen.

Property	Methane	Literature Values	Hydrogen	Literature Values
Triple point temperature	90.6941 K −182.456 °C −296.421 °F	90.6861 K ± 0.2 [131]	13.9570 K −259.193 °C −434.547 °F	13.9 K [132]
Triple point absolute pressure	11696.1 Pa 87.7277 Torr 116.961 mbar 1.69637 psi 0.116961 bar	87.85 Torr [133]	7357.83 Pa 55.1882 Torr 73.5783 mbar 1.06716 psi 0.0735783 bar	54 Torr [134]
Triple point density (liquid)	451.475 kg/m^3 28.1419 mol/L	28.0536 mol/L [135]	77.0037 kg/m^3 38.1985 mol/L	-
Triple point density (vapor)	0.250744 kg/m^3 0.015630 mol/L	-	0.129853 kg/m^3 0.064415 mol/L	-
Critical temperature	190.564 K −82.586 °C −116.655 °F	190.551 K [136]	33.1443 K −240.006 °C −400.010 °F	33 K [137]
Critical pressure (absolute)	4599200 Pa 667.057 psi 45.99200 bar 4.599200 MPa	4.62 Mpa [138]	1296358 Pa 188.021 psi 12.9636 bar 1.29636 Mpa	1.284 Mpa [139]
Critical density	162.660 kg/m^3	-	31.2499 kg/m^3	-

3.2. Variation of Hythane Properties with Hydrogen Mole Fraction

The main part of the results for the current study is presented here. This part includes visualized variations of 20 properties of hythane as quantities dependent on the hydrogen mole fraction when it varies between 0% and 30%. Tabulated data are also provided for selected hythane compositions. For each hythane property, a proposed regression model is presented (the regression equation and its R-squared value). In these regression models, the hydrogen mole fraction is treated as a decimal fraction. Thus, the hydrogen mole fraction of 15% (for example) should be converted into the decimal fraction 0.15, rather than the integer 15. Similarly, when the output variable from the regression model is a percentage (like the hydrogen mass fraction), it is computed by the regression model as a decimal fraction with a bounded range of 0.00–1.00, rather than 0–100.

To evaluate the reliability of the proposed regression models beyond the R2 value, additional statistical measures were computed for each of the 20 models using the 31 composition points (0% to 30% H_2). The adjusted R2, which accounts for the number of regression coefficients, is at least 0.9907 for all properties and is practically identical to the corresponding R2 value (the minimum R2 is 0.9911, for the specific heat capacity at constant pressure). The root-mean-square error (RMSE) of each model is small compared with the property values. The maximum relative residual over all compositions is below 1% for 10 properties and below 3% for all properties, with the largest values being 2.79% for the thermal diffusivity and 2.47% for the Prandtl number (for the hydrogen mass fraction, which is zero for pure methane, the RMSE is 0.12 percentage points). For most linear models, the residuals follow a smooth curved pattern rather than random scatter, which reflects a weak nonlinearity in the composition dependence that is small enough to be acceptable for engineering use. To independently evaluate the predictive accuracy, each model was refitted using only the 16 compositions with even hydrogen mole fractions (0%, 2%, …, 30%) and then used to predict the 15 excluded compositions with odd hydrogen mole fractions (1%, 3%, …, 29%). The maximum relative prediction error at these excluded compositions was below 2.1% for all properties. These results confirm that the correlations can reliably interpolate within the

investigated composition range. However, they should not be extrapolated beyond 30% H_2 or applied at other pressures and temperatures without re-evaluation.

To partially quantify the variation in the hythane properties with the hydrogen enrichment, in each plot the values of the shown property at the limiting cases of 0% and 30% hydrogen mole fractions are shown. None of the 20 hythane properties showed an extremum point (either a minimum or a maximum). In other words, all 20 properties showed monotonic profiles within the range of interest for the hydrogen mole fraction (namely, 0% to 30% hydrogen mole fraction) at the selected absolute pressure (30 bar) and temperature (20 °C).

It should be emphasized that the direct findings of the current study are the computed values of the 20 intrinsic hythane properties, their composition trends, the proposed regression models, and the pressure and temperature sensitivities. The engineering implications discussed alongside these results (such as changes in pipeline friction losses, compressor power demand, heat loss and insulation requirements, flow metering, and leakage tendency) are qualitative inferences drawn from these fluid properties using established fluid-mechanics and heat-transfer relations, rather than outputs of pipeline-network, compressor, or leakage simulations. Unless stated otherwise, these inferences assume that the same existing pipeline (same diameter, length, wall roughness, and insulation) is operated under steady conditions at the baseline pressure and temperature, and that hythane is compared with methane at the same mass flow rate. Under different operating constraints (for example, delivering the same energy flow rate rather than the same mass flow rate), the magnitude of some implications may differ. Therefore, these implications are intended to indicate potential tendencies that warrant attention, and their quantitative assessment requires dedicated hydraulic, thermal, compressor, and materials analyses, which are outside the scope of the present study.

3.2.1. Methane Mass Fraction

Figure 3 shows how the methane mass fraction (Y_{CH4}) for hythane changes as the hydrogen enrichment increases from 0% to 30% by mole. The figure also shows the variation of the methane mole fraction (X_{CH4}) for completeness, as this is a trivial property directly related to the hydrogen mole fraction (X_{H2}) through the balance formula presented in Equation (3), and it is not counted among the 20 properties being investigated.

The methane mole fraction declines exactly linearly from 100% to 70% as the hydrogen mole fraction increases from 0% to 30%, and this perfect correlation has the ideal R-squared (R^2 or coefficient of determination) value of 1.0000, as shown in the figure. The slope of –1.0000 signifies the progressive replacement of methane with hydrogen. Thus, for each amount of hydrogen mole fraction introduced, the same amount of methane mole fraction is removed.

The methane mass fraction decreases from 100% (at 0% hydrogen) to 94.8899% (at 30% hydrogen) almost linearly (R^2 0.9935), leading to a change of −5.1% with respect to the pure methane reference composition. This relative change is small in magnitude. Hydrogen enrichment has negligible effects on that property. The weak (slow) variation in this property is explained by the large molecular weight of methane compared to hydrogen, with the ratio being approximately 16:2.

For hythane as a binary mixture, the mass fraction of methane can be computed as follows [140]:

$$Y_{CH4} = \frac{X_{CH4}\, MW_{CH4}}{X_{CH4}\, MW_{CH4} + X_{H2}\, MW_{H2}} = \frac{(1 - X_{H2})\, MW_{CH4}}{(1 - X_{H2})\, MW_{CH4} + X_{H2}\, MW_{H2}} \quad (10)$$

Even at the upper limit of X_{H2} = 30%, the methane contribution term $(1 - X_{H2})$ MW_{CH4} in the denominator remains dominant compared to the hydrogen contribution term

$X_{H2}\ MW_{H2}$, which makes the methane mass fraction drop only slightly from the reference 100% value.

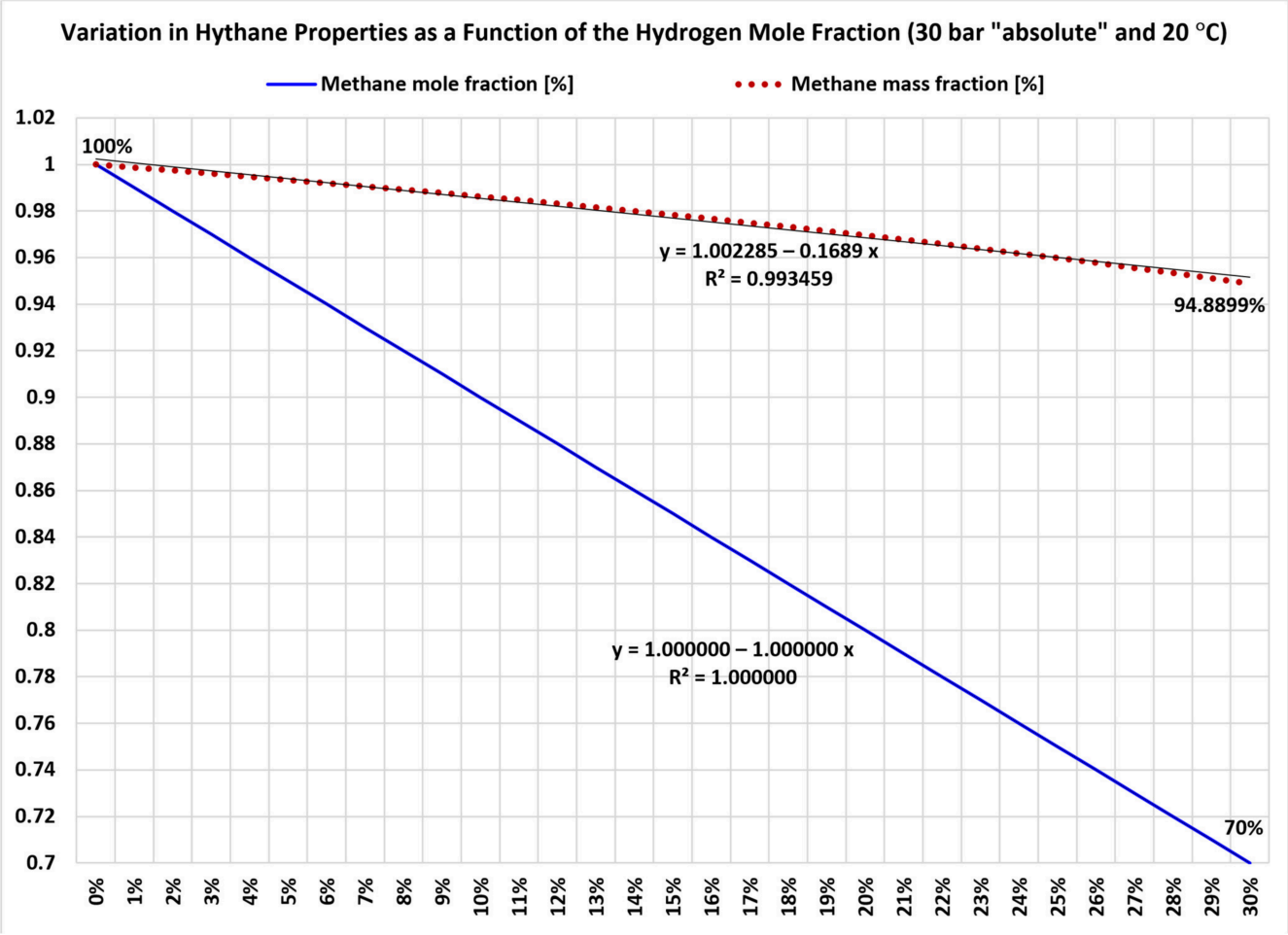

Figure 3. Variation in the methane mole fraction and the methane mass fraction for hythane, as a function of the hydrogen mole fraction. This plot was made by the author, with the data produced using CoolProp [57].

3.2.2. Hydrogen Mass Fraction

Figure 4 shows how the hydrogen mass fraction (Y_{H2}) for hythane changes as the hydrogen enrichment increases from 0% to 30% by mole.

The hydrogen mass fraction increases in a weakly nonlinear (R^2 0.9935) and accelerating pattern as the hydrogen mole fraction increases.

The hydrogen mass fraction is 1.3770% at 10% hydrogen mole fraction, 3.0457% at 20% hydrogen mole fraction, and 5.1101% at 30% hydrogen mole fraction. Therefore, between 10% and 20% hydrogen mole fractions, the percentage-point increase in the hydrogen mass fraction is 1.6688%. Between 20% and 30% hydrogen mole fractions, the percentage-point increase in the hydrogen mass fraction is 2.0644%. Thus, the gain in the hydrogen mass fraction over the molar hydrogen enrichment range 20–30% is larger than the gain over the molar hydrogen enrichment range 10–20%, which is larger than the gain over the molar hydrogen enrichment range 0–10%. This manifests the nonlinear accelerating gain in the hydrogen mass fraction of hythane as the molar hydrogen fraction increases.

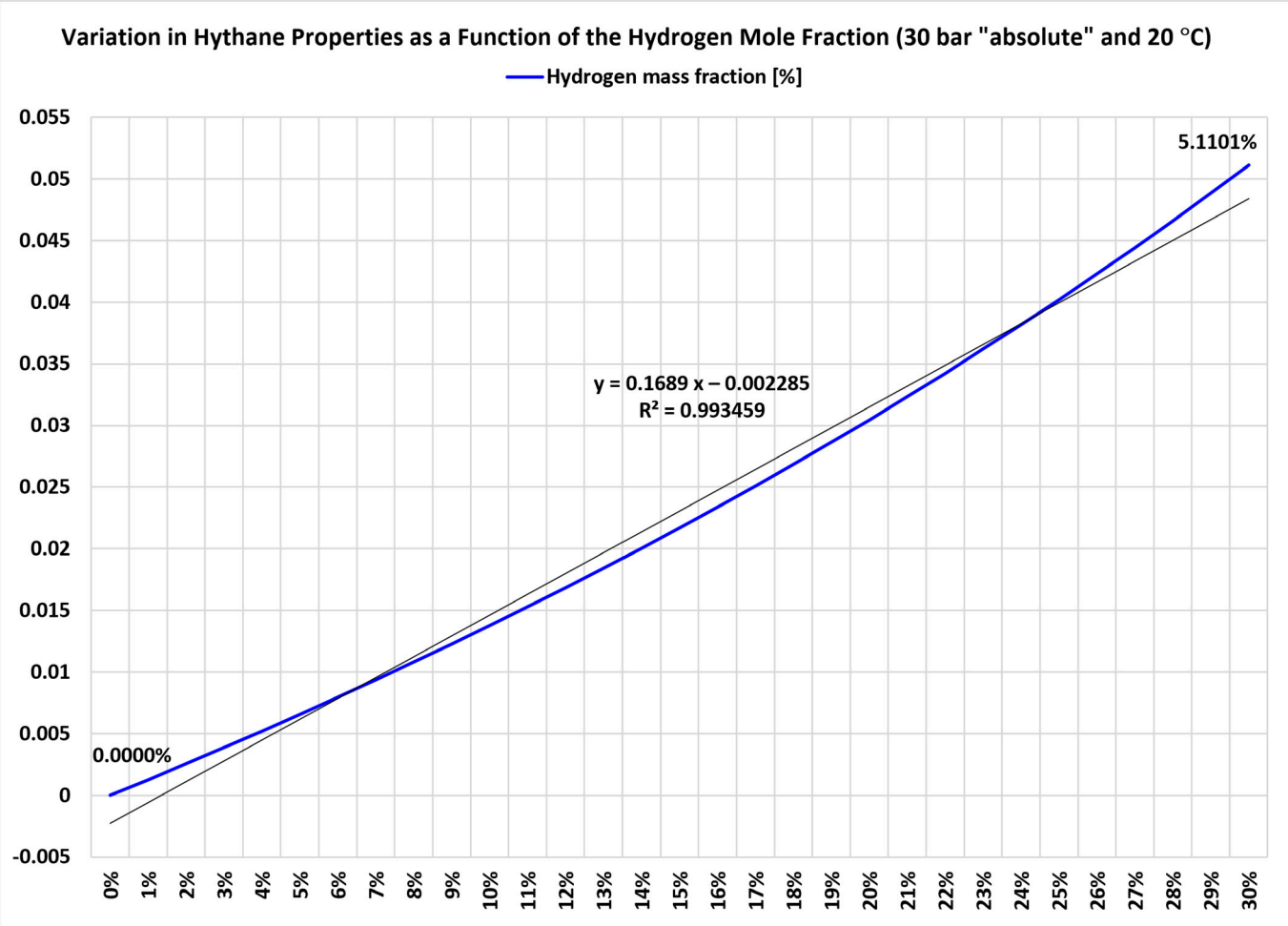

Figure 4. Variation in the hydrogen mass fraction for hythane, as a function of the hydrogen mole fraction. This plot was made by the author, with the data produced using CoolProp [57].

3.2.3. Molecular Weight, Density, Specific Volume, and Thermal Conductivity

Figures 5 and 6 show how the molecular weight (MW) and density (ρ) for hythane change as the hydrogen enrichment increases from 0% to 30% by mole, respectively.

Figures 7 and 8 show how the specific volume ($\bar{v}$) and thermal conductivity (λ) for hythane change as the hydrogen enrichment increases from 0% to 30% by mole, respectively.

The molecular weight decreases exactly linearly (R^2 1.0000) with the hydrogen mole fraction. This can be explained by the following expression for the hythane molecular weight as a binary gaseous mixture of methane and hydrogen [141]:

$$MW = (1 - X_{H2})MW_{CH4} + X_{H2}\,MW_{H2} = MW_{CH4} - X_{H2}(MW_{CH4} - MW_{H2}) \quad (11)$$

The above expression is a linear equation for the hythane molecular weight, with the independent variable being the hydrogen mole fraction.

The molecular weight changes by −26.2%, from 16.0428 kg/kmol (at 0% hydrogen) to 11.8347 kg/kmol (at 30% hydrogen) and decreases further to 2.0159 kg/kmol (at 100% hydrogen).

The implications of decreased molecular weight of hythane (compared to methane) include higher mobility of molecules, which results in a lower density and stronger diffusion [142] and leakage possibilities [143].

The density changes nearly linearly (R^2 0.9998) by −28.8%, from 20.875 kg/m^3 (at 0% hydrogen) to 14.868 kg/m^3 (at 30% hydrogen) and decreases further to 2.438 kg/m^3 (at 100% hydrogen).

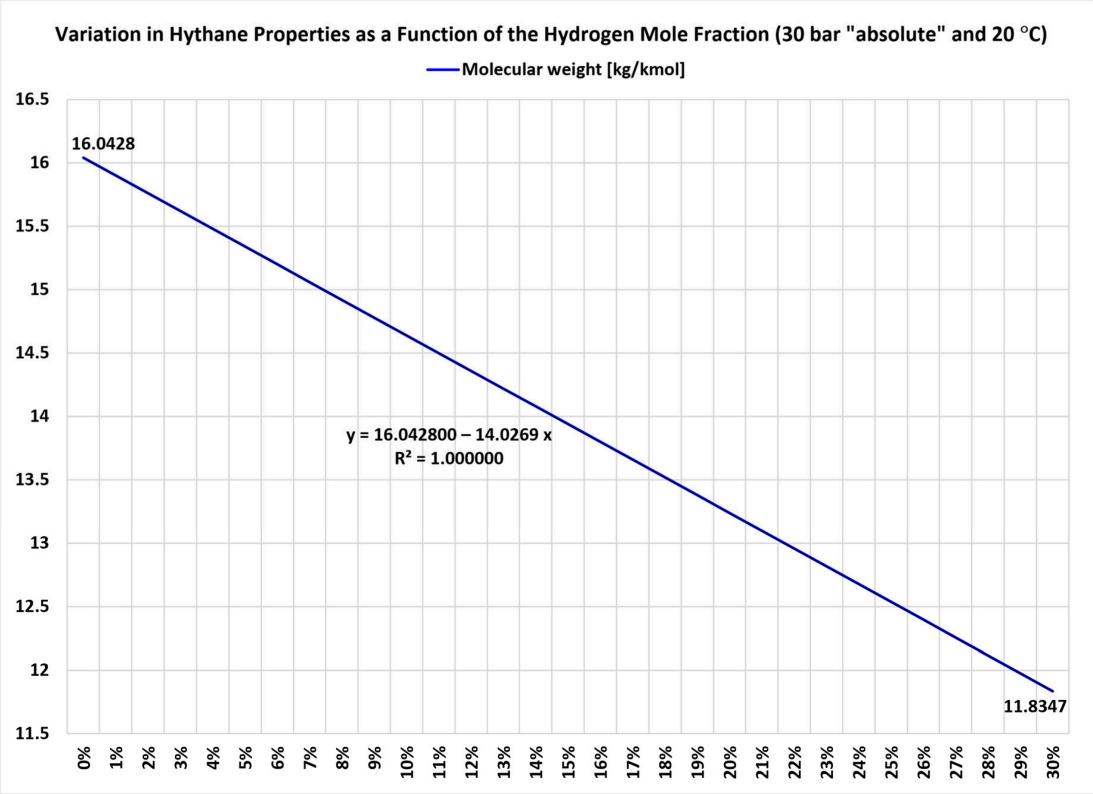

Figure 5. Variation in the molecular weight for hythane, as a function of the hydrogen mole fraction. This plot was made by the author, with the data produced using CoolProp [57].

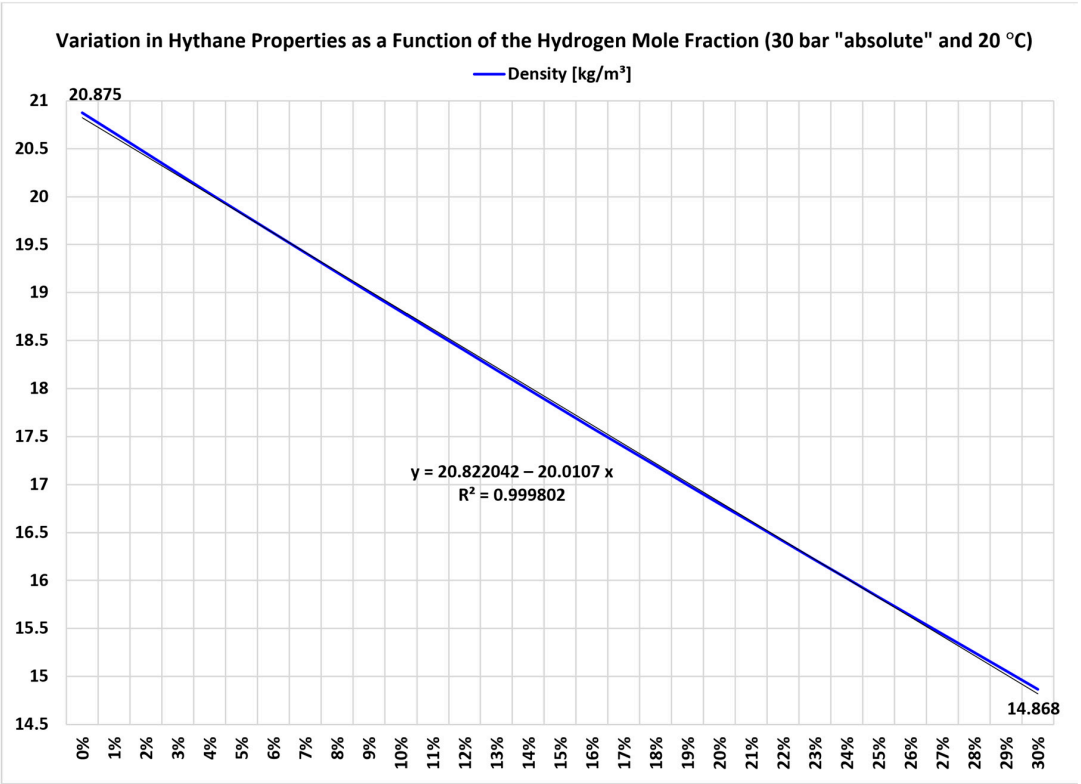

Figure 6. Variation in the density for hythane, as a function of the hydrogen mole fraction. This plot was made by the author, with the data produced using CoolProp [57].

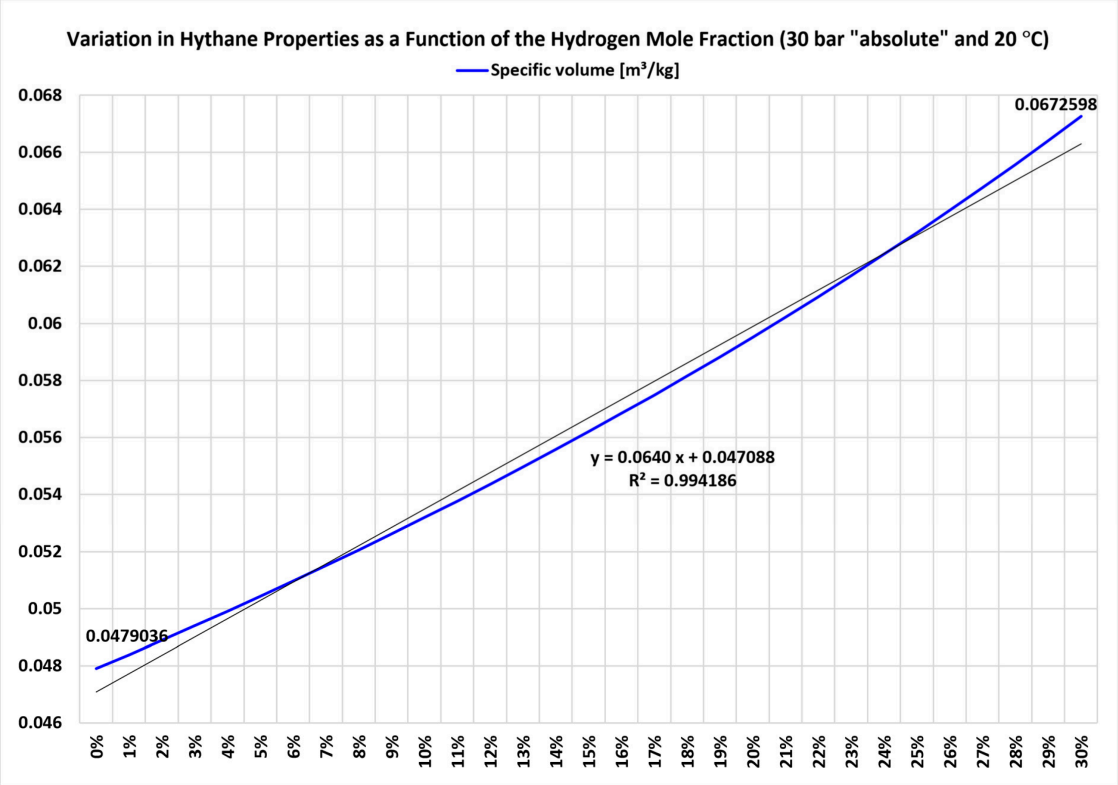

Figure 7. Variation in the specific volume for hythane, as a function of the hydrogen mole fraction. This plot was made by the author, with the data produced using CoolProp [57].

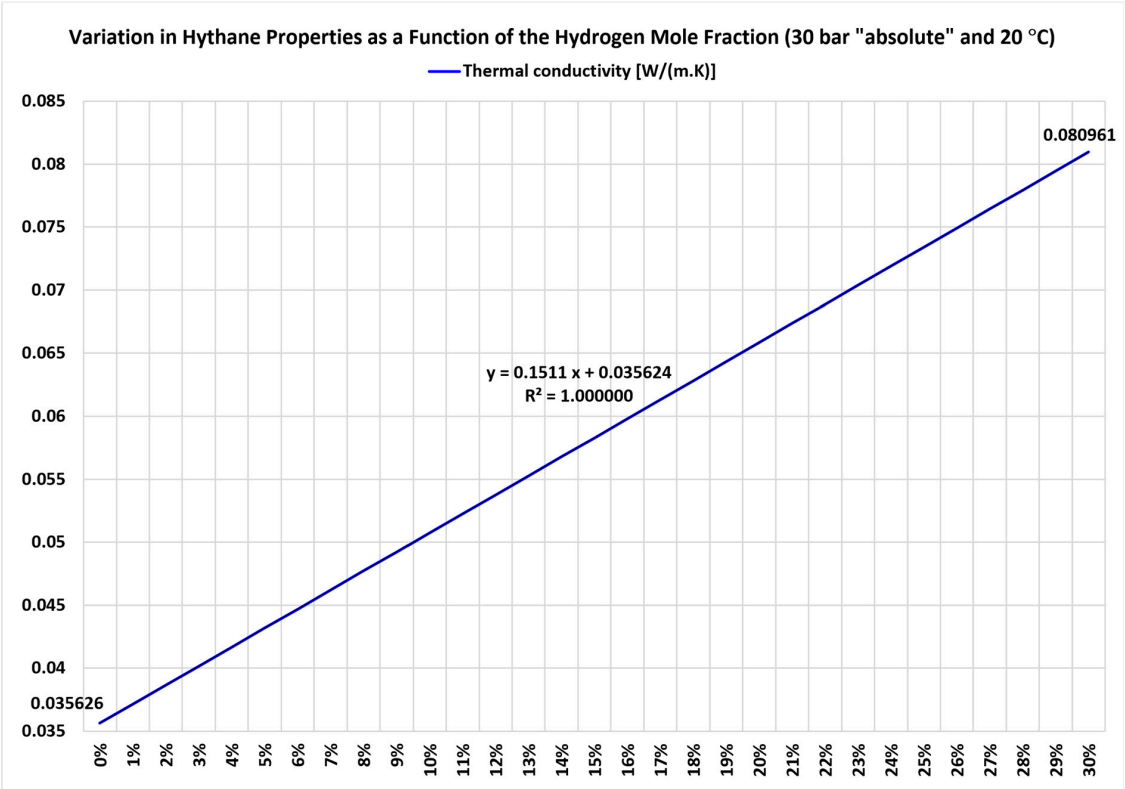

Figure 8. Variation in the thermal conductivity for hythane, as a function of the hydrogen mole fraction. This plot was made by the author, with the data produced using CoolProp [57].

The specific volume is the reciprocal of the density, which is mathematically expressed as follows:

$$\vartheta = \frac{1}{\rho} \tag{12}$$

The specific volume increases according to a weakly nonlinear accelerating profile (R^2 0.9942) by 40.4%, from 0.0479036 m^3/kg (at 0% hydrogen) to 0.0672598 m^3/kg (at 30% hydrogen) and increases further to 0.4102440 m^3/kg (at 100% hydrogen).

Although the specific volume is derived from the density that was presented earlier and is not truly another independent property of hythane, it is still useful to discuss it along with the density for convenience and completion of the study [144]. It is common in thermodynamic contexts to report the specific volume [145] rather than the density because specific properties (those expressed per unit mass of the fluid) are more suitable for numerical analysis and design, irrespective of the mass (size) of the system under consideration [146].

The implications of decreased density and increased specific volume of hythane (compared to methane) include higher travel velocities of hythane if transported using an existing methane (natural gas) pipe at the same mass flow rate used in the case of methane (natural gas). Such elevated velocities have direct consequences for friction losses [147], which increase proportionally with the square of the hythane velocity. This would demand greater compressor power and could lead to higher operational costs (power consumption). Furthermore, higher-velocity hythane flows accelerate aerodynamic noise generation [148] and exacerbate localized pipe oscillations [149]. This can compromise structural integrity over time. The elevated velocities also increase the risk of internal pipeline erosion, particularly if trace particulates are carried with hythane [150], and can disrupt the accuracy of conventional ultrasonic or turbine flow meters [151]. As a result, the optimal percentage of hydrogen enrichment should be carefully assessed against these hydrodynamic constraints by balancing the expected environmental benefits of decarbonization against the physical limitations of existing pipeline infrastructure and downstream equipment.

The thermal conductivity increases almost linearly (R^2 0.9999999970, but not perfectly 1.0) by 127.3%, from 0.035626 W/(m·K) at 0% hydrogen to 0.080961 W/(m·K) at 30% hydrogen and further to 0.186819 W/(m·K) at 100% hydrogen.

The implication of increased thermal conductivity of hythane (compared to methane) is that there is accelerated heat transfer between hythane and its surrounding pipeline or storage vessel [152]. This may cause more heat loss to the ambient surroundings, which results in remarkable temperature drops over long distances [153]. In addition, mechanical stresses due to thermal expansions or contractions become greater [154]. Also, the insulation requirements of the hythane transporting pipelines become more important, with a need for more effective (and probably heavier) insulation materials to mitigate the heat loss over long transport distances [155]. Because the thermal conductivity measures the ability of a material to conduct heat, and the current study shows that molecular hydrogen has a thermal conductivity that is more than five times higher than that of methane at typical conditions of natural gas pipelines, when hydrogen is blended into methane to form hythane, it significantly increases the overall thermal conductivity of the gas mixture. This elevated thermal conductivity results in two effects, namely, (1) faster thermal response, and (2) more sensitivity to thermal driving forces. With regard to the former effect, the intensified thermal conductivity accelerates the rate of conductive heat transfer between the bulk fluid and the internal walls of the pipeline or storage vessel. Regarding the latter effect, the hythane gas mixture responds much faster to external thermal gradients. This means that any temperature differential between the transported hythane and the external environment is quickly equalized through the containment walls.

3.2.4. Specific Heat Capacity at Constant Volume, and Specific Heat Capacity at Constant Pressure

Figure 9 shows how the specific heat capacity of hythane at constant volume (C_v) and its specific heat capacity at constant pressure (C_p) change as the hydrogen enrichment increases from 0% to 30% by mole.

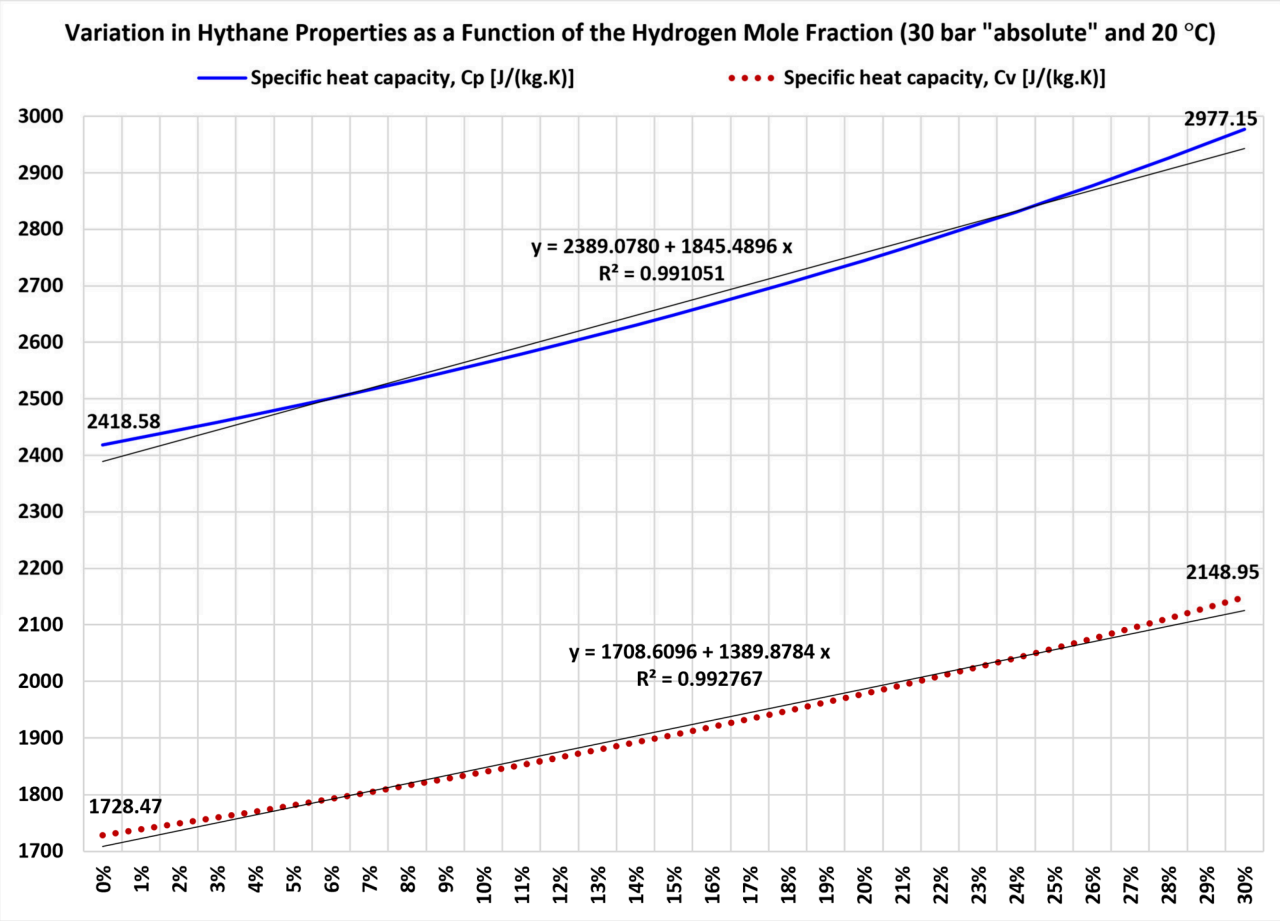

Figure 9. Variation in the specific heat capacity of hythane at constant volume and specific heat capacity at constant pressure, as a function of the hydrogen mole fraction. This plot was made by the author, with the data produced using CoolProp [57].

Both properties increase in a weakly nonlinear accelerating profile (R^2 0.9928 for C_v and R^2 0.9911 for C_p) over the entire range of hydrogen enrichment.

The specific heat capacity at constant volume increases by 24.3%, from 1728.47 J/(kg·K) (at 0% hydrogen) to 2148.95 J/(kg·K) (at 30% hydrogen) and increases further to 10185.56 J/(kg·K) (at 100% hydrogen). The specific heat capacity at constant pressure increases by 23.1%, from 2418.58 J/(kg·K) (at 0% hydrogen) to 2977.15 J/(kg·K) (at 30% hydrogen) and increases further to 14368.76 J/(kg·K) (at 100% hydrogen).

The implication of the increased specific heat capacity of hythane (compared to methane) is that a larger amount of energy needs to be added to elevate the temperature of hythane, and a larger amount of energy should be extracted to reduce the temperature of hythane. This increase in heat capacity has a favorable impact on the thermal stability, safety dynamics, and compression needs during pipeline transmission [156]. The specific heat capacity here (either the one at constant pressure or the one at constant volume) defines the amount of heat (thermal energy, in joules) required to change the temperature of a unit mass (1 kg) of a substance by one degree (1 K or 1 °C). The current study shows that

molecular hydrogen possesses an exceptionally high specific heat capacity that is roughly six times greater than that of methane, on a per-mass basis, at typical conditions of natural gas pipelines. Therefore, blending hydrogen into natural gas to form hythane markedly increases the overall specific heat capacity of the formed hythane compared to the original pure methane. This boost in the specific heat capacity involves three effects, which are (1) higher thermal buffering, (2) delayed cooling, and (3) improved intrinsic safety. For the first effect, a unit mass of hythane acts as a more powerful thermal sink because it absorbs a significantly larger amount of heat before experiencing a measurable increase in temperature. On the other hand, the second effect implies that when hythane cools, it releases a much larger amount of stored internal energy because it possesses much higher thermal inertia compared to methane. This may raise a compatibility issue for the cooling equipment of natural gas when used for hythane. Regarding the third effect, the higher thermal inertia of hythane and its higher heat capacity allow it to absorb unexpected localized hot spots without immediately reaching its auto-ignition temperature (AIT) [157]. This is an advantageous safety feature leading to a delay or mitigation of potential thermal runaway and ignition hazards.

3.2.5. Adiabatic Index

Figure 10 shows how the adiabatic index (γ) for hythane changes as the hydrogen enrichment increases from 0% to 30% by mole.

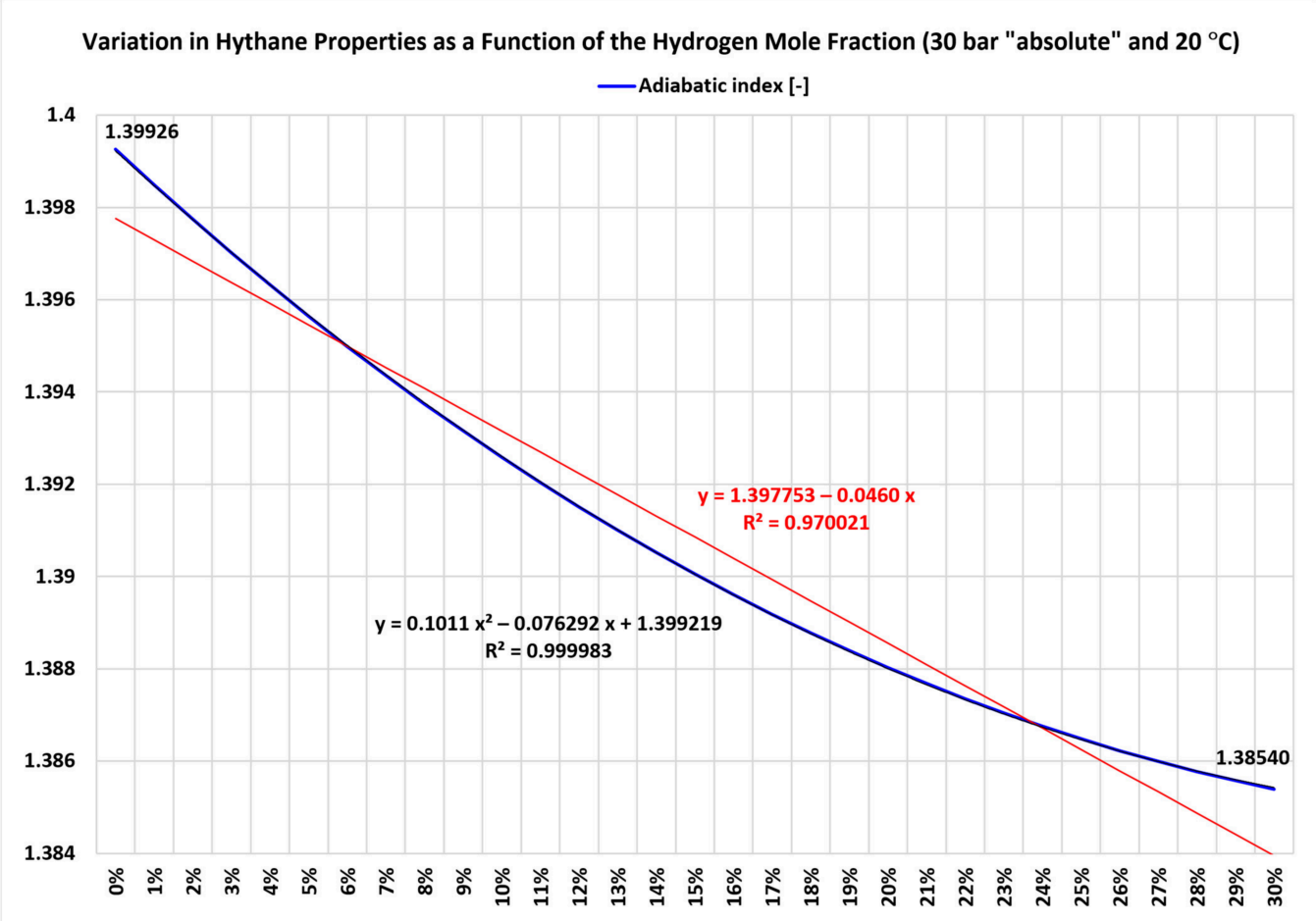

Figure 10. Variation in the adiabatic index for hythane, as a function of the hydrogen mole fraction. This plot was made by the author, with the data produced using CoolProp [57].

This property decreases nonlinearly over the range of hydrogen considered (namely, from 0% to 30% H_2 mole fraction), with a near-perfect (R^2 0.999983) attained using a quadratic regression model. The linear regression model is rejected due to over-simplification, as evidenced visually and by the unacceptably low (R^2 0.9700) below the set threshold of 0.99.

The adiabatic index changes by only −1.0%, from 1.39926 at 0% hydrogen to 1.38540 at 30% hydrogen, but this trend then reverses and increases at higher hydrogen enrichment and reaches 1.41070 at 100% hydrogen. The relative change in the adiabatic index is small enough to allow its approximation as a constant for hythane, with an average value of 1.3923. This value is the average of the adiabatic index values at the two extreme hythane compositions (namely, $\gamma = 1.39926$ at 0% hydrogen and $\gamma = 1.38540$ at 30% hydrogen).

The very weak change in the adiabatic index means that the specific heat capacity at constant volume (C_v) and specific heat capacity at constant pressure (C_p) increase with the hydrogen mole fraction but nearly maintain a fixed ratio between them. This is consistent with the results reported in the previous sub-subsection.

3.2.6. Specific Internal Energy, and Specific Enthalpy

Figure 11 shows how the specific internal energy (u) and the specific enthalpy (h) for hythane change as the hydrogen enrichment increases from 0% to 30% by mole.

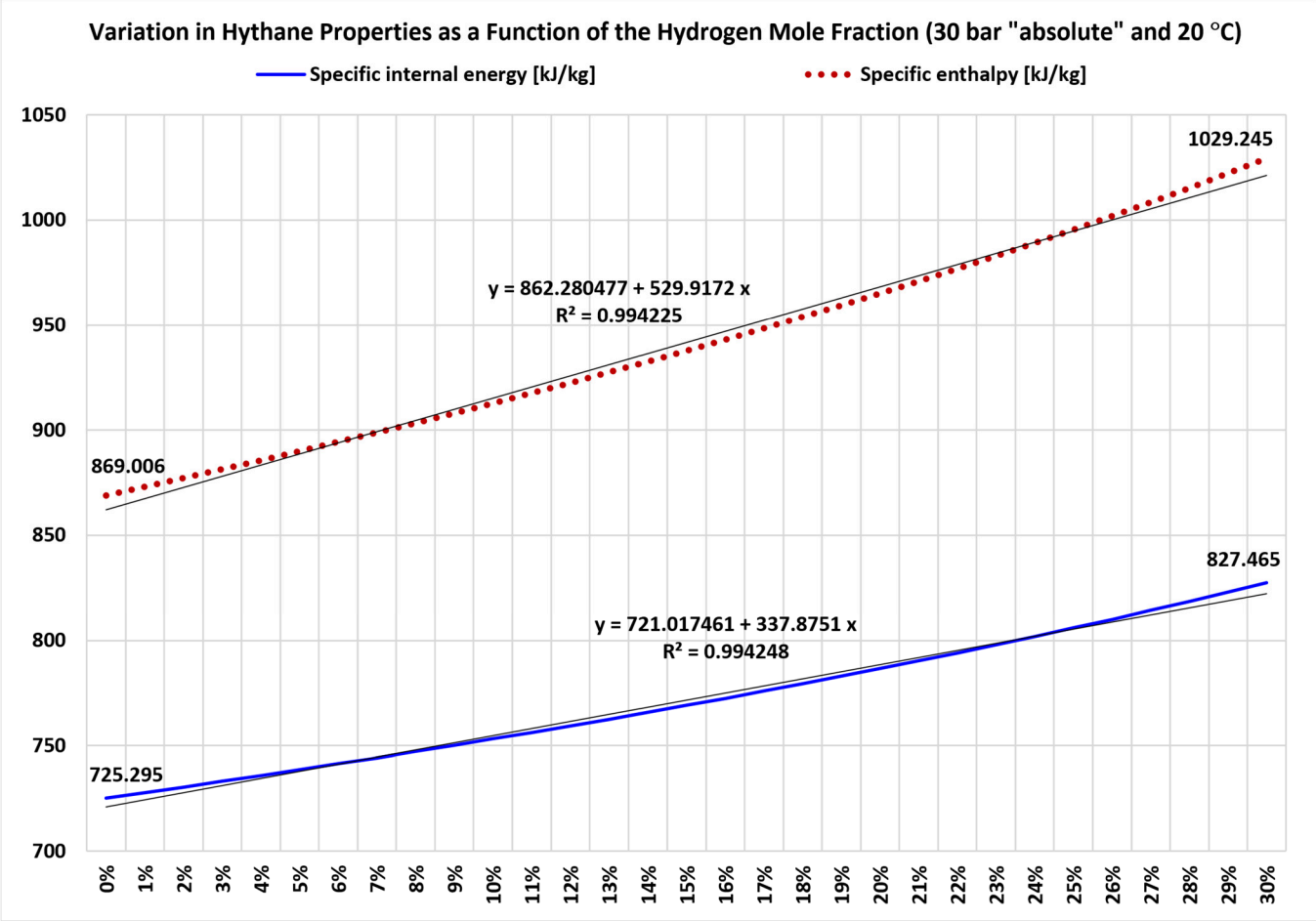

Figure 11. Variation in the specific internal energy and specific enthalpy for hythane, as a function of the hydrogen mole fraction. This plot was made by the author, with the data produced using CoolProp [57].

Both properties increase nearly linearly (R^2 0.99425 for u and R^2 0.99423 for h) with the hydrogen mole fraction.

The specific internal energy increases by 14.1%, from 725.295 kJ/kg at 0% hydrogen to 827.465 kJ/kg at 30% hydrogen and increases further to 2641.932 kJ/kg at 100% hydrogen. The specific enthalpy increases at a slightly higher rate of 18.4%, from 869.006 kJ/kg at 0% hydrogen to 1029.245 kJ/kg at 30% hydrogen and increases further to 3872.664 kJ/kg at 100% hydrogen.

The specific enthalpy is the sum of the specific internal energy (u) and the specific flow energy [158], which is also called specific pressure energy or specific flow work ($P\,\bar{v}$) [159]:

$$h = u + P\,\bar{v} \tag{13}$$

The implications of increased specific internal energy or specific enthalpy of hythane (compared to methane) include the rise in the energy content of hythane [160], through elevated thermal energy per unit mass and elevated flow energy per unit mass. Thus, as an energy carrier, transported hythane can deliver more energy than methane for the same mass. Because hydrogen possesses an exceptionally high gravimetric energy density (lower heating value, LHV) of about 120 MJ/kg [161,162] compared to about 50 MJ/kg for methane [163,164], blending hydrogen into methane significantly boosts the total energy content stored per unit mass.

However, an opposing trend holds for per unit volume, which is more relevant for pipeline transport. Taking the LHV of hydrogen and methane as 119.96 MJ/kg and 50.03 MJ/kg, respectively, and combining these values with the hydrogen mass fraction and the density computed here at 30 bar and 20 °C, the LHV of hythane rises from 50.03 MJ/kg (0% H_2) to 51.55 MJ/kg (15% H_2) and 53.60 MJ/kg (30% H_2), whereas its volumetric energy density at pipeline conditions drops from 1044.4 MJ/m^3 to 917.1 MJ/m^3 (a 12.2% decrease) and 797.0 MJ/m^3 (a 23.7% decrease), respectively. Thus, delivering the same energy flow rate requires a volumetric flow rate that is higher by 13.9% at 15% H_2 and by 31.0% at 30% H_2. For a given pipeline operated with a fixed pressure drop, and assuming fully turbulent flow with an unchanged friction factor (so that the pressure drop is proportional to the density multiplied by the square of the flow velocity), the flow velocity scales with the inverse square root of the density, and the deliverable energy flow rate scales with the volumetric energy density divided by the square root of the density. Under these simplifying assumptions, the energy delivery capacity of the pipeline decreases by about 4.9% at 15% H_2 and 9.6% at 30% H_2, compared with methane. Conversely, maintaining the same energy delivery would require higher flow velocities, which would increase the pressure drop and the compression duty. The slight decrease in the absolute viscosity with hydrogen enrichment marginally raises the Reynolds number, which would slightly lower the friction factor and partially offset these effects. These estimates are first-order indications, and a quantitative assessment of the pressure drop and compressor power requires a dedicated pipeline-hydraulic simulation for a specific network.

Although not among the 20 properties reported here, it might be useful to mention that the specific flow energy ($P\,\bar{v}$) was analyzed over the entire range of hythane compositions (from 0% to 30% hydrogen mole fraction). It was found to monotonically increase with the hydrogen mole fraction in an approximately linear manner (R^2 0.99419). It increased by 40.4% from 143.711 kJ/kg at 0% hydrogen to 201.779 kJ/kg at 30% hydrogen and increased further to 1230.732 kJ/kg at 100% hydrogen.

3.2.7. Specific Entropy

Figure 12 shows how the specific entropy (s) for hythane changes as hydrogen enrichment increases from 0% to 30% by mole.

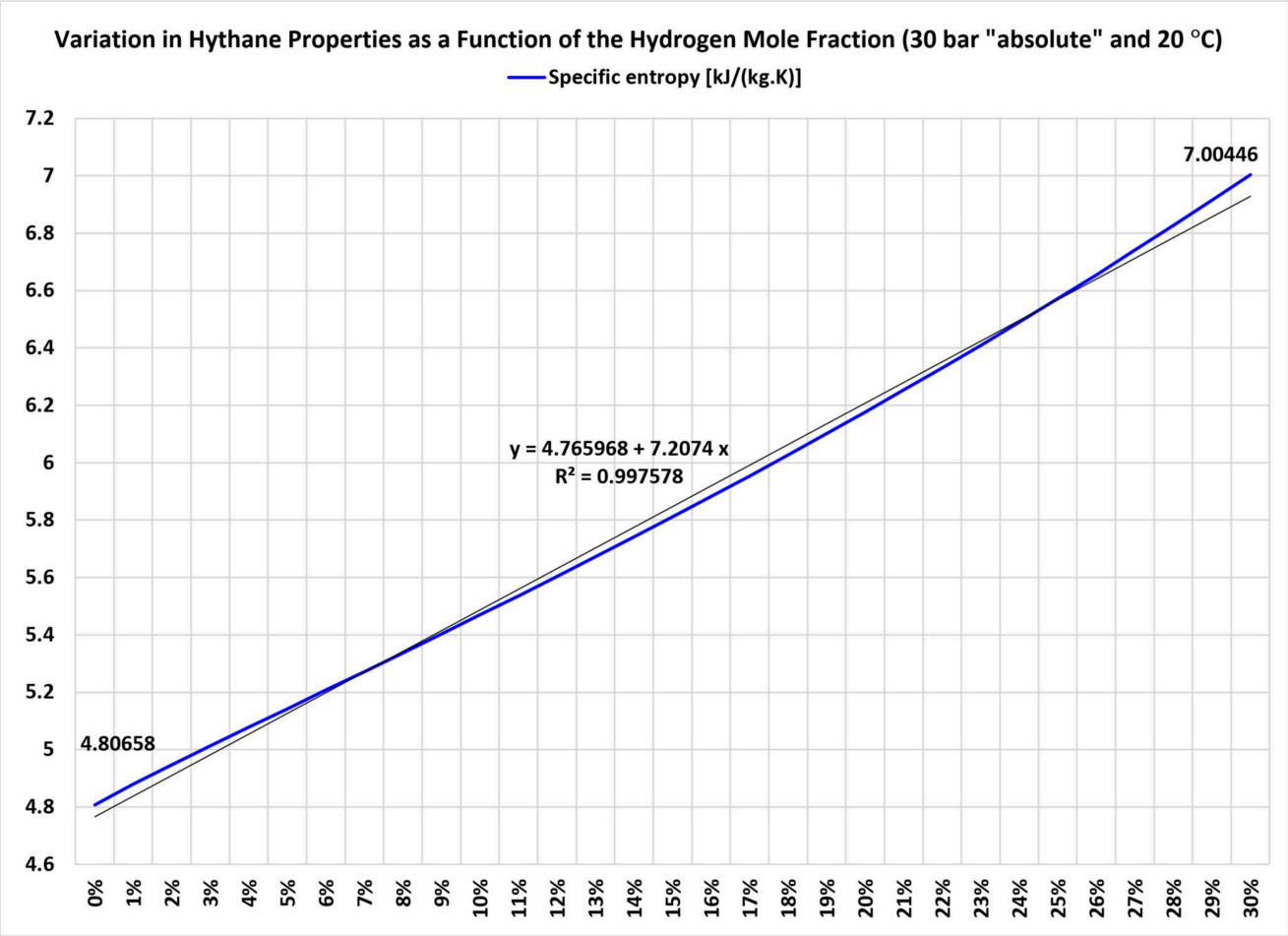

Figure 12. Variation in the specific entropy for hythane, as a function of the hydrogen mole fraction. This plot was made by the author, with the data produced using CoolProp [57].

The specific entropy increases nearly linearly (R^2 0.9976) by 45.7% from 4.80658 kJ/(kg·K) at 0% hydrogen to 7.00446 kJ/(kg·K) at 30% hydrogen and increases further to 39.13132 kJ/(kg·K) at 100% hydrogen.

The implications of increased specific entropy of hythane (compared to methane) include intensified dispersal of energy accompanied by higher molecular disorder [165]. Practically, this means that a unit mass of hythane has a lower capability to do useful work [166] or has a lower reduced exergy [167] than a unit mass of methane. The increase in the specific entropy due to adding hydrogen into methane is a fundamental thermodynamic effect that stems from (1) the addition of lighter hydrogen molecules and (2) the increased complexity of the gas mixture. Because hydrogen is significantly lighter and smaller than methane, when hydrogen is introduced into methane, the binary gaseous system (hythane) gains more microstates, or a higher number of specific ways by which the energy of the system can be arranged [168]. In addition, blending two distinct gases (hydrogen and methane) introduces an additional thermodynamic effect, namely, the entropy of mixing [169]. This irreversible dispersal means the thermal energy within hythane is more scattered and less organized than in pure methane.

3.2.8. (13) Absolute Viscosity

Figure 13 shows how the absolute viscosity, or dynamic viscosity, (μ) for hythane changes as the hydrogen enrichment increases from 0% to 30% by mole.

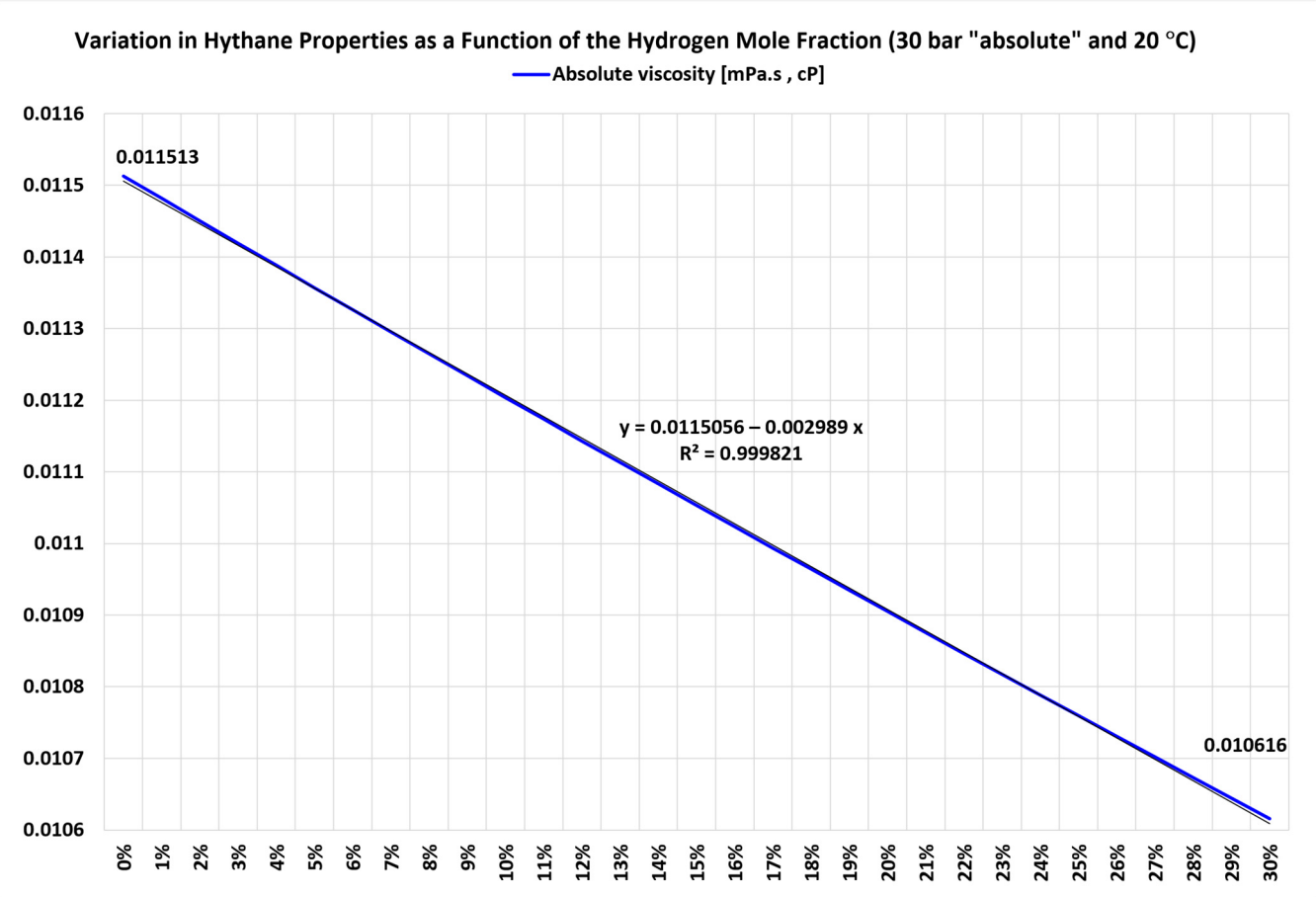

Figure 13. Variation in the absolute viscosity for hythane, as a function of the hydrogen mole fraction. This plot was made by the author, with the data produced using CoolProp [57].

The absolute viscosity changes nearly linearly (R^2 0.9998) by −7.8%, from 0.011513 cP at 0% hydrogen to 0.010616 cP at 30% hydrogen and decreases further to 0.008820 cP at 100% hydrogen.

Based on principles of fluid mechanics, the implication of decreased absolute viscosity of hythane (compared to methane) means that hythane has lower internal resistance to flow [170], thus loses less energy via friction and requires less power to be transported [171]. Given that the absolute viscosity measures the internal resistance of a fluid to gradual deformation by shear or tensile stress, and that the current study shows that hydrogen has about 75% of the dynamic viscosity of that corresponding to pure methane at typical pipeline operating temperatures and pressures, then when hydrogen is blended into methane (or natural gas) to form hythane, the resulting mixture exhibits a lower absolute viscosity than pure methane (or natural gas), but this change is not significant. This drop in hythane's absolute viscosity results in (1) lower molecular drag, (2) reduced wall shear stress [172] that is exerted both within the fluid layers and at the fluid-solid boundary (the inner wall of the pipeline), (3) thinner viscous sublayer near the pipe wall, which means that the flow transitions more quickly from laminar-like behavior near the wall to turbulent behavior in the buffer and log-law regions [173], and (4) less energy dissipation due to friction, where kinetic energy is converted into thermal energy.

3.2.9. Compressibility Factor

Figure 14 shows how the compressibility factor (Z) for hythane changes as the hydrogen enrichment increases from 0% to 30% by mole.

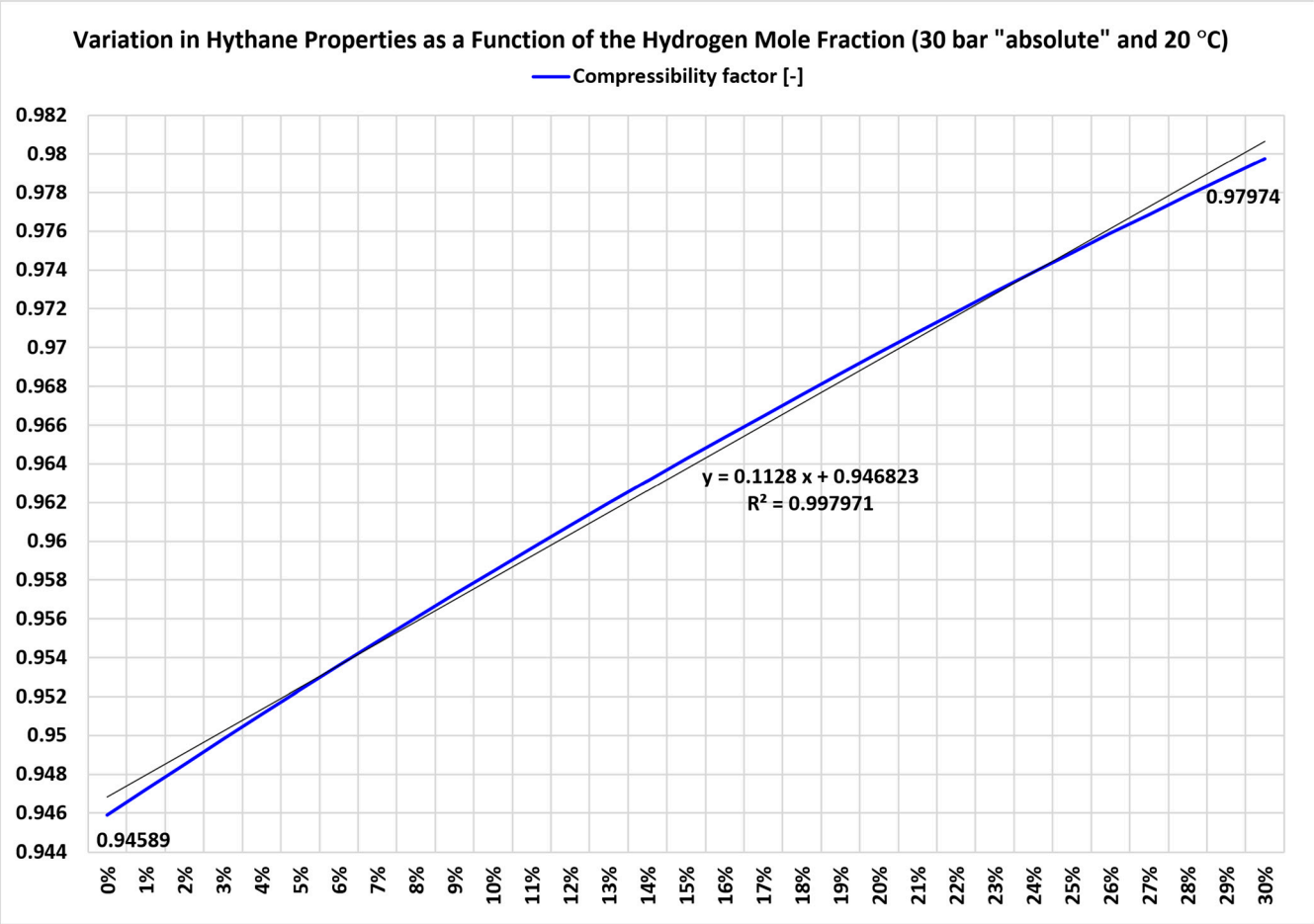

Figure 14. Variation in the compressibility factor for hythane, as a function of the hydrogen mole fraction. This plot was made by the author, with the data produced using CoolProp [57].

The compressibility factor increases nearly linearly (R^2 0.9980) over the entire range of hydrogen considered here for hythane (namely, from 0% to 30% H_2 mole fraction).

The compressibility factor increases by 3.6%, from 0.94589 at 0% hydrogen to 0.97974 at 30% hydrogen and increases further to 1.01790 at 100% hydrogen. As in the case of the methane mass fraction and the adiabatic index, the relative change in the compressibility factor is small enough to allow approximating it as a constant for hythane, with an average value of 0.9628.

The compressibility factor for all hythane compositions covered is close to unity ($Z \approx 1$), which permits approximating hythane (at the selected absolute pressure of 30 bar and temperature of 20 °C) as an ideal gas with a minor loss of accuracy compared to more accurate modeling as a real gas (in CoolProp).

3.2.10. Specific Gas Constant, and Speed of Sound

Figures 15 and 16 show how the specific gas constant (R_g) and the speed of sound (c) for hythane change as the hydrogen enrichment increases from 0% to 30% by mole, respectively.

Either of these two properties responds similarly because of the hydrogen enrichment, where both increase in an approximately linear fashion (R^2 0.9935 for R_g, R^2 0.9973 for c).

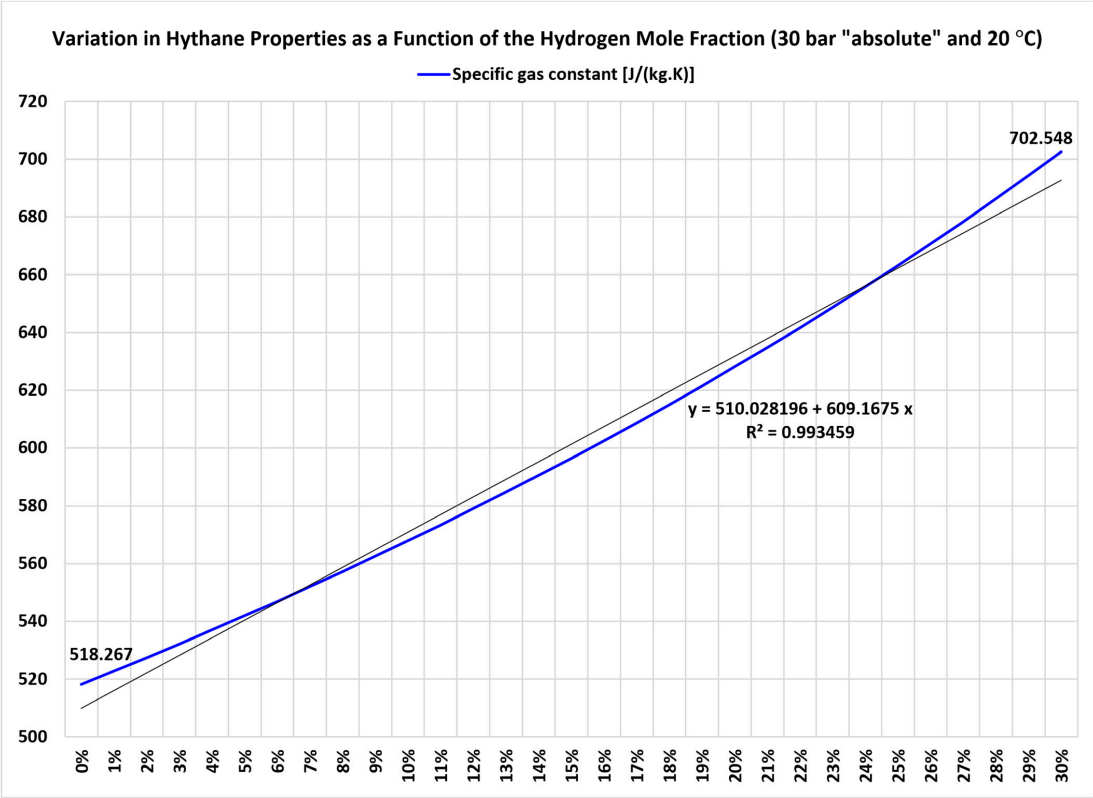

Figure 15. Variation in the specific gas constant for hythane, as a function of the hydrogen mole fraction. This plot was made by the author, with the data produced using CoolProp [57].

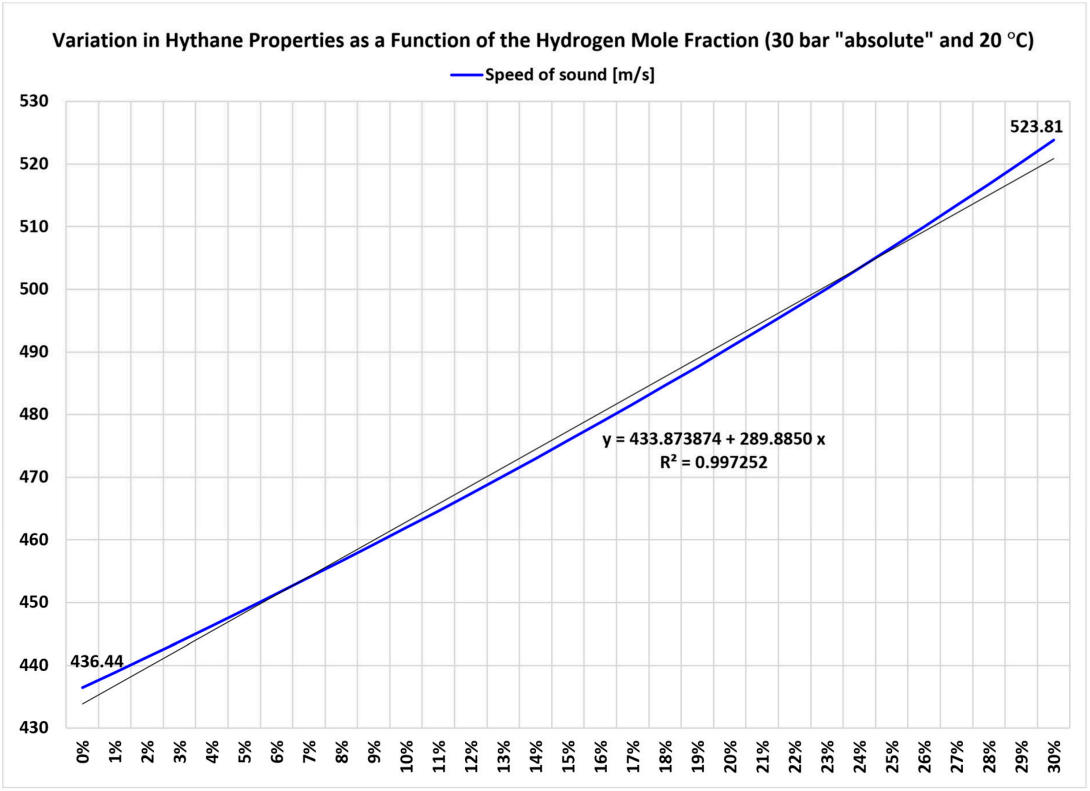

Figure 16. Variation in the speed of sound for hythane, as a function of the hydrogen mole fraction. This plot was made by the author, with the data produced using CoolProp [57].

The speed of sound in a gas depends nonlinearly (through a square root function) on the adiabatic index (presented earlier), which is nearly independent of hydrogen enrichment as discussed previously. It also depends on the specific gas constant, which increases with hydrogen enrichment, as shown in the current sub-subsection. The result of these effects is the obtained increasing profile of the speed of sound.

For an ideal gas, as an approximation to the real hythane gas computations, the speed of sound is a nonlinear function of the product of the adiabatic index and the specific gas constant, as follows [174]:

$$c = \sqrt{\gamma\, R_g\, T} \tag{14}$$

For a real gas, the speed of sound has a more detailed expression [175]. A simplified form for the speed of sound in a real gas is [176]:

$$c = \sqrt{Z\, \gamma\, R_g\, T} \tag{15}$$

The compressibility factor (Z) in the current study is close to unity, as shown in the previous sub-subsection, reflecting a small deviation from the ideal gas.

The specific gas constant increases by 35.6%, from 518.267 J/(kg·K) at 0% hydrogen to 702.548 J/(kg·K) at 30% hydrogen and increases further to 4124.482 J/(kg·K) at 100% hydrogen.

The speed of sound increases by 20.0%, from 436.44 m/s at 0% hydrogen to 523.81 m/s at 30% hydrogen and increases further to 1329.48 m/s at 100% hydrogen.

The implication of the increased specific gas constant of hythane (compared to methane) is that the pressure becomes more responsive to a change in either the density or the absolute temperature. In the approximate case of an ideal gas, the pressure is directly proportional to either the density or the absolute temperature as follows [177]:

$$P = \rho\, R_g\, T \tag{16}$$

3.2.11. Momentum Diffusivity, Prandtl Number, and Thermal Diffusivity

Figures 17 and 18 show how the momentum diffusivity, kinematic viscosity (ν), and Prandtl number (Pr) for hythane change as the hydrogen enrichment increases from 0% to 30% by mole, respectively.

Figure 19 shows how the thermal diffusivity (α) for hythane changes as the hydrogen enrichment increases from 0% to 30% by mole.

The momentum diffusivity increases nearly linearly (R^2 0.9942) by 29.5%, from 0.55152 cSt at 0% hydrogen to 0.71404 cSt at 30% hydrogen and increases further to 3.61836 cSt at 100% hydrogen. The increase in the momentum diffusivity with hydrogen enrichment, despite the decrease in the absolute viscosity with hydrogen enrichment, is attributed to the faster decline in the density (the denominator of the momentum diffusivity) compared to a slower decline in the absolute viscosity (the numerator of the momentum diffusivity).

The implications of the increasing momentum diffusivity for hythane compared to natural gas include the decrease in the Reynolds number (Re) for the hythane flow inside the pipelines. The Reynolds number is an important non-dimensional quantity that describes the ratio of the inertial forces to the viscous forces in a moving fluid [178], and it is related to the momentum diffusivity (ν), average or bulk gas speed (V), and pipe's internal diameter (D) as follows [179]:

$$Re = \frac{V\, D}{\nu} \tag{17}$$

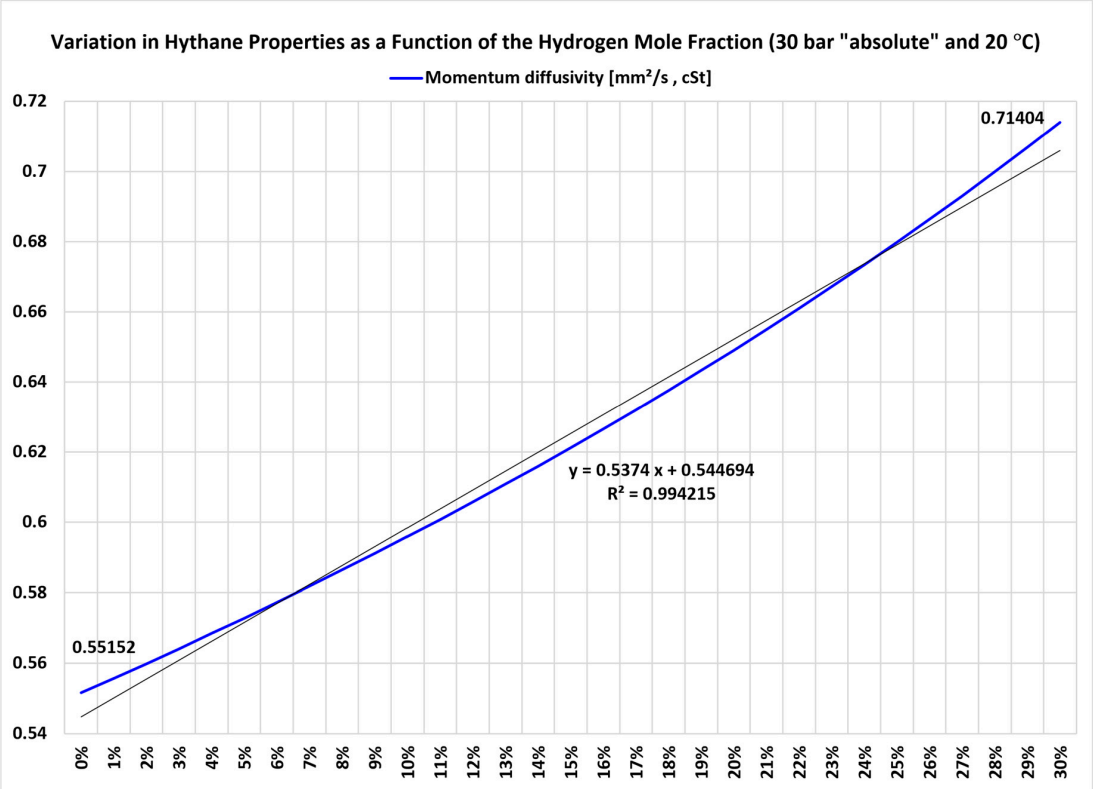

Figure 17. Variation in the momentum diffusivity for hythane, as a function of the hydrogen mole fraction. This plot was made by the author, with the data produced using CoolProp [57].

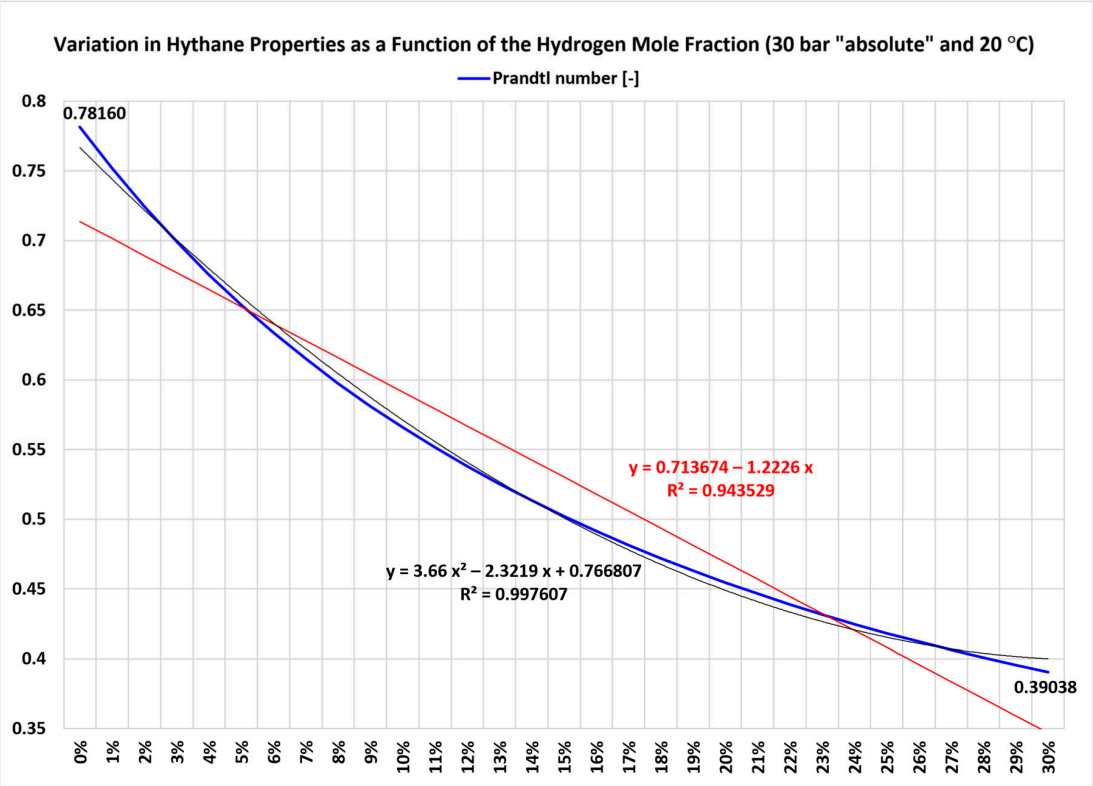

Figure 18. Variation in the Prandtl number for hythane, as a function of the hydrogen mole fraction. This plot was made by the author, with the data produced using CoolProp [57].

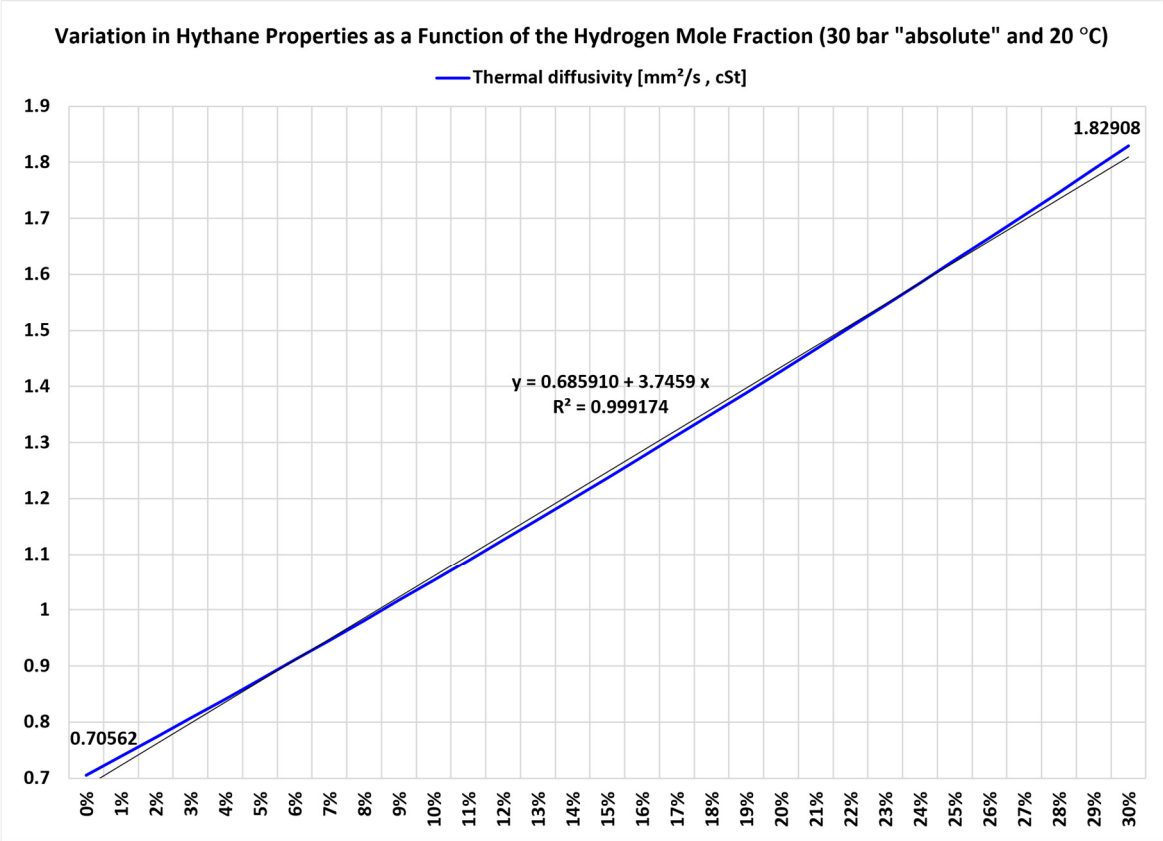

Figure 19. Variation in the thermal diffusivity for hythane, as a function of the hydrogen mole fraction. This plot was made by the author, with the data produced using CoolProp [57].

Natural gas in pipelines is typically in the turbulent region, where the Reynolds number is much higher than the threshold of Re = 4000 [180]; it often exceeds 10,000 and can reach 10^7 [181]. Thus, a small increase in the momentum diffusivity is not expected to change the turbulent flow regime of the gas (hythane) from turbulent to transitional ($2300 \leq Re \leq 4000$) or to laminar ($Re < 2300$) for the same bulk velocity of flowing hythane gas [182].

The Prandtl number decreases in a quadratic manner (with R^2 0.9976) over the investigated range of hydrogen enrichment. A linear regression for the Prandtl number was rejected due to the apparent deviation (inability to capture the nonlinearity), with an R^2 value of 0.9435, which is considered too low here (below 0.99), and thus, the more detailed quadratic polynomial regression model was proposed as a better alternative. For pure methane, Pr = 0.78160; while at 30% hydrogen, Pr = 0.39038; and for pure hydrogen, Pr = 0.67837 (it reverses its declining trend and increases at high hydrogen concentrations). Thus, the change in Pr over the entire hythane range (from 0% to 30% hydrogen) is −50.1%.

Therefore, small hydrogen enrichment rapidly reduces the relative power of momentum (viscous) diffusion compared to thermal diffusion, making momentum diffusion gradually weaker than thermal diffusion. This alteration in the Prandtl number behavior is consistent with the larger thermal conductivity of hydrogen (compared to methane) and the smaller absolute viscosity of hydrogen (compared to methane).

Visual inspection of the faster uptrend of the thermal diffusivity (the denominator of Pr) in contrast to the slower uptrend of the momentum diffusivity (the numerator of Pr) elucidates the gradual nonlinear decline in the Prandtl number from a higher value at 0% hydrogen to a lower value at 30% hydrogen. A unity Prandtl number coincides with the condition of equal thermal diffusivity and momentum diffusivity, but this condition is not

realized over the entire range of hydrogen enrichment for hythane. Instead, the Prandtl number remains below unity.

In practical applications, the implication of the drop in the Prandtl number as a result of limited hydrogen addition is a thicker thermal boundary layer compared to the velocity boundary layer because heat diffuses faster than momentum [183]. This reduction in Pr can be an advantage in heat exchangers due to the rapid heat transfer relative to frictional losses [184]. The current study shows that, in typical natural gas pipeline conditions, pure methane exhibits a higher Prandtl number (closer to 1.0) than hythane, where momentum and thermal diffusion rates are closer in magnitude. However, hydrogen blending into methane to form hythane causes the exceptionally high thermal conductivity of hydrogen to noticeably raise the mixture's overall thermal diffusivity. Simultaneously, the absolute viscosity drops, thereby causing a distinct drop in the Prandtl number. This drop in the Prandtl number due to hydrogen enrichment leads to several effects, such as (1) a thicker thermal boundary layer and (2) dominance of thermal diffusion because the thermal boundary layer expands and becomes significantly thicker than the velocity (momentum) boundary layer. This effect, physically, means that thermal energy diffuses much farther into the bulk core of the moving hythane stream than the frictional, shear-driven velocity disturbances do. For heat exchangers, the drop in the Prandtl number implies rapid thermal equalization. In many heat exchangers, the overall heat-transfer rate is limited (bottlenecked) by the thermal resistance of the fluid-side boundary layer adjacent to the wall [185]. This occurs especially on the low-conductivity side or the low-turbulence side. Therefore, the reduced-Pr hythane allows heat to pass through the velocity profile rapidly. This feature leads to accelerated thermal development and faster temperature equalization between the walls and the bulk gas region.

The thermal diffusivity increases by 159.2%, from 0.70562 mm^2/s at 0% hydrogen to 1.82908 mm^2/s at 30% hydrogen and increases further to 5.33390 mm^2/s at 100% hydrogen. Among the 20 hythane properties investigated in the current study, thermal diffusivity is the property that is affected the most (on a relative basis considering absolute values) by hydrogen enrichment. The strong increase in thermal diffusivity due to hydrogen enrichment is attributed to the double effect of (1) increasing thermal conductivity (the numerator of the thermal diffusivity) and (2) decreasing density (a multiplicative variable in the denominator of the thermal diffusivity). While the specific heat capacity at constant pressure (the other multiplicative variable in the denominator of the thermal diffusivity) increases with hydrogen enrichments, its effect on the thermal diffusivity is overpowered by the stronger effect of the thermal conductivity and the density.

3.2.12. Joule–Thomson Coefficient

Figure 20 shows how the Joule–Thomson coefficient (μ_{JT}) for hythane changes as the hydrogen enrichment increases from 0% to 30% by mole.

The Joule–Thomson coefficient changes nearly linearly (R^2 0.9989) by −44.2%, from 4.338991 K/MPa at 0% hydrogen to 2.421611 K/MPa at 30% hydrogen and decreases further to the negative value of –0.304978 K/MPa at 100% hydrogen.

The positive Joule–Thomson coefficient for pure compressed methane and for compressed hythane mixtures means that during a throttling process (adiabatic expansion at a constant specific enthalpy from a higher-pressure upstream point to a lower-pressure downstream point), the temperature decreases with a cooling effect [186]. This is the same behavior as industrial refrigerants and carbon dioxide [187], which also have a positive Joule–Thomson coefficient that makes them able to produce a cooling effect upon throttling [188]. The explanation of this cooling effect is that hythane is forced to expand rapidly into the lower-pressure region through a restriction during the throttling process.

Consequently, hythane molecules (methane molecules and hydrogen molecules) pull further apart, thereby requiring energy to overcome their mutual attractions [189]. Given that there is no heat addition during the throttling process, hythane takes this energy from its own internal energy [190]. So, the specific internal energy of hythane drops, and thus the temperature of hythane drops [191].

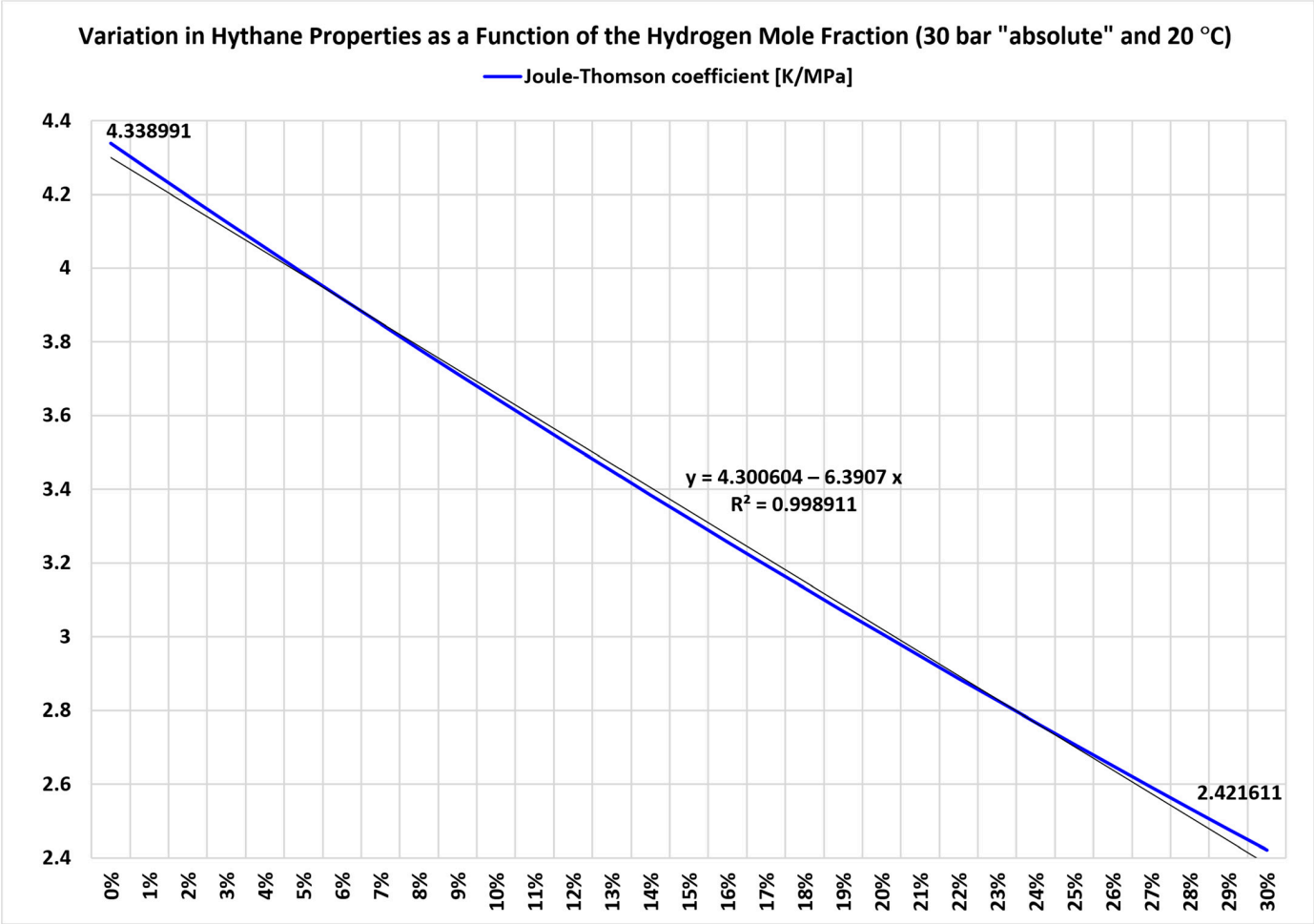

Figure 20. Variation in the Joule-Thomson coefficient for hythane, as a function of the hydrogen mole fraction. This plot was made by the author, with the data produced using CoolProp [57].

By analyzing additional very high values of the absolute pressure (such as 500 bar), it was found that the Joule–Thomson coefficient becomes negative beyond a certain pressure (that depends on the hythane composition). Beyond this threshold pressure value, the Joule–Thomson coefficient becomes negative, similar to the case of compressed pure hydrogen [192]. The reason is that the repulsive intermolecular forces dominate (the molecules are closely packed together) and overpower attractive forces. This causes the molecules to forcefully push each other apart, thereby increasing the internal energy. This causes the temperature of hythane to increase, rather than to decrease during throttling [193].

The implications of the decreased (yet still positive) Joule–Thomson coefficient of hythane (compared to methane) include less cooling upon the sudden transition from a high-pressure region to a lower-pressure region. Such a thermodynamic process might happen through a throttle valve [194,195]. The decreased positive Joule–Thomson coefficient of hythane relative to natural gas at typical natural gas pipeline conditions results in attenuated cooling during pressure regulation. This attenuated expansive cooling reduces the thermal

load on pressure-regulation stages by decreasing the need for reheating between multi-stage expansions [196]. It also lowers the risk of hydrate or ice formation downstream of pressure regulators [197]. While hythane under low and moderate pressures still exhibits expansive cooling, its intensity is less than that of natural gas. This reduced cooling effect lowers the external thermal energy input required to maintain safe downstream temperatures, thereby resulting in potential energy savings at regulation stations.

3.3. Tabulated Summary for Selected Hythane Compositions

As a numerical summary, a comparison is given in Table 5 for the numerical values of the 20 properties at particular compositions of hythane. The five compositions in the table correspond to (1) pure methane (the trivial lower limiting case for hythane), (2) low-hydrogen hythane with 10% hydrogen mole fraction, (3) trademark Hythane® with 20% hydrogen mole fraction, (4) upper limiting case for hythane with 30% hydrogen mole fraction, and (5) pure hydrogen (for benchmarking only).

Table 5. Values of the evaluated hythane properties at different compositions.

Index	Property Symbol	Unit	Hydrogen Mole Fraction (X_{H2})				
			0% (Pure CH_4)	10%	20%	30%	100% (Pure H_2)
1	MW	kg/kmol	16.0428	14.6401	13.2374	11.8347	2.0159
2	R_g	J/(kg·K)	518.267	567.923	628.103	702.548	4124.482
3	Y_{H2}	%	0.0000%	1.3770%	3.0457%	5.1101%	100.0000%
4	Y_{CH4}	%	100.0000%	98.6230%	96.9543%	94.8899%	0.0000%
5	c	m/s	436.44	461.92	490.71	523.81	1329.48
6	ρ	kg/m^3	20.875	18.801	16.802	14.868	2.438
7	ϑ	m^3/kg	0.0479036	0.0531900	0.0595181	0.0672598	0.4102440
8	u	kJ/kg	725.295	753.237	786.636	827.465	2641.932
9	h	kJ/kg	869.006	912.807	965.190	1029.245	3872.664
10	s	kJ/(kg·K)	4.80658	5.46926	6.17666	7.00446	39.13132
11	C_p	J/(kg·K)	2418.58	2562.78	2744.96	2977.15	14368.76
12	C_v	J/(kg·K)	1728.47	1840.30	1977.60	2148.95	10185.56
13	γ	[-]	1.39926	1.39258	1.38802	1.38540	1.41070
14	Z	[-]	0.94589	0.95845	0.96973	0.97974	1.01790
15	μ_{JT}	K/MPa	4.338991	3.646960	3.007965	2.421611	−0.304978
16	λ	W/(m·K)	0.035626	0.050736	0.065847	0.080961	0.186819
17	μ	cP	0.011513	0.011204	0.010905	0.010616	0.008820
18	α	mm^2/s	0.70562	1.05301	1.42775	1.82908	5.33390
19	ν	cSt	0.55152	0.59594	0.64905	0.71404	3.61836
20	Pr	[-]	0.78160	0.56594	0.45460	0.39038	0.67837

3.4. Pressure Sensitivity

In the previous results of the current study, the absolute pressure at 30 bar was fixed as a reasonable value for general hythane handling. However, hythane utilization and storage can occur over a range of system pressures below and above this selected value, depending on the scale of the hythane network (being small and local, intermediate and regional, or large and international). To alleviate this concern, five additional absolute pressures were selected, and the hythane properties were computed at these additional pressure values. These pressures span a range from a low atmospheric level (relevant to service lines delivering the gas to buildings) to a high level (relevant to transmission lines moving the gas over a long distance). The absolute pressure values selected here for the sensitivity analysis (including the baseline value of 30 bar) are as follows:

(1) 1 bar (0.987 atm or 14.5 psi);
(2) 10 bar (9.87 atm or 145 psi);
(3) 20 bar (19.74 atm or 290 psi);

(4) 30 bar (29.61 atm or 435 psi);
(5) 40 bar (39.48 bar or 580 psi);
(6) 50 bar (49.35 atm or 725 psi).

It is worth mentioning that standard on-board compressed natural gas (CNG) tanks for vehicles have a standard pressure level of 3600 psi (248 bar) [198], while stationary CNG storage can operate at higher pressures like 5000 psi (345 bar) [199]. These storage-oriented pressures are much higher than those encountered for transportation and are considered outside the primary scope of the current study.

For the sake of this pressure sensitivity analysis, the mid-range hythane composition was selected, with 15% hydrogen and 85% methane (by mole). This is justified by being a representative realistic composition, equally far from the two extreme limiting cases of 0% hydrogen and 30% hydrogen.

A comparison is given in Table 6 for the numerical values of the 20 properties at the six pressure values.

Table 6. Values of the evaluated hythane properties at different absolute pressures for a selected hythane composition of 15% hydrogen and 85% methane (by mole). The temperature is at a baseline level of 20 °C.

Index	Property Symbol	Unit	Absolute Pressure of Mid-Range Hythane (15% H_2) at 20 °C					
			1 Bar	10 Bar	20 Bar	30 Bar (Baseline)	40 Bar	50 Bar
1	MW	kg/kmol	13.9388	13.9388	13.9388	13.9388	13.9388	13.9388
2	R_g	J/(kg·K)	596.499	596.499	596.499	596.499	596.499	596.499
3	Y_{H2}	%	2.1694%	2.1694%	2.1694%	2.1694%	2.1694%	2.1694%
4	Y_{CH4}	%	97.8306%	97.8306%	97.8306%	97.8306%	97.8306%	97.8306%
5	c	m/s	479.758	478.196	476.812	475.843	475.338	475.345
6	ρ	kg/m^3	0.573	5.790	11.721	17.792	23.998	30.330
7	$\overline{v}$	m^3/kg	1.7464634	0.1727143	0.0853134	0.0562041	0.0416707	0.0329701
8	u	kJ/kg	788.537	782.608	775.926	769.149	762.286	755.347
9	h	kJ/kg	963.183	955.322	946.553	937.762	928.969	920.198
10	s	kJ/(kg·K)	7.90576	6.51208	6.07598	5.81130	5.61675	5.46063
11	C_p	J/(kg·K)	2481.67	2530.92	2588.33	2648.49	2711.20	2776.17
12	C_v	J/(kg·K)	1880.70	1888.41	1896.91	1905.32	1913.61	1921.75
13	γ	[-]	1.31955	1.34024	1.36450	1.39005	1.41680	1.44461
14	Z	[-]	0.99876	0.98771	0.97577	0.96425	0.95321	0.94274
15	μ_{JT}	K/MPa	3.511333	3.458619	3.393427	3.320857	3.240622	3.152619
16	λ	W/(m·K)	0.055938	0.056639	0.057445	0.058291	0.059186	0.060136
17	μ	mPa·s (cP)	0.010668	0.010770	0.010902	0.011053	0.011225	0.011417
18	α	mm^2/s	39.36600	3.86515	1.89342	1.23701	0.90968	0.71418
19	ν	mm^2/s (cSt)	18.63062	1.86010	0.93006	0.62124	0.46776	0.37643
20	Pr	[-]	0.47327	0.48125	0.49121	0.50221	0.51420	0.52708

As expected, the four chemical properties (MW, R_g, Y_{H2}, Y_{CH4}) are independent of the pressure.

Eight other properties follow a monotonic decrease in response to the pressure increase. These are $\overline{v}$, u, h, s, Z, μ_{JT}, α, and ν.

Seven other properties follow a monotonic increase in response to the pressure increase. These are ρ, C_p, C_v, γ, λ, μ, and Pr.

The speed of sound (c) has a unique behavior, where it initially decreases with pressure, but then it reverses this downtrend and starts to increase.

The effect of pressure is small or mild except for the density (ρ) and its directly dependent properties ($\overline{v}$, α, and ν), where the variations are large (more than one order of magnitude increase or decrease) due to the high sensitivity of the density to the pressure. These fast-changing variables due to the pressure show the steepest change as the pressure

is raised above the atmospheric value. This observation is consistent with hythane as a compressible gas rather than an incompressible fluid.

3.5. Temperature Sensitivity

In the previous results of the current study, the temperature was fixed at a suitable ambient value of 20 °C or 293.15 K when evaluating the hythane properties. This might be considered a reasonable choice, since this normal ambient temperature is a good representation of outdoor processes involving hythane, such as pipeline transportation and vessel storage, particularly for underground pipelines. However, seasonal variation and hourly variations in the ambient conditions, as well as compression processes, lead to elevated temperatures, especially in hot climates. This suggests performing another sensitivity analysis, but by varying the temperature this time (rather than the pressure).

To this end, the 20 hythane properties were evaluated at five additional temperatures beyond the baseline temperature of 20 °C. These auxiliary temperatures were 30 °C, 40 °C, 50 °C, 60 °C, and 70 °C. Like the pressure sensitivity analysis, the mid-range hythane composition (85% CH_4 and 15% H_2) is retained in the current temperature sensitivity analysis. A baseline absolute pressure of 30 bar is adopted in the current temperature sensitivity analysis.

A comparison is given in Table 7 for the numerical values of the 20 properties at the six temperature values (the five additional values as well as the baseline value).

Table 7. Values of the evaluated hythane properties at different temperatures for a selected hythane composition of 15% hydrogen and 85% methane (by mole). The absolute pressure is at a baseline level of 30 bar.

Index	Property Symbol	Unit	Temperature of Mid-Range Hythane (15% H_2) at 30 Bar (Absolute)					
			20 °C (Baseline)	30 °C	40 °C	50 °C	60 °C	70 °C
1	MW	kg/kmol	13.9388	13.9388	13.9388	13.9388	13.9388	13.9388
2	R_g	J/(kg·K)	596.499	596.499	596.499	596.499	596.499	596.499
3	Y_{H2}	%	2.1694%	2.1694%	2.1694%	2.1694%	2.1694%	2.1694%
4	Y_{CH4}	%	97.8306%	97.8306%	97.8306%	97.8306%	97.8306%	97.8306%
5	c	m/s	475.84	484.37	492.58	500.51	508.18	515.61
6	ρ	kg/m^3	17.792	17.120	16.502	15.930	15.401	14.908
7	ϑ	m^3/kg	0.0562041	0.0584114	0.0606004	0.0627733	0.0649322	0.0670785
8	u	kJ/kg	769.149	789.048	809.099	829.328	849.759	870.414
9	h	kJ/kg	937.762	964.282	990.900	1017.648	1044.556	1071.649
10	s	kJ/(kg·K)	5.81130	5.90026	5.98665	6.07072	6.15273	6.23286
11	C_p	J/(kg·K)	2648.49	2656.32	2667.75	2682.33	2699.66	2719.42
12	C_v	J/(kg·K)	1905.32	1926.22	1948.98	1973.46	1999.51	2026.99
13	γ	[-]	1.39005	1.37904	1.36879	1.35920	1.35016	1.34160
14	Z	[-]	0.96425	0.96906	0.97327	0.97697	0.98024	0.98313
15	μ_{JT}	K/MPa	3.320857	3.091599	2.881171	2.687513	2.508888	2.343816
16	λ	W/(m·K)	0.058291	0.060098	0.061929	0.063784	0.065663	0.067566
17	μ	mPa·s (cP)	0.011053	0.011342	0.011629	0.011912	0.012192	0.012470
18	α	mm^2/s	1.23701	1.32154	1.40678	1.49272	1.57934	1.66662
19	ν	mm^2/s (cSt)	0.62124	0.66253	0.70470	0.74774	0.79166	0.83645
20	Pr	[-]	0.502212	0.501332	0.500930	0.500928	0.501264	0.501884

As expected, the four chemical properties (MW, R_g, Y_{H2}, Y_{CH4}) are independent of the pressure.

Only three properties follow a monotonic decrease in response to the temperature increase. These are ρ, γ, and μ_{JT}.

Twelve other properties follow a monotonic increase in response to the temperature increase. These are c, ϑ, u, h, s, C_p, C_v, Z, λ, μ, α, and ν.

The Prandtl number (Pr) has a unique behavior, where it initially decreases with temperature, but it then reverses this downtrend and starts to increase.

The effect of temperature is small or mild, with the absence of very steep variations as observed in the pressure sensitivity analysis.

3.6. Summary of Regression Models

Table 8 summarizes the regression models proposed in Section 3.2 for all 20 hythane properties at the baseline conditions of 30 bar (absolute) and 20 °C, together with their goodness-of-fit statistics. In each model, x is the hydrogen mole fraction expressed as a decimal fraction (from 0.00 to 0.30), and y is the property in the listed unit. A linear model is used for 18 properties, whereas a quadratic model is used for the adiabatic index (γ) and the Prandtl number (Pr), for which it provides a better fit than the linear model. All models were fitted by ordinary least squares to the 31 computed compositions (from 0% to 30% H_2 with a 1% increment). In addition to the coefficient of determination (R^2), the table reports the adjusted coefficient of determination (adjusted R^2), which accounts for the number of fitted coefficients; the root-mean-square error (RMSE) of the residuals, expressed in the unit of the property; and the maximum absolute relative residual over the 31 compositions. To assess the predictive accuracy independently of the fitting data, each model was also refitted using only the 16 compositions with even hydrogen percentages (0%, 2%, ..., 30%), and its predictions were compared with the computed values at the 15 compositions with odd percentages (1%, 3%, ..., 29%), which were excluded from the refitting. The maximum relative prediction error at these held-out compositions is reported in the last column. For the hydrogen mass fraction (Y_{H2}), which vanishes at 0% H_2, the residual and prediction errors are given as absolute values in percentage points (pp) instead of relative values. The adjusted R^2 is at least 0.9907 for all 20 models, the maximum relative residual is below 3% for all properties (and below 1% for 10 of them), and the maximum held-out prediction error does not exceed 2.04%. This confirms that the proposed models can be used reliably for interpolation within the investigated range of hydrogen content.

Table 8. Summary of the proposed regression models for the 20 hythane properties as functions of the hydrogen mole fraction (x, as a decimal fraction from 0.00 to 0.30) at 30 bar (absolute) and 20 °C, with their goodness-of-fit statistics.

Index	Symbol	Unit	Regression Equation	R^2	Adj. R^2	RMSE	Max. Rel. Error (%)	Max. Test Error (%)
1	Y_{CH4}	[-]	y = 1.002285 − 0.168922 x	0.993459	0.993234	0.001226	0.285	0.211
2	Y_{H2}	[-]	y = −0.00228472 + 0.168922 x	0.993459	0.993234	0.001226	0.271 pp	0.201 pp
3	MW	kg/kmol	y = 16.0428 − 14.0269 x	1.000000	1.000000	≈0	0.000	0.000
4	ρ	kg/m^3	y = 20.8220 − 20.0107 x	0.999802	0.999795	0.02517	0.329	0.252
5	v	m^3/kg	y = 0.0470877 + 0.0640140 x	0.994186	0.993986	0.0004378	1.703	1.326
6	λ	W/(m·K)	y = 0.0356243 + 0.151118 x	1.000000	1.000000	7.349×10^{-7}	0.004	0.003
7	C_v	J/(kg·K)	y = 1708.61 + 1389.88 x	0.992767	0.992517	10.61	1.149	0.897
8	C_p	J/(kg·K)	y = 2389.08 + 1845.49 x	0.991051	0.990742	15.69	1.220	0.952

Table 8. *Cont.*

Index	Symbol	Unit	Regression Equation	R^2	Adj. R^2	RMSE	Max. Rel. Error (%)	Max. Test Error (%)
9	γ	[-]	$y = 1.39922 - 0.0762920\,x + 0.101119\,x^2$	0.999983	0.999982	1.707×10^{-5}	0.003	0.002
10	u	kJ/kg	$y = 721.017 + 337.875\,x$	0.994248	0.994050	2.299	0.615	0.463
11	h	kJ/kg	$y = 862.280 + 529.917\,x$	0.994225	0.994026	3.612	0.776	0.606
12	s	kJ/(kg·K)	$y = 4.76597 + 7.20736\,x$	0.997578	0.997495	0.03176	1.089	0.858
13	μ	mPa·s (cP)	$y = 0.0115056 - 0.00298890\,x$	0.999821	0.999814	3.581×10^{-6}	0.067	0.052
14	Z	[-]	$y = 0.946823 + 0.112779\,x$	0.997971	0.997901	0.0004549	0.098	0.075
15	R_g	J/(kg·K)	$y = 510.028 + 609.167\,x$	0.993459	0.993234	4.421	1.590	1.240
16	c	m/s	$y = 433.874 + 289.885\,x$	0.997252	0.997157	1.361	0.588	0.458
17	ν	mm^2/s (cSt)	$y = 0.544694 + 0.537423\,x$	0.994215	0.994015	0.003667	1.237	0.966
18	Pr	[-]	$y = 0.766807 - 2.32187\,x + 3.66435\,x^2$	0.997607	0.997436	0.005507	2.473	1.407
19	α	mm^2/s	$y = 0.685910 + 3.74590\,x$	0.999174	0.999145	0.009633	2.794	2.036
20	μ_{JT}	K/MPa	$y = 4.30060 - 6.39073\,x$	0.998911	0.998873	0.01888	1.579	1.182

4. Discussion

In the current section, a broader justification for the observed composition dependence of the hythane properties as shown in the preceding sweep figures is provided. This accompanies the earlier property-specific discussion about its variation and the implications of that variation.

This dependence pattern arises from three coupled effects, as listed below:

(1) Replacing methane with hydrogen substantially lowers the molecular weight of the binary hythane gas mixture (drops by 26.2% between 0% H_2 and 30% H_2). Consequently, the specific gas constant increases, while the density decreases at constant pressure and temperature. These are primary composition effects that propagate directly into derived quantities such as the specific volume, speed of sound, momentum diffusivity, and thermal diffusivity.

(2) Hydrogen and methane differ remarkably in their molecular size, mass, collision dynamics, and energy-transfer efficiency. Therefore, hydrogen alters the momentum and heat transport differently. The addition of hydrogen into natural gas strongly increases thermal conductivity (by 127.3% between 0% H_2 and 30% H_2), while the absolute viscosity changes to a much lesser extent (dropping by 7.8% between 0% H_2 and 30% H_2), thereby producing a pronounced change in the balance between thermal and momentum diffusion.

(3) The mixture is not exactly ideal (a perfect gas) at an absolute pressure of 30 bar. Thus, the Helmholtz-energy mixture formulation introduces composition-dependent

residual and binary-interaction contributions. Therefore, departure from simple mole-fraction averaging remains possible. The presented curves earlier should therefore be interpreted differently by distinguishing directly composition-controlled properties (such as the molecular weight), properties derived from coupled thermodynamic variables (such as the speed of sound), and transport properties governed by molecular interactions and mixing rules (such as the absolute viscosity).

From a sustainability perspective, the main environmental benefit of hythane arises at the point of use [200]. Combining the computed hydrogen and methane mass fractions with the LHV values given in Section 3.2.6, and assuming complete combustion, the direct carbon dioxide emissions per unit of released energy (LHV basis) decrease from 54.83 g/MJ for methane to 53.06 g/MJ (a 3.2% reduction) at 10% H_2, 52.06 g/MJ (a 5.1% reduction) at 15% H_2, and 48.56 g/MJ (an 11.4% reduction) at 30% H_2. These reductions are considerably smaller than the hydrogen mole fraction itself, because hydrogen has a much lower volumetric heating value than methane. Moreover, they represent combustion emissions only. The life-cycle benefit depends on the hydrogen production pathway. Hydrogen produced by water electrolysis powered by renewable electricity (green hydrogen) [201,202] has low life-cycle emissions. Hydrogen produced by steam methane reforming with carbon capture and storage (blue hydrogen) offers an intermediate benefit that depends on the capture rate and on upstream methane leakage. In contrast, hydrogen produced by steam methane reforming without carbon capture (grey hydrogen) provides little or no net reduction, because carbon dioxide is released during its production. Therefore, the description of hythane as a more sustainable alternative to natural gas in the current study refers to its reduced carbon content and combustion emissions, which translate into life-cycle emission reductions only when low-carbon hydrogen is used. A complete life-cycle assessment is beyond the scope of the present property-based study.

5. Conclusions

The current study presents a computational investigation of how 20 properties of compressed hythane (methane-dominated hydrogen-enriched methane) vary as the hydrogen mole fraction incrementally increases from 0% (pure methane) to 30% (practical upper limit of hydrogen enrichment for hythane) at an ambient temperature of 20 °C and a typical pipeline absolute pressure of 30 bar. Using the validated CoolProp package in Python, these 20 properties were evaluated systematically and visualized through consistent plots and compact regression models to reveal insights into the composition-dependent behavior of hythane. The results of this work provide a framework for understanding which properties (chemical, thermofluidic, or transport) are weakly sensitive to hydrogen addition, which are strongly correlated with hydrogen enrichment even with moderate hydrogen enrichment, and which exhibit a nonlinear response to this blending. The variation of the 20 hythane properties with absolute pressure (between 1 bar and 50 bar) and with temperature (between 20 °C and 70 °C) at a moderate hydrogen enrichment level of 15% by mole was also examined.

The following statements can be made:

- CoolProp was found to be accurate as a calculator of fluid properties compared to the Chemistry WebBook (Standard Reference Database Number 69 or SRD 69) of the NIST (United States National Institute of Standards and Technology) for pure methane and pure hydrogen. Compared to the Cantera thermochemical calculator for a mixture of 85% CH_4 and 15% H_2, the deviations were within 2.7% for most properties. The larger deviations in density (3.64%) and specific heat capacity at constant pressure (6.77%) reflect the ideal-gas treatment in Cantera, and the largest deviation (18.14%) in the thermal conductivity reflects differences between the mixture-transport models.

- Hydrogen enrichment in hythane has very different effects on various properties of hythane. The intensity of these effects varies from being negligible (such as the adiabatic index) to being steep (such as the thermal diffusivity).
- Compared to methane, hythane has larger values for the following properties: (1) specific gas constant, (2) hydrogen mass fraction, (3) speed of sound, (4) specific volume, (5) specific internal energy, (6) specific enthalpy, (7) specific entropy, (8) specific heat capacity at constant pressure, (9) specific heat capacity at constant volume, (10) thermal conductivity, (11) momentum diffusivity, (12) thermal diffusivity, and (13) compressibility factor.
- Compared to methane, hythane has lower values for the following properties: (1) molecular weight, (2) methane mass fraction, (3) Prandtl number, (4) density, (5) Joule–Thomson coefficient, (6) absolute viscosity, and (7) adiabatic index.
- Hythane can be approximated as having a composition-independent adiabatic index, with a value of 1.3923.
- At the selected conditions pertaining to natural gas pipelines, the properties of hythane over its range of possible compositions can be approximated well through a simple linear regression model in most cases. A quadratic regression model is suggested instead of the linear one for the adiabatic index and the Prandtl number, in order to maintain the coefficient of determination above 0.99.
- The computed changes in density and thermal conductivity suggest that using methane (natural gas) pipelines for transporting hythane may require some retrofits, which should be confirmed through dedicated pipeline-hydraulic and thermal analyses. This is in addition to the hydrogen embrittlement interaction with the pipeline walls.
- Hydrogen enrichment raises the gravimetric heating value of hythane but lowers its volumetric energy density at pipeline conditions (by 12.2% at 15% H_2 and 23.7% at 30% H_2), while it reduces the direct carbon dioxide emissions per unit of released energy (by 5.1% and 11.4%, respectively). The life-cycle environmental benefit depends on the use of low-carbon hydrogen.
- The effect of pressure on hythane properties varied; four properties were unchanged, eight properties featured a monotonic decrease, seven properties featured a monotonic increase, and one property featured a minimum point.
- The effect of temperature on hythane properties varied; four properties were unchanged, three properties featured a monotonic decrease, twelve properties featured a monotonic increase, and one property featured a minimum point.
- The current results are limited to a binary methane–hydrogen mixture, a single baseline condition (30 bar and 20 °C) with sensitivity analyses at 15% H_2, and model-based mixture transport properties (particularly the thermal conductivity), and they lack direct experimental validation for hythane. The engineering implications discussed here are qualitative inferences that require dedicated pipeline, compressor, and materials analyses.

Funding: This research received no external funding.

Institutional Review Board Statement: Not applicable.

Informed Consent Statement: Not applicable.

Data Availability Statement: Data are contained within the article.

Conflicts of Interest: The author declares no competing financial interests or personal relationships that could have appeared to influence the work reported in this paper.

References

1. Global Gas Infrastructure Tracker (GGIT). Asset-Level Data on Gas Transmission Pipeline Projects and Liquefied Natural Gas Import and Export Terminals. Available online: https://globalenergymonitor.org/projects/global-gas-infrastructure-tracker (accessed on 31 May 2026).
2. Research and Markets Ltd. (R&M). Oil and Gas Pipelines Industry Outlook by Capacity and Capital Expenditure Including Details of All Operating and Planned Pipelines to 2027. Available online: https://www.researchandmarkets.com/reports/5912961/oil-gas-pipelines-industry-outlook-capacity (accessed on 31 May 2026).
3. Statista Countries with Longest Operational Natural Gas Pipeline Networks Worldwide in 2024 (in Kilometers). Available online: https://www.statista.com/statistics/459552/length-of-natural-gas-pipelines-by-country/ (accessed on 31 May 2026).
4. Snam Natural Gas Atlas. Available online: https://www.snamatlas.it/world_of_gas#focus-container (accessed on 31 May 2026).
5. Marzouk, O.A. Radiant Heat Transfer in Nitrogen-Free Combustion Environments. *Int. J. Nonlinear Sci. Numer. Simul.* **2018**, *19*, 175–188. [CrossRef]
6. Marzouk, O.A. Detailed and Simplified Plasma Models in Combined-Cycle Magnetohydrodynamic Power Systems. *Int. J. Adv. Appl. Sci.* **2023**, *10*, 96–108. [CrossRef]
7. Marzouk, O.A. Temperature-Dependent Functions of the Electron–Neutral Momentum Transfer Collision Cross Sections of Selected Combustion Plasma Species. *Appl. Sci.* **2023**, *13*, 11282. [CrossRef]
8. Marzouk, O.A. Hydrogen Utilization as a Plasma Source for Magnetohydrodynamic Direct Power Extraction (MHD-DPE). *IEEE Access* **2024**, *12*, 167088–167107. [CrossRef]
9. Plaksin, V.Y.; Kirillov, I.A. Hydrogen Flammability and Explosion Concentration Limits for a Wide Temperature Range. *J. Loss Prev. Process Ind.* **2025**, *94*, 105554. [CrossRef]
10. Crowl, D.A.; Jo, Y.-D. The Hazards and Risks of Hydrogen. *J. Loss Prev. Process Ind.* **2007**, *20*, 158–164. [CrossRef]
11. Armaroli, N.; Balzani, V. The Hydrogen Issue. *ChemSusChem* **2011**, *4*, 21–36. [CrossRef] [PubMed]
12. Kvenvolden, K.A. A Review of the Geochemistry of Methane in Natural Gas Hydrate. *Org. Geochem.* **1995**, *23*, 997–1008. [CrossRef]
13. Hureau, G.; Lecarpentier, A.; Serbutoviez, S.; Kaniewicz, J.; Madden, M.; Brooks, C.; Robertson, A.; Harrison, C.; Langston, C.; Ravalec, M.L. Global Methane Emissions from Natural Gas Transmission and Distribution Networks. *Sci. Tech. Energ. Transit.* **2025**, *80*, 28. [CrossRef]
14. Minic, D. *Hydrogen Energy: Challenges and Perspectives*; IntechOpen: Rijeka, Croatia, 2012; ISBN 978-953-51-0812-2.
15. Lynch, F.E.; Marmaro, R.W. Special Purpose Blends of Hydrogen and Natural Gas. U.S. Patent US5139002A, 18 August 1992. Available online: https://patents.google.com/patent/US5139002A/en (accessed on 18 September 2026).
16. Pandey, V.; Guluwadi, S.; Tafesse, G.H. Performance and Emission Study of Low HCNG Fuel Blend in SI Engine with Fixed Ignition Timing. *Cogent Eng.* **2022**, *9*, 2010925. [CrossRef]
17. Krishna, S.; Mahant, B.; Robustillo, M.D.; Sreenivasan, H.; Pandey, J.S. The Role of Gas Hydrates in Storing Natural Gas-Hydrogen Blends for Coupling Power-to-X and Decarbonization. *Energy Fuels* **2024**, *38*, 23192–23229. [CrossRef]
18. Li, J.; Su, Y.; Yu, B.; Wang, P.; Sun, D. Influences of Hydrogen Blending on the Joule–Thomson Coefficient of Natural Gas. *ACS Omega* **2021**, *6*, 16722–16735. [CrossRef] [PubMed]
19. Sagar, S.M.V.; Agarwal, A.K. Hydrogen-Enriched Compressed Natural Gas: An Alternate Fuel for IC Engines. In *Advances in Internal Combustion Engine Research*; Srivastava, D.K., Agarwal, A.K., Datta, A., Maurya, R.K., Eds.; Springer: Singapore, 2018; pp. 111–134, ISBN 978-981-10-7575-9.
20. Annesini, M.C. *Production and Purification of Hydrogen-Methane Mixtures Utilized in Internal Combustion Engines*; Augelletti, R., De Falco, M., Frattari, S., Gironi, F., Murmura, M.A., Eds.; WIT Press: Istanbul, Turkey, 2015; pp. 535–545.
21. Villante, C.; Genovese, A. Hydromethane: A Bridge towards the Hydrogen Economy or an Unsustainable Promise? *Int. J. Hydrogen Energy* **2012**, *37*, 11541–11548. [CrossRef]
22. Marzouk, O.A. Performance Analysis of Shell-and-Tube Dehydrogenation Module. *Int. J. Energy Res.* **2017**, *41*, 604–610. [CrossRef]
23. Marzouk, O.A. Technical Review of Radiative-Property Modeling Approaches for Gray and Nongray Radiation, and a Recommended Optimized WSGGM for CO_2/H_2O-Enriched Gases. *Results Eng.* **2025**, *25*, 103923. [CrossRef]
24. Hora, C.; Dan, F.C.; Secui, D.-C.; Hora, H.N. Systematic Literature Review on Pipeline Transport Losses of Hydrogen, Methane, and Their Mixture, Hythane. *Energies* **2024**, *17*, 4709. [CrossRef]
25. Wang, W.; Wang, Q.; Deng, H.; Cheng, G.; Li, Y. Feasibility analysis on the transportation of hydrogen–natural gas mixtures in natural gas pipelines. *Nat. Gas Ind.* **2020**, *40*. [CrossRef]
26. Mahajan, D.; Tan, K.; Venkatesh, T.; Kileti, P.; Clayton, C.R. Hydrogen Blending in Gas Pipeline Networks—A Review. *Energies* **2022**, *15*, 3582. [CrossRef]
27. Marzouk, O.A. Tilt Sensitivity for a Scalable One-Hectare Photovoltaic Power Plant Composed of Parallel Racks in Muscat. *Cogent Eng.* **2022**, *9*, 2029243. [CrossRef]

28. Marzouk, O.A. Wind Speed Weibull Model Identification in Oman, and Computed Normalized Annual Energy Production (NAEP) from Wind Turbines Based on Data from Weather Stations. *Eng. Rep.* **2025**, *7*, e70089. [CrossRef]
29. Marzouk, O.A. Levelized Cost of Green Hydrogen (LCOH) in the Sultanate of Oman Using H2A-Lite with Polymer Electrolyte Membrane (PEM) Electrolyzers Powered by Solar Photovoltaic (PV) Electricity. *E3S Web Conf.* **2023**, *469*, 00101. [CrossRef]
30. Srivastava, D.; Arya, A.K. Hydrogen Injection in Natural Gas Pipeline Networks. In *Proceedings of the Recent Advances in Energy Transitions Towards Sustainable Development*; Ghosh, A., Sapkal, V., Kamachi Mudali, U., Eds.; Springer Nature: Singapore, 2025; pp. 115–128.
31. French Agency for Environment and Energy Management (ADEME). GDF Suez, McPhy in French GRHYD Project on Methane, Hydrogen. *Fuel Cells Bull.* **2012**, *2012*, 10. [CrossRef]
32. Leicher, J.; Schaffert, J.; Carpentier, S.; Albus, R.; Görner, K. *THyGA [Testing Hydrogen Admixture for Gas Applications]/Impact of Hydrogen Admixture on Combustion Processes—Part I: Theory*; Hydrogen Knowledge Centre: Paris, France, 2020; pp. 1–30.
33. Ko, S.; Qiao, Y.; Nickerson, E.; Shin, Y.; Han, K.S.; Kuang, W.; Simmons, K. Investigating In-Situ Fracture Behaviors of Polymer Pipeline Materials in Hydrogen and Hydrogen-Methane Blended Gas Environments. In *Pressure Vessels and Piping Conference*; American Society of Mechanical Engineers Digital Collection; American Society of Mechanical Engineers: New York, NY, USA, 2024.
34. Marzouk, O.A. Portrait of the Decarbonization and Renewables Penetration in Oman's Energy Mix, Motivated by Oman's National Green Hydrogen Plan. *Energies* **2024**, *17*, 4769. [CrossRef]
35. Leicher, J.; Schaffert, J.; Cigarida, H.; Tali, E.; Burmeister, F.; Giese, A.; Albus, R.; Görner, K.; Carpentier, S.; Milin, P.; et al. The Impact of Hydrogen Admixture into Natural Gas on Residential and Commercial Gas Appliances. *Energies* **2022**, *15*, 777. [CrossRef]
36. Pourhoseini, S.H. A Novel Configuration of Natural Gas Diffusion Burners to Enhance Optical, Thermal and Radiative Characteristics of Flame and Reduce NO_x Emission. *Energy* **2017**, *132*, 41–48. [CrossRef]
37. Dupont, V.; Pourkashanian, M.; Williams, A.; Woolley, R. The Reduction of NO_x Formation in Natural Gas Burner Flames. *Fuel* **1993**, *72*, 497–503. [CrossRef]
38. McReynolds, D.H.; Ding, G.; Gagné-Bourque, C.; Kang, M. Effects of Hydrogen Blending on Methane Emissions in Natural Gas Distribution and End-Use Piping. *Environ. Res. Infrastruct. Sustain.* **2026**, *6*, 011001. [CrossRef]
39. Di Lullo, G.; Oni, A.O.; Kumar, A. Blending Blue Hydrogen with Natural Gas for Direct Consumption: Examining the Effect of Hydrogen Concentration on Transportation and Well-to-Combustion Greenhouse Gas Emissions. *Int. J. Hydrogen Energy* **2021**, *46*, 19202–19216. [CrossRef]
40. Marzouk, O.A. Estimated Electric Conductivities of Thermal Plasma for Air-Fuel Combustion and Oxy-Fuel Combustion with Potassium or Cesium Seeding. *Heliyon* **2024**, *10*, e31697. [CrossRef] [PubMed]
41. Marzouk, O.A. Multi-Scale Computational Fluid Dynamics (CFD) and Reduced-Order Modeling (ROM) of Metal Membrane Modules for Blue Hydrogen Production and Carbon Capture, Utilization, and Storage (CCUS). *Processes* **2026**, *14*, 3725. [CrossRef]
42. Truslove, S.; Bruce, E.L.; Yiu, H.H.P. An Appraisal on Various Hydrogen Productions and Their CO_2 Emissions—A Comparison on the Grey, Blue and Green Pathways. *J. Chem. Technol. Biotechnol.* **2025**, *100*, 1753–1761. [CrossRef]
43. Ammar, M.; Oyewale, B.O.; Elseragy, A.; Albayati, I.M.; Aliyu, A.M. A Global Review of Blue and Green Hydrogen Fuel Production Technologies, Trends and Future Outlook to 2050. *Fuels* **2025**, *6*, 88. [CrossRef]
44. Makaryan, I.A.; Sedov, I.V.; Salgansky, E.A.; Arutyunov, A.V.; Arutyunov, V.S. A Comprehensive Review on the Prospects of Using Hydrogen–Methane Blends: Challenges and Opportunities. *Energies* **2022**, *15*, 2265. [CrossRef]
45. Marzouk, O.A. Aerial E-Mobility Perspective: Anticipated Designs and Operational Capabilities of eVTOL Urban Air Mobility (UAM) Aircraft. *Edelweiss Appl. Sci. Technol.* **2025**, *9*, 413–442. [CrossRef]
46. Marzouk, O.A. Chamber Pressure as a Decision-Making Design Metric in Bi-Propellant Rocket Systems (and Overview of an Omani-Argentinian Collaborative Program in Space Applications). *Comput. Decis. Mak. Int. J.* **2026**, *3*, 3023–3041. [CrossRef]
47. Dally, B.B.; Masri, A.R.; Barlow, R.S.; Fiechtner, G.J. Instantaneous and Mean Compositional Structure of Bluff-Body Stabilized Nonpremixed Flames. *Combust. Flame* **1998**, *114*, 119–148. [CrossRef]
48. Marzouk, O.A. Verification of the reactingFoam Solver Through Simulating Hydrogen–Methane Turbulent Diffusion Flame, and an Overview of Flame Types and Flame Stabilization Techniques. *Processes* **2025**, *13*, 3610. [CrossRef]
49. Pallav; Gajbhiye, K.R.; Bist, N.; Sircar, A. Experimental Investigation of Flame and Emission Characteristics of Hydrogen-Enriched Natural Gas Mixtures—An Innovative Approach for India's City Gas Distribution Network. *ACS Omega* **2026**, *11*, 35218–35233. [CrossRef] [PubMed]
50. Marzouk, O.A. Direct Numerical Simulations of the Flow Past a Cylinder Moving with Sinusoidal and Nonsinusoidal Profiles. *J. Fluids Eng.* **2009**, *131*, 121201. [CrossRef]
51. Marzouk, O.A. The Sod Gasdynamics Problem as a Tool for Benchmarking Face Flux Construction in the Finite Volume Method. *Sci. Afr.* **2020**, *10*, e00573. [CrossRef]

52. Wang, L.; Wang, K.; Zhao, G.; Wang, Y.; Li, Z.; Tong, F.; Lei, L.; Xu, Z. Ultraselective Carbon Hollow Fiber Membrane for H_2 Extraction from Blended Natural Gas. *Chem. Eng. Sci.* **2025**, *302*, 120717. [CrossRef]
53. Ficco, G.; Cassano, M.; Cortellessa, G.; Zuena, F.; Dell'Isola, M. On the Reliability of Temperature Measurements in Natural Gas Pipelines. *Sensors* **2023**, *23*, 3121. [CrossRef] [PubMed]
54. Ramadhas, A.S.; Singh, P.K.; Mathai, R.; Sehgal, A.K. Impact of Ambient Temperature Conditions on Cold Start Combustion, Gaseous and Particle Emissions from Gasoline Engines. In Proceedings of the International Powertrains, Fuels & Lubricants Meeting, Beijing, China, 8 October 2017; p. 2017-01-2286. [CrossRef]
55. Bell, I.H.; Wronski, J.; Quoilin, S.; Lemort, V. Pure and Pseudo-Pure Fluid Thermophysical Property Evaluation and the Open-Source Thermophysical Property Library CoolProp. *Ind. Eng. Chem. Res.* **2014**, *53*, 2498–2508. [CrossRef] [PubMed]
56. CoolProp. Welcome to CoolProp. Available online: https://coolprop.org (accessed on 1 June 2026).
57. CoolProp. Citation for CoolProp. Available online: https://coolprop.org/citation.html (accessed on 1 June 2026).
58. Nagpal, A.; Gabrani, G. Python for Data Analytics, Scientific and Technical Applications. In Proceedings of the 2019 Amity International Conference on Artificial Intelligence (AICAI), Dubai, United Arab Emirates, 4–6 February 2019; pp. 140–145.
59. Mattsson, S.E.; Elmqvist, H.; Otter, M. Physical System Modeling with Modelica. *Control Eng. Pract.* **1998**, *6*, 501–510. [CrossRef]
60. Marzouk, O.A. Evolutionary Computing Applied to Design Optimization. In *Proceedings of the ASME 2007 International Design Engineering Technical Conferences and Computers and Information in Engineering Conference (IDETC-CIE 2007), 4–7 September 2007*; American Society of Mechanical Engineers (ASME): Las Vegas, NV, USA, 2009; Volume 2, pp. 995–1003. [CrossRef]
61. Nagar, S. Introduction to Octave. In *Introduction to Octave: For Engineers and Scientists*; Nagar, S., Ed.; Apress: Berkeley, CA, USA, 2018; pp. 1–16, ISBN 978-1-4842-3201-9.
62. Domnisoru, C. Using MATHCAD in Teaching Power Engineering. *IEEE Trans. Educ.* **2005**, *48*, 157–161. [CrossRef]
63. Khouya, A. Performance Assessment of a Dual Loop Organic Rankine Cycle Powered by a Parabolic Trough Collector for Ammonia and Hydrogen Production Purpose. *Int. J. Ambient Energy* **2021**, *43*, 6149–6166. [CrossRef]
64. Bell, I. Welcome to ACHP's Documentation!—ACHP 1.4 Documentation. Available online: https://achp.sourceforge.net/ (accessed on 1 June 2026).
65. Predolin, R.E.; Ito, M.C.; Palma, G.L.; Scalon, V.L. An Experimental and Numerical Investigation of Absorber Positioning in a Natural Convection Solar Drying System. *Sol. Energy* **2022**, *243*, 431–442. [CrossRef]
66. SourceForge. DWSIM—Open Source Process Simulator. Available online: https://sourceforge.net/projects/dwsim/ (accessed on 1 June 2026).
67. PyPI. CoolProp: Open-Source Thermodynamic and Transport Properties Database. 2025. Available online: https://coolprop.sourceforge.net/ (accessed on 1 June 2026).
68. CoolProp. Pure and Pseudo-Pure Fluid Properties. Available online: https://coolprop.org/fluid_properties/PurePseudoPure.html (accessed on 1 June 2026).
69. Akasaka, R. A Reliable and Useful Method to Determine the Saturation State from Helmholtz Energy Equations of State. *J. Therm. Sci. Technol.* **2008**, *3*, 442–451. [CrossRef]
70. Akasaka, R. Recent Trends in the Development of Helmholtz Energy Equations of State and Their Application to 3,3,3-Trifluoroprop-1-Ene (R-1243zf). *Sci. Technol. Built Environ.* **2016**, *22*, 1136–1144. [CrossRef]
71. Gao, K.; Wu, J.; Zhang, P.; Lemmon, E.W. A Helmholtz Energy Equation of State for Sulfur Dioxide. *J. Chem. Eng. Data* **2016**, *61*, 2859–2872. [CrossRef]
72. Akasaka, R.; Lemmon, E.W. A Helmholtz Energy Equation of State for 3,3,3-Trifluoroprop-1-Ene (R-1243zf). *Int. J. Thermophys.* **2025**, *46*, 23. [CrossRef]
73. Akasaka, R.; Lemmon, E.W. A Helmholtz Energy Equation of State for Calculations of Thermodynamic Properties of Trans-1,2-Difluoroethene [R-1132(E)]. *Int. J. Thermophys.* **2024**, *45*, 174. [CrossRef]
74. Velliadou, D.; Antoniadis, K.D.; Assael, M.J.; Huber, M.L. Reference Correlation for the Viscosity of Difluoromethane (R-32) from the Triple Point to 425 K and up to 70 MPa. *Int. J. Thermophys.* **2022**, *43*, 129. [CrossRef]
75. Kou, J.; Chen, H.; Luo, S.; Wang, X. A Structure-Preserving Numerical Scheme for Non-Isothermal Compressible Flow in Porous Media: Energy Conservation and Entropy Stability. *Phys. Fluids* **2025**, *37*, 056120. [CrossRef]
76. Rehner, P.; Bauer, G.; Gross, J. FeOs: An Open-Source Framework for Equations of State and Classical Density Functional Theory. *Ind. Eng. Chem. Res.* **2023**, *62*, 5347–5357. [CrossRef]
77. Thorade, M.; Saadat, A. Partial Derivatives of Thermodynamic State Properties for Dynamic Simulation. *Environ. Earth Sci.* **2013**, *70*, 3497–3503. [CrossRef]
78. Kunz, O.; Wagner, W. The GERG-2008 Wide-Range Equation of State for Natural Gases and Other Mixtures: An Expansion of GERG-2004. *J. Chem. Eng. Data* **2012**, *57*, 3032–3091. [CrossRef]
79. Lemmon, E.W.; Jacobsen, R.T. Equations of State for Mixtures of R-32, R-125, R-134a, R-143a, and R-152a. *J. Phys. Chem. Ref. Data* **2004**, *33*, 593–620. [CrossRef]

80. Lemmon, E.W.; Jacobsen, R.T. A Generalized Model for the Thermodynamic Properties of Mixtures. *Int. J. Thermophys.* **1999**, *20*, 825–835. [CrossRef]
81. Lemmon, E.W.; Jacobsen, R.T.; Penoncello, S.G.; Friend, D.G. Thermodynamic Properties of Air and Mixtures of Nitrogen, Argon, and Oxygen From 60 to 2000 K at Pressures to 2000 MPa. *J. Phys. Chem. Ref. Data* **2000**, *29*, 331–385. [CrossRef]
82. CoolProp. Mixtures. Available online: https://coolprop.org/fluid_properties/Mixtures.html (accessed on 1 June 2026).
83. Zhang, B.-J.; Liang, S.; Lu, Y. Calculating Thermodynamic Properties from Perturbation Theory: II. An Analytic Representation for the Square-Well Chain Fluid. *Fluid Phase Equilibria* **2001**, *180*, 183–194. [CrossRef]
84. Lakkas, A.T.; Sgouros, A.P.; Theodorou, D.N. Self-Consistent Field Theory Coupled with Square Gradient Theory of Free Surfaces of Molten Polymers and Compared to Atomistic Simulations and Experiment. *Macromolecules* **2019**, *52*, 5337–5356. [CrossRef]
85. Liang, S.; Zhang, B.; Han, S.; Hu, W.; Jin, Z. Calculating Thermodynamic Properties from Perturbation Theory: Part III. The Mixtures of Square-Well Chain Fluid. *Fluid Phase Equilibria* **2002**, *200*, 337–348. [CrossRef]
86. Mickoleit, E.; Jäger, A.; Breitkopf, C. Carrier-Fluid Screening for a Three-Phase Sublimation Refrigeration Cycle with CO_2 Using Reference Equations of State and COSMO-SAC. *J. Chem. Eng. Data* **2020**, *65*, 1124–1134. [CrossRef]
87. Jäger, A.; Breitkopf, C.; Richter, M. The Representation of Cross Second Virial Coefficients by Multifluid Mixture Models and Other Equations of State. *Ind. Eng. Chem. Res.* **2021**, *60*, 9286–9295. [CrossRef]
88. Song, B.; Xu, D. Speed of the Downstream Turbulent Front in Pipe Flow. In *Proceedings of the IUTAM Symposium on Turbulent/Non-Turbulent Interface in Turbulent Shear Flows*; Wang, J., Marusic, I., Eds.; IUTAM Bookseries; Springer Nature: Cham, Switzerland, 2025; Volume 45, pp. 164–173, ISBN 978-3-031-78150-6.
89. Yang, Y.; Shan, M.; Kan, X.; Duan, K.; Han, Q.; Juan, Y. Thermodynamic Effects of Gas Adiabatic Index on Cavitation Bubble Collapse. *Heliyon* **2023**, *9*, e20532. [CrossRef] [PubMed]
90. Coker, A.K. Compression Equipment (Including Fans). In *Ludwig's Applied Process Design for Chemical and Petrochemical Plants*; Elsevier: Amsterdam, The Netherlands, 2015; pp. 729–978, ISBN 978-0-7506-8524-5.
91. Gordon, S.; McBride, B.J. *Computer Program for Calculation of Complex Chemical Equilibrium Compositions and Applications. Part 1: Analysis*; Glenn Research Center (GRC)—United States National Aeronautics and Space Administration (NASA): Cleveland, OH, USA, 1994; pp. 1–58.
92. Nayfeh, A.H.; Marzouk, O.A.; Arafat, H.N.; Akhtar, I. Modeling the Transient and Steady-State Flow Over a Stationary Cylinder. In *Proceedings of the Volume 1: 20th Biennial Conference on Mechanical Vibration and Noise, Parts A, B, and C*; ASMEDC: Long Beach, CA, USA, 2005; pp. 1513–1523. [CrossRef]
93. Marić, I.; Galović, A.; Šmuc, T. Calculation of Natural Gas Isentropic Exponent. *Flow Meas. Instrum.* **2005**, *16*, 13–20. [CrossRef]
94. Song, Z.-M.; Chen, D.; Ke, Z.-S.; Wang, R.-H.; Wang, Q.-M.; Lu, F.; Qu, J. A New Approach for Active Removal of 5,000 Centistokes Silicone Oil Through 23-Gauge Cannula. *Retina* **2010**, *30*, 1302–1307. [CrossRef] [PubMed]
95. Pattillo, P.D. Design Loads. In *Elements of Oil and Gas Well Tubular Design*; Elsevier: Amsterdam, The Netherlands, 2018; pp. 337–394, ISBN 978-0-12-811769-9.
96. Sundén, B. Electrochemistry and Thermodynamics. In *Hydrogen, Batteries and Fuel Cells*; Elsevier: Amsterdam, The Netherlands, 2019; pp. 15–36, ISBN 978-0-12-816950-6.
97. Verzicco, R.; Camussi, R. Prandtl Number Effects in Convective Turbulence. *J. Fluid Mech.* **1999**, *383*, 55–73. [CrossRef]
98. Hansen, C.F. Note on the Prandtl Number for Dissociated Air. *J. Aeronaut. Sci.* **1953**, *20*, 789–790. [CrossRef]
99. Ahlers, G.; Bodenschatz, E.; Funfschilling, D.; Hogg, J. Turbulent Rayleigh–Bénard Convection for a Prandtl Number of 0.67. *J. Fluid Mech.* **2009**, *641*, 157–167. [CrossRef]
100. Schobert, B.N.; Peeters, A.G.; Rath, F. The Impact of Accretion Heating and Thermal Conduction on the Dead Zone of Protoplanetary Disks. *Astrophys. J.* **2019**, *881*, 56. [CrossRef]
101. Patience, G.S. Physicochemical Analysis. In *Experimental Methods and Instrumentation for Chemical Engineers*; Elsevier: Amsterdam, The Netherlands, 2013; pp. 227–263, ISBN 978-0-444-53804-8.
102. The Engineering ToolBox (TET). Methane—Prandtl Number vs. Temperature. Available online: https://www.engineeringtoolbox.com/methane-prandtl-number-viscosity-heat-capacity-thermal-conductivity-d_2022.html (accessed on 1 June 2026).
103. Mokhatab, S.; Poe, W.A.; Mak, J.Y. Natural Gas Fundamentals. In *Handbook of Natural Gas Transmission and Processing*; Elsevier: Amsterdam, The Netherlands, 2019; pp. 1–35, ISBN 978-0-12-815817-3.
104. Gutow, J. Chemistry LibreTexts | 1.4: Joule-Thompson Coefficient. Available online: https://chem.libretexts.org/Courses/University_of_Wisconsin_Oshkosh/Chem_371%3A_P-Chem_2_to_Folow_Combined_Biophysical_and_P-Chem_1_(Gutow)/01%3A_Thermodynamics/1.04%3A_Joule-Thompson_Coefficient (accessed on 1 June 2026).
105. Zhou, M.-Y.; Fang, Y.; Wang, Q.-H.; Dai, Y.-M.; Liu, Z.-H.; Li, J.-Q.; Kwon, J.-T. Modeling and Validation of High-Pressure Hydrogen Joule-Thomson Effect for Enhanced Hydrogen Energy System Safety. *Energies* **2025**, *18*, 4573. [CrossRef]
106. Li, J.-Q.; Chen, Y.; Ma, Y.B.; Kwon, J.-T.; Xu, H.; Li, J.-C. A Study on the Joule-Thomson Effect of during Filling Hydrogen in High Pressure Tank. *Case Stud. Therm. Eng.* **2023**, *41*, 102678. [CrossRef]

107. Balmer, R.T. Vapor and Gas Refrigeration Cycles. In *Modern Engineering Thermodynamics*; Elsevier: Amsterdam, The Netherlands, 2011; pp. 535–590, ISBN 978-0-12-374996-3.
108. Demirel, Y. Internal Energy and Enthalpy. In *Energy*; Green Energy and Technology; Springer: London, UK, 2012; pp. 99–145, ISBN 978-1-4471-2371-2.
109. United States National Institute of Standards and Technology (NIST). NIST Chemistry WebBook Citation Information. Available online: https://webbook.nist.gov/cgi/cbook.cgi?Contrib=LBHM (accessed on 1 June 2026).
110. Linstrom, P. NIST Chemistry WebBook, NIST Standard Reference Database 69. 1997. Available online: https://webbook.nist.gov/chemistry/ (accessed on 1 June 2026).
111. Linstrom, P.J.; Mallard, W.G. The NIST Chemistry WebBook: A Chemical Data Resource on the Internet. *J. Chem. Eng. Data* **2001**, *46*, 1059–1063. [CrossRef]
112. Rombot, D.; Mokosuli, Y. Potential Ectoparasiticide for Dog and Cat Fleas, a Combination of Ficus Minahassae Extract and Latex from *Carica papaya* L. *J. Adv. Vet. Anim. Res.* **2024**, *11*, 810. [CrossRef] [PubMed]
113. Borland, L.; Brickhouse, M.; Thomas, T.; Fountain, A.W. Review of Chemical Signature Databases. *Anal. Bioanal. Chem.* **2010**, *397*, 1019–1028. [CrossRef] [PubMed]
114. United States National Institute of Standards and Technology (NIST). Data and NIST Chemistry WebBook—Methane. Available online: https://webbook.nist.gov/cgi/cbook.cgi?ID=C74828 (accessed on 1 June 2026).
115. United States National Institute of Standards and Technology (NIST). NIST Chemistry WebBook—Hydrogen. Available online: https://webbook.nist.gov/cgi/cbook.cgi?Name=h2&Units=SI (accessed on 7 May 2022).
116. Cantera. Citing Cantera. Available online: https://cantera.org/citations.html (accessed on 19 July 2026).
117. Goodwin, D.G.; Moffat, H.K.; Schoegl, I.; Speth, R.L.; Weber, B.W. Cantera: An Object-Oriented Software Toolkit for Chemical Kinetics, Thermodynamics, and Transport Processes. 2025. Available online: https://zenodo.org/records/14455267 (accessed on 19 July 2026).
118. Lielmezs, J.; Mak, P.C.N. Thermodynamic Properties of Unsaturated Vapour and Liquid States from a Cubic Equation of State: Saturated and Subcritical Regions. *Thermochim. Acta* **1992**, *196*, 415–435. [CrossRef]
119. Lemmon, E.W.; Span, R. Short Fundamental Equations of State for 20 Industrial Fluids. *J. Chem. Eng. Data* **2006**, *51*, 785–850. [CrossRef]
120. Green, M.A.; Manikowski, A.; Noland, G.; Golden, R.L. A Fuel Cell Power Supply for Long Duration Balloon Flights Using Stored Cryogens. In *Advances in Cryogenic Engineering*; Kittel, P., Ed.; Springer: Boston, MA, USA, 1998; pp. 1265–1271, ISBN 978-1-4757-9047-4.
121. Bell, I.H. Entropy Scaling of Viscosity—II: Predictive Scheme for Normal Alkanes. *J. Chem. Eng. Data* **2020**, *65*, 5606–5616. [CrossRef] [PubMed]
122. Naghizadeh, A.; Amiri-Ramsheh, B.; Atashrouz, S.; Abuswer, M.A.; Abedi, A.; Mohaddespour, A.; Hemmati-Sarapardeh, A. Modeling Thermal Conductivity of Hydrogen-Based Binary Gaseous Mixtures Using Generalized Regression Neural Network. *Int. J. Hydrogen Energy* **2024**, *59*, 242–250. [CrossRef]
123. Monsalve, J.M. A Theoretical Assessment of the On-Site Monitoring of Hydrogen-Enriched Natural Gas by Its Thermodynamic Properties. *Front. Energy Res.* **2025**, *13*, 1339598. [CrossRef]
124. Piazza, L.; Scalabrin, G.; Marchi, P.; Richon, D. Enhancement of the Extended Corresponding States Techniques for Thermodynamic Modeling. I. *Pure Fluids. Int. J. Refrig.* **2006**, *29*, 1182–1194. [CrossRef]
125. Mathias, P.M.; Parekh, V.S.; Miller, E.J. Prediction and Correlation of the Thermal Conductivity of Pure Fluids and Mixtures, Including the Critical Region. *Ind. Eng. Chem. Res.* **2002**, *41*, 989–999. [CrossRef]
126. Cantera. Cantera: MixTransport Class Reference. Available online: https://cantera.org/dev/cxx/d9/d17/classCantera_1_1MixTransport.html (accessed on 19 September 2026).
127. Kee, R.J.; Coltrin, M.E.; Glarborg, P.; Zhu, H. *Chemically Reacting Flow: Theory, Modeling, and Simulation*, 1st ed.; Wiley: Hoboken, NJ, USA, 2017; ISBN 978-1-119-18487-4.
128. Cantera. Transport Properties—Cantera Documentation. Available online: https://cantera.org/dev/reference/transport/index.html (accessed on 19 September 2026).
129. Cantera. Gri30.Yaml—Cantera Documentation. Available online: https://cantera.org/3.2/examples/input/gri30.html (accessed on 19 September 2026).
130. Funk, M.; Wakili, K.G. Driving Potentials of Heat and Mass Transport in Porous Building Materials: A Comparison Between General Linear, Thermodynamic and Micromechanical Derivation Schemes. *Transp. Porous Media* **2008**, *72*, 273–294. [CrossRef]
131. Bonhoure, J.; Pello, R. Temperature of the Triple Point of Methane. *Metrologia* **1978**, *14*, 175. [CrossRef]
132. Chill, F.; Wilfert, S.; Bozyk, L. Cryopumping of Hydrogen on Stainless Steel in the Temperature Range between 7 and 18 K. *J. Vac. Sci. Technol. A* **2019**, *37*, 031601. [CrossRef]
133. Mathot, V.; Staveley, L.A.K.; Young, J.A.; Parsonage, N.G. Thermodynamic Properties of the System Methane + Carbon Monoxide at 90·67° K. *Trans. Faraday Soc.* **1956**, *52*, 1488–1500. [CrossRef]

134. Foster, C.A.; Kim, K.; Turnbull, R.J.; Hendricks, C.D. Apparatus for Producing Uniform Solid Spheres of Hydrogen. *Rev. Sci. Instrum.* **1977**, *48*, 625–631. [CrossRef]
135. Goodwin, R.D. Thermophysical Properties of Methane: Virial Coefficients, Vapor and Melting Pressures. *J. Res. Natl. Bur. Stand. Sect. A Phys. Chem.* **1970**, *74A*, 655–660. [CrossRef] [PubMed]
136. Kleinrahm, R.; Duschek, W.; Wagner, W. (Pressure, Density, Temperature) Measurements in the Critical Region of Methane. *J. Chem. Thermodyn.* **1986**, *18*, 1103–1114. [CrossRef]
137. Züttel, A. Hydrogen Storage Methods. *Naturwissenschaften* **2004**, *91*, 157–172. [CrossRef] [PubMed]
138. Lu, G.; Zou, C.; Wu, S.; Pan, S.; Jiang, X.; Cheng, D.; Liu, H.; Cui, J.; Zhao, Z.; Jing, Z. Occurrence Characteristics of Initial Free and Adsorbed Methane under Pressure-Preserved Coring Conditions and the Influence of Initial Free Methane on Deep Coalbed Methane Production. *Energy Fuels* **2025**, *39*, 5295–5311. [CrossRef]
139. Qiu, Y.N.; Hu, Z.J.; Wu, J.H.; Li, Q.; Zhang, Y.; Zhang, P.; Wang, G.P. Cryogenic Hydrogen Circulation System of Neutron Source. *AIP Conf. Proc.* **2014**, *1573*, 1230–1235. [CrossRef]
140. Poinsot, T.; Veynante, D. *Theoretical and Numerical Combustion*, 2nd ed.; Edwards: Philadelphia, PA, USA, 2005; ISBN 978-1-930217-10-2.
141. Kuo, K.K. *Principles of Combustion*, 2nd ed.; John Wiley: Hoboken, NJ, USA, 2005; ISBN 978-0-471-04689-9.
142. Frisch, H.L.; Stern, S.A. Diffusion of Small Molecules in Polymers. *Crit. Rev. Solid State Mater. Sci.* **1983**, *11*, 123–187. [CrossRef]
143. Koenig, S.P.; Wang, L.; Pellegrino, J.; Bunch, J.S. Selective Molecular Sieving through Porous Graphene. *Nat. Nanotechnol.* **2012**, *7*, 728–732. [CrossRef] [PubMed]
144. Kretzschmar, H.-J.; Wagner, W. *International Steam Tables: Properties of Water and Steam Based on the Industrial Formulation IAPWS-IF97*; Springer: Berlin/Heidelberg, Germany, 2019; ISBN 978-3-662-53217-1.
145. Affandi, M.; Mamat, N.; Kanafiah, S.N.A.M.; Khalid, N.S. Simplified Equations for Saturated Steam Properties for Simulation Purpose. *Procedia Eng.* **2013**, *53*, 722–726. [CrossRef]
146. Struchtrup, H. *Thermodynamics and Energy Conversion*, 1st ed.; Springer: Berlin/Heidelberg, Germany, 2014; ISBN 978-3-662-43715-5.
147. García, F.; García, R.; Padrino, J.C.; Mata, C.; Trallero, J.L.; Joseph, D.D. Power Law and Composite Power Law Friction Factor Correlations for Laminar and Turbulent Gas–Liquid Flow in Horizontal Pipelines. *Int. J. Multiph. Flow* **2003**, *29*, 1605–1624. [CrossRef]
148. Xiao, R.; Joseph, P.; Li, J. The Leak Noise Spectrum in Gas Pipeline Systems: Theoretical and Experimental Investigation. *J. Sound Vib.* **2020**, *488*, 115646. [CrossRef]
149. Marzouk, O.A.; Nayfeh, A.H. A Study of the Forces on an Oscillating Cylinder. In *Proceedings of the ASME 2007 26th International Conference on Offshore Mechanics and Arctic Engineering (OMAE 2007)*; American Society of Mechanical Engineers (ASME): San Diego, CA, USA, 2009; pp. 741–752. [CrossRef]
150. Lin, N.; Lan, H.; Xu, Y.; Dong, S.; Barber, G. Effect of the Gas–Solid Two-Phase Flow Velocity on Elbow Erosion. *J. Nat. Gas Sci. Eng.* **2015**, *26*, 581–586. [CrossRef]
151. Esmaeili, M.; Shahraki, F.; Sardashti Birjandi, M.R.; Khosravi-Bizhaem, H. Black Powder Contamination in Turbine Gas Meters: A Comprehensive Numerical Study of Particle Transport, Deposition, and Erosion Impacts on Measurement Accuracy. *Flow Meas. Instrum.* **2026**, *108*, 103172. [CrossRef]
152. Mahant, B.; C S, S.; Kushwaha, O.S.; Kumar, R. Storage and Transportation of Hythane: Thermodynamics, Kinetics, and Stability Studies Using the Gas Hydrates Process. *Energy Fuels* **2024**, *38*, 17586–17607. [CrossRef]
153. Prasad, V.; Almara, L.M.; Wang, G.-X. Ultra-Long-Distance Transport of Supercritical Natural Gas (SNG) at Very-High Mass Flow Rates via Pipelines through Land, Underground, Water Bodies, and Ocean. *Gas Sci. Eng.* **2023**, *117*, 205053. [CrossRef]
154. Can Turkmen, A.; Espinoza-Andaluz, M.; Celik, C.; Sunden, B.; Serhad Soyhan, H. Impact of the Temperature Variation on the Thermal Conductivity of Gas Diffusion Layers for Polymer Electrolyte Fuel Cells. *Fuel* **2023**, *345*, 128097. [CrossRef]
155. Wang, D. Heat Loss along the Pipeline and Its Control Measures. *SN Appl. Sci.* **2022**, *5*, 2. [CrossRef]
156. Kareem, L.A.; Iwalewa, T.M.; Omeke, J.E. Isobaric Specific Heat Capacity of Natural Gas as a Function of Specific Gravity, Pressure and Temperature. *J. Nat. Gas Sci. Eng.* **2014**, *19*, 74–83. [CrossRef]
157. Caron, M.; Goethals, M.; De Smedt, G.; Berghmans, J.; Vliegen, S.; Van't Oost, E.; Van Den Aarssen, A. Pressure Dependence of the Auto-Ignition Temperature of Methane/Air Mixtures. *J. Hazard. Mater.* **1999**, *65*, 233–244. [CrossRef]
158. Çengel, Y.A.; Kanoğlu, M. Exergy Efficiency of Closed and Unsteady-Flow Systems. *Entropy* **2025**, *27*, 943. [CrossRef] [PubMed]
159. Chatterjee, D. An Enthalpy-Based Thermal Lattice Boltzmann Model for Non-Isothermal Systems. *Europhys. Lett.* **2009**, *86*, 14004. [CrossRef]
160. Mobaraki, M.; Semken, R.S.; Mikkola, A.; Pyrhönen, J. Enhanced Sludge Dewatering Based on the Application of High-Power Ultrasonic Vibration. *Ultrasonics* **2018**, *84*, 438–445. [CrossRef] [PubMed]
161. Valenti, G. 2—Hydrogen Liquefaction and Liquid Hydrogen Storage. In *Compendium of Hydrogen Energy*; Gupta, R.B., Basile, A., Veziroğlu, T.N., Eds.; Woodhead Publishing Series in Energy; Woodhead Publishing: Cambridge, UK, 2016; pp. 27–51, ISBN 978-1-78242-362-1.

162. Osman, A.I.; Mehta, N.; Elgarahy, A.M.; Hefny, M.; Al-Hinai, A.; Al-Muhtaseb, A.H.; Rooney, D.W. Hydrogen Production, Storage, Utilisation and Environmental Impacts: A Review. *Environ. Chem. Lett.* **2022**, *20*, 153–188. [CrossRef]
163. Collet, P.; Flottes, E.; Favre, A.; Raynal, L.; Pierre, H.; Capela, S.; Peregrina, C. Techno-Economic and Life Cycle Assessment of Methane Production via Biogas Upgrading and Power to Gas Technology. *Appl. Energy* **2017**, *192*, 282–295. [CrossRef]
164. Bromberg, L.; Cohn, D.R.; Rabinovich, A.; O'Brie, C.; Hochgreb, S. Plasma Reforming of Methane. *Energy Fuels* **1998**, *12*, 11–18. [CrossRef]
165. Stishov, S.M. Entropy, Disorder, Melting. *Sov. Phys. Uspekhi* **1988**, *31*, 52. [CrossRef]
166. Dincer, I.; Cengel, Y.A. Energy, Entropy and Exergy Concepts and Their Roles in Thermal Engineering. *Entropy* **2001**, *3*, 116–149. [CrossRef]
167. Bejan, A. Fundamentals of Exergy Analysis, Entropy Generation Minimization, and the Generation of Flow Architecture. *Int. J. Energy Res.* **2002**, *26*, 0–43. [CrossRef]
168. Roy, J.R.; Lesse, P.F. On Appropriate Microstate Descriptions in Entropy Modelling. *Transp. Res. Part B Methodol.* **1981**, *15*, 85–96. [CrossRef]
169. Mukherjee, R.N.; Ghorai, P.K.; Biswas, R. Entropy of Mixing: Contributions from Interparticle Interactions and Its Relevance to Deep Eutectic Solvents. *J. Phys. Chem. B* **2025**, *129*, 4410–4419. [CrossRef] [PubMed]
170. Marzouk, O.A. Characteristics of the Flow-Induced Vibration and Forces with 1- and 2-DOF Vibrations and Limiting Solid-to-Fluid Density Ratios. *J. Vib. Acoust.* **2010**, *132*, 041013. [CrossRef]
171. Fan, J.; Müller, M.; Stöhr, T.; Spikes, H.A. Reduction of Friction by Functionalised Viscosity Index Improvers. *Tribol. Lett.* **2007**, *28*, 287–298. [CrossRef]
172. Schlichting, H.; Gersten, K. *Boundary-Layer Theory*; Springer: Berlin/Heidelberg, Germany, 2017; ISBN 978-3-662-52917-1.
173. Lachmann, G.V. *Boundary Layer and Flow Control: Its Principles and Application*; Lachmann, G.V., Ed.; Pergamon Press: Oxford, UK; New York, NY, USA, 1961; Volume 2, ISBN 978-1-4832-2666-8.
174. Marzouk, O.A. A Two-Step Computational Aeroacoustics Method Applied to High-Speed Flows. *Noise Control Eng. J.* **2008**, *56*, 396. [CrossRef]
175. United States National Aeronautics and Space Administration (NASA). Speed of Sound Derivation. Available online: https://www.grc.nasa.gov/www/BGH/snddrv.html (accessed on 19 July 2026).
176. Firgelli. Automations Speed of Sound in Gas Interactive Calculator. Available online: https://www.firgelliauto.com/blogs/calculators/speed-of-sound-in-gas-calculator (accessed on 19 July 2026).
177. Wang, Y.; Wang, P. Analysis of the Application of Ideal Gas Equation of State. *E3S Web Conf.* **2021**, *252*, 03019. [CrossRef]
178. Marzouk, O.A.; Nayfeh, A.H.; Akhtar, I.; Arafat, H.N. Modeling Steady-State and Transient Forces on a Cylinder. *J. Vib. Control* **2007**, *13*, 1065–1091. [CrossRef]
179. Marzouk, O.A. Contrasting the Cartesian and Polar Forms of the Shedding-Induced Force Vector in Response to 12 Subharmonic and Superharmonic Mechanical Excitations. *Fluid Dyn. Res.* **2010**, *42*, 035507. [CrossRef]
180. Marzouk, O.A. Flow Control Using Bifrequency Motion. *Theor. Comput. Fluid Dyn.* **2011**, *25*, 381–405. [CrossRef]
181. Cadorin, M.; Morini, M.; Pinelli, M. Numerical Analyses of High Reynolds Number Flow of High Pressure Fuel Gas through Rough Pipes. *Int. J. Hydrogen Energy* **2010**, *35*, 7568–7579. [CrossRef]
182. Marzouk, O.A.; Nayfeh, A.H. New Wake Models with Capability of Capturing Nonlinear Physics. In *Proceedings of the ASME 2008 27th International Conference on Offshore Mechanics and Arctic Engineering (OMAE 2008)*; American Society of Mechanical Engineers (ASME): Estoril, Portugal, 2009; pp. 901–912. [CrossRef]
183. Ching, E.S.C.; Leung, H.S.; Zwirner, L.; Shishkina, O. Velocity and Thermal Boundary Layer Equations for Turbulent Rayleigh-Bénard Convection. *Phys. Rev. Res.* **2019**, *1*, 033037. [CrossRef]
184. Kamble, B.V.; Kuzhiveli, B.T.; Jain, R.; Prasad, S.; Kasthurirengan, S.; Behera, U. Experimental Studies of the Influence of Prandtl Number on the Performance of a Thermoacoustic Prime Mover. *AIP Conf. Proc.* **2014**, *1573*, 768–775. [CrossRef]
185. Saha, S.K.; Tiwari, M.; Sundén, B.; Wu, Z. *Advances in Heat Transfer Enhancement*, 1st ed.; Springer International Publishing: Cham, Switzerland, 2016; ISBN 978-3-319-29480-3.
186. Maytal, B.-Z.; Pfotenhauer, J.M. The Joule-Thomson Effect, Its Inversion and Other Expansions. In *Miniature Joule-Thomson Cryocooling*; Springer: New York, NY, USA, 2013; pp. 39–72, ISBN 978-1-4419-8284-1.
187. Harmon, C.W. Measurement of the Joule–Thomson Coefficient of Nitrogen and Carbon Dioxide to Demonstrate LabVIEW, Electronic Data Acquisition, and Experimental Design. *J. Chem. Educ.* **2024**, *101*, 949–955. [CrossRef]
188. Venkatarathnam, G. Fundamental Principles and Processes. In *Cryogenic Mixed Refrigerant Processes*; Timmerhaus, K.D., Rizzuto, C., Eds.; International Cryogenics Monograph Series; Springer: New York, NY, USA, 2008; pp. 1–50, ISBN 978-0-387-78513-4.
189. Balmer, R.T. First Law Open System Applications. In *Modern Engineering Thermodynamics*; Elsevier: Amsterdam, The Netherlands, 2011; pp. 167–203, ISBN 978-0-12-374996-3.
190. Stull, R. 3.1: Internal Energy. Available online: https://geo.libretexts.org/Bookshelves/Meteorology_and_Climate_Science/Practical_Meteorology_(Stull)/03%3A_Thermodynamics/3.01%3A_Internal_Energy (accessed on 12 June 2026).

191. Dincer, I. 1.7 Energy and Exergy Efficiencies. In *Comprehensive Energy Systems*; Dincer, I., Ed.; Elsevier: Oxford, UK, 2018; pp. 265–339, ISBN 978-0-12-814925-6.
192. Pimentel, L.; Guerrieri, Y.; Costa, G.; Pontes, K.V. Joule–Thomson Effect in Mixtures Containing Polymers and Copolymers. *Ind. Eng. Chem. Res.* **2016**, *55*, 1117–1125. [CrossRef]
193. Yang, F.; Wang, T.; Deng, X.; Dang, J.; Huang, Z.; Hu, S.; Li, Y.; Ouyang, M. Review on Hydrogen Safety Issues: Incident Statistics, Hydrogen Diffusion, and Detonation Process. *Int. J. Hydrogen Energy* **2021**, *46*, 31467–31488. [CrossRef]
194. Marzouk, O.A. Reheat Pressure Influence on the Performance of Steam Rankine Power Cycles, and an Introduced Level of Reheat (LOR) Normalized Variable. *Open Eng.* **2026**, *16*, 20250208. [CrossRef]
195. Li, Z.; Zhang, C.; Li, C.; Jia, W. Thermodynamic Study on the Natural Gas Condensation in the Throttle Valve for the Efficiency of the Natural Gas Transport System. *Appl. Energy* **2022**, *322*, 119506. [CrossRef]
196. Xu, X.; Cai, L.; Chen, T.; Zhan, Z. Analysis and Optimization of a Natural Gas Multi-Stage Expansion Plant Integrated with a Gas Engine-Driven Heat Pump. *Energy* **2021**, *236*, 121321. [CrossRef]
197. Aman, Z.M. Hydrate Risk Management in Gas Transmission Lines. *Energy Fuels* **2021**, *35*, 14265–14282. [CrossRef]
198. Chen, Q.-S.; Wegrzyn, J.; Prasad, V. Analysis of Temperature and Pressure Changes in Liquefied Natural Gas (LNG) Cryogenic Tanks. *Cryogenics* **2004**, *44*, 701–709. [CrossRef]
199. ANGI. Energy Storage Solutions for CNG Stations. Available online: https://www.angienergy.com/storage-solutions-cng-stations (accessed on 12 June 2026).
200. Marzouk, O.A. Compilation of Smart Cities Attributes and Quantitative Identification of Mismatch in Rankings. *J. Eng.* **2022**, *2022*, 5981551. [CrossRef]
201. Marzouk, O.A. Solar Heat for Industrial Processes (SHIP): An Overview of Its Categories and a Review of Its Recent Progress. *Solar* **2025**, *5*, 46. [CrossRef]
202. Marzouk, O.A. Land-Use Competitiveness of Photovoltaic and Concentrated Solar Power Technologies near the Tropic of Cancer. *Sol. Energy* **2022**, *243*, 103–119. [CrossRef]

Disclaimer/Publisher's Note: The statements, opinions and data contained in all publications are solely those of the individual author(s) and contributor(s) and not of MDPI and/or the editor(s). MDPI and/or the editor(s) disclaim responsibility for any injury to people or property resulting from any ideas, methods, instructions or products referred to in the content.